Development of Nano-TiO_2/Y_2O_3 Dispersed Zirconium Alloys by Mechanical Alloying Followed by Conventional and Spark Plasma Sintering

Dissertation submitted to the
National Institute of Technology Rourkela
in partial fulfillment of the requirements
of the degree of
Doctor of Philosophy
in
Metallurgical and Materials Engineering
by
Mohan Nuthalapati
(Roll Number: 511MM110)
under the supervision of
Prof. Anindya Basu
and
Prof. Swapan Kumar Karak

January, 2016
Department of Metallurgical and Materials Engineering
National Institute of Technology Rourkela

Metallurgical and Materials Engineering

National Institute of Technology Rourkela

January, 2016

Supervisor's Certificate

This is to certify that the work presented in this dissertation entitled "*Development of Nano-TiO_2/Y_2O_3 Dispersed Zirconium Alloys by Mechanical Alloying Followed by Conventional and Spark Plasma Sintering*" by "*Mohan Nuthalapati*", Roll Number 511MM110, is a record of original research carried out by him under our supervision and guidance in partial fulfillment of the requirements of the degree of *Doctor of Philosophy* in *Metallurgical and Materials Engineering.* Neither this dissertation nor any part of it has been submitted for any degree or diploma to any institute or university in India or abroad.

--------------------------	--------------------------
Swapan Kumar Karak Co-Supervisor	Anindya Basu Principal Supervisor

Declaration of Originality

I, Mohan Nuthalapati, Roll Number 511MM110 hereby declare that this dissertation entitled *“Development of Nano-*TiO_2/Y_2O_3 *Dispersed Zirconium Alloys by Mechanical Alloying Followed by Conventional and Spark Plasma Sintering”* represents my original work carried out as a doctoral student of NIT Rourkela and, to the best of my knowledge, it contains no material previously published or written by another person, nor any material presented for the award of any other degree or diploma of NIT Rourkela or any other institution. Any contribution made to this research by others, with whom I have worked at NIT Rourkela, is explicitly acknowledged in the dissertation. Works of other authors cited in this dissertation have been duly acknowledged under the section "Bibliography". I have also submitted my original research records to the scrutiny committee for evaluation of my dissertation.

I am fully aware that in case of any non-compliance detected in future, the Senate of NIT Rourkela may withdraw the degree awarded to me on the basis of the present dissertation.

January, 2016
NIT Rourkela

Mohan Nuthalapati

Acknowledgment

This work would not have the spirit without the valuable academic, educational, psychological and human support. So, I would like to acknowledge the support of the people who made it possible.

I would like to express the deepest appreciation to my supervisor Prof. Anindya Basu, who has the attitude and the efficiency: he continually and convincingly communicates in regard to research and teaching. Without his guidance and persistent help this dissertation would not have been possible.

I express my sincere gratitude to my supervisor Prof. Swapan Kumar Karak, who introduced me to Zirconium alloys and whose enthusiasm for the "High Temperature Structural Materials" had lasting effect.

It is a pleasure to express my deep sense of thanks to Dr. D. Chakravarty, Scientist of ARCI, Hyderabad, for providing me with the facility to carry out Spark Plasma Sintering in his laboratory.

I would like to express my sincere gratitude to Prof J. Dutta Mazumdar, Department of Metallurgical and Materials Engineering, IIT, Khargpur, for permitting me to carry out the experiments in her laboratory.

I am very much thankful to Prof. Debasis Chaira, Department of Metallurgical and Materials Engineering, for allowing me to carry out milling.

I would like to thank especially S. Pradhan, U. K. Sahu, Arindam Pal, R. Pattanaik, S. Hembram technical staff of Metallurgical and Materials Engineering department, for practical assistance.

I am extremely grateful to my friends, D. Narsimhachary and Ranjan Kumar Behera, for their help throughout my project. I would also like to thank Anand Babu. K, for his help during oxidation tests.

January, 2016
NIT Rourkela

Mohan. Nuthalapati
Roll Number: 511MM110

Abstract

Zirconium based alloys are attractive materials for high temperature applications mainly in the chemical and nuclear sectors due to their excellent corrosion resistance, good mechanical and thermal properties with very low neutron absorption. Minor addition of nano oxides in zirconium matrix enhances mechanical properties by dispersion strengthening and its grain boundary pinning results in better high temperature stability. Moreover nano-sized oxide dispersion in the alloy suppresses the grain growth during annealing at high temperature results in the improvement of creep strength. The elevated temperature yield strength and corrosion resistance of zirconium alloys can be increased by dispersion of nano-TiO_2/Y_2O_3.

The present study deals with nano-TiO_2/Y_2O_3 (1.0-2.0 wt. %) dispersed Zr based alloys with nominal compositions: $Zr_{45}Fe_{30}Ni_{20}Mo_5$ (alloy-A), $Zr_{44}Fe_{30}Ni_{20}Mo_5$ $(TiO_2)_1$ (alloy-B_1), $Zr_{44}Fe_{30}Ni_{20}Mo_4(TiO_2)_2$ (alloy-B_2), $Zr_{44}Fe_{30}Ni_{20}Mo_5$ $(Y_2O_3)_1$ (alloy-C_1) and $Zr_{44}Fe_{30}Ni_{20}Mo_4(Y_2O_3)_2$ (alloy-C_2) are synthesized by mechanical alloying (MA) in two ball mills (Mill-1: planetary and Mill-2: dual drive) followed by powder consolidation with conventional and spark plasma sintering (SPS) at 1400 ^{o}C and 900-1000 ^{o}C respectively. The microstructural and phase analysis of mechanical alloyed powders and consolidated products were studied by XRD, SEM/EDS and TEM followed by evaluation of physical (density), mechanical (compressive strength, hardness and wear resistance) and chemical (oxidation and corrosion resistance) properties.

X-ray diffraction and TEM analysis reveal formation of different intermetallics of 10-30 nm size along with TiO_2/Y_2O_3 (10-20 nm) throughout the matrix. Alloys consolidated by spark plasma sintering was found to possess high levels of compressive strength (825-1240 MPa) and hardness (10.38-16.85 GPa) which was 1.5-2 times higher than that obtained from conventional sintering. Addition of TiO_2 and Y_2O_3 helps in enhancement of mechanical properties and effect of TiO_2 was more prominent.Y_2O_3 dispersion displays better corrosion resistance, whereas, base alloy shows best oxidation property.

After scrutinizing all characterizations and results it was concluded that dual drive ball mill was more efficient than planetary mill and SPS technique was found more efficient and advanced to produce product with better mechanical, oxidation and corrosion properties. Moreover, dispersoids helped in improving the key properties needed for structural and corrosion applications.

Key words: Mechanical alloying; Zirconium alloy; SPS; TEM; Mechanical property; electro chemical property.

Contents

List of Figures

List of Tables

Chapter 1

Introduction

1.1 Introduction

Zirconium alloys are the primary structural materials for nuclear and chemical sectors. Since 1960 Zirconium alloys are the principal cladding materials with excellent corrosion resistance, very low thermal neutron cross section and good mechanical properties [1--4]. Zirconium alloys have superior thermal properties compared to other traditional materials. The thermal conductivity of Zirconium alloys is 30% higher than stainless steel group of alloys and the linear coefficient of thermal expansion is one third the value of stainless steel which provide zirconium alloys superior dimensional stability at elevated temperature [5--7].

Due to the cost, early commercial nuclear power reactors used stainless steel to clad uranium dioxide fuel. In the preparation of nitric acid generally stainless steel of AISI 316 and 304 grades have performed well within certain process conditions [8]. If the concentration of the chemical or applied temperature became too high the problem of corrosion attack increases. In these conditions the unique properties of zirconium alloys made the ultimate material to use in both nuclear and chemical sectors [9--11].

During last few decades, there has been significant technological interest in the synthesis of nano-structured materials by mechanical alloying (MA) [12--14]. In order to acquire nano-crystalline structure or amorphous phase, the alloys were treated by different non-equilibrium processing techniques such as solid-state quenching, rapid solidification, mechanical cold work, irradiation/ion implantation and condensation from vapor. Powders of similar structure can also be formed by high energy deformation processing via mechanical alloying [15--17]. Over the past several years, there has been extensive development in producing high temperature materials for ever more demanding applications. The primary requirements of these alloys are high strength, high hardness, wear resistance, high creep resistance and high oxidation resistance at elevated temperature.

Iron, Ni-based metallic materials are the usual class of super alloys with high temperature strength, corrosion and oxidation resistance. Molybdenum is a commercial refractory material with high recrystallization temperature. Moreover, dispersion hardening improves creep resistance for structural materials. With these alloying elements and dispersoid (nano-oxide), there is a possibility of improving high temperature properties. Moreover, some of the Zr-based alloys have high glass forming ability for high temperature application [18, 19].

The process of sintering is the most important task for materials with high melting points. During sintering grain growth and densifications are two simultaneous processes and it has a great influence on microstructure [20, 21]. Spark plasma sintering (SPS) is an advanced sintering process that makes use of a microscopic electric discharge between the particles under pressure by plasma formation followed by Joule heating. This has been acknowledged to reduce the densification temperature to a great extent with minimum grain growth leading to high density products [22].

Alloying of Zr with elements such as Fe, Ni, Mo, and dispersoid addition may be a possibility to increase the high temperature strength of Zr-based alloys. Because the solid solubility of such alloying elements in Zr is limited, conventional melting casting process would not be appropriate to develop such high temperature alloys. Moreover, this route lags in control over grain refinement and homogeneous dispersion of oxides due to the density difference between oxide and the matrix [23--25]. Development of such high temperature alloys can only be possible by mechanical alloying to avoid the disintegrated melting casting processing route. Mechanical alloying improves grain refinement, homogeneous dispersion of oxide and the formation of non-equilibrium phases, leading to better mechanical properties [26--29].

The overall scope and objectives of this investigation are: (a) to synthesize the ODS alloys by dispersion of 1-2 wt. % TiO_2/Y_2O_3 in Zr-Fe-Ni-Mo alloy by mechanical alloying and subsequent consolidation by conventional and spark plasma sintering techniques (b) study the effect of process parameters on microstructure, hardness, compressive strength, wear resistance, corrosion and oxidation resistance properties, and finally, (c) arrive at a detailed structure-property correlation to optimize the process parameters for fabrication of nano-TiO_2/Y_2O_3 dispersed zirconium alloys.

Major objectives of the present study are:

- Synthesis of alloy powders $Zr_{45}Fe_{30}Ni_{20}Mo_5$ (alloy-A), $Zr_{44}Fe_{30}Ni_{20}Mo_5 (TiO_2)_1$ (alloy-B_1), $Zr_{44}Fe_{30}Ni_{20}Mo_4 (TiO_2)_2$ (alloy-B_2), $Zr_{44}Fe_{30}Ni_{20}Mo_5 (Y_2O_3)_1$ (alloy-C_1) and $Zr_{44}Fe_{30}Ni_{20}Mo_4 (Y_2O_3)_2$ (alloy-C_2) by mechanical alloying involving two different mills: Mill-1 (high energy planetary ball mill), Mill-2 (high energy dual drive planetary ball mill).

- Phase and microstructural characterization of powders obtained from Mill-1 and Mill-2 involving XRD, SEM/EDS, Particle size analyzer and TEM.

- Study of recrystallization behaviour of final milled powders obtained from both the mills by TG/DSC.

- Phase and microstructural characterization of conventional and spark plasma sintered (SPS) products by XRD, SEM and TEM.

- Evaluation of physical (Density) and mechanical properties (Hardness, Compressive strength and Wear resistance) of sintered products.

- Corrosion, Iso-thermal and Non-isothermal oxidation study of the consolidated products.

- Correlation of process parameters and addition of dispersoids (TiO_2/ Y_2O_3) with mechanical (Hardness, Compressive strength and Wear resistance) and chemical (Corrosion, Iso-thermal and Non-isothermal oxidation) properties of all the alloys sintered by conventional and SPS process.

1.2 Structure of Thesis

This thesis contains seven chapters**.** Chapter-1 introduces the concept and back ground of the present work. The discussion includes an overview of the objectives of the present study.

Literature survey on high temperature materials, application in nuclear and chemical sector, and how zirconium alloys can fulfill these requirement and development of ODS zirconium alloys by mechanical alloying has been incorporated in chapter-2.

Chapter-3 describes experimental procedures of powder production of all the alloys with 1-2 wt. % nano-TiO_2/Y_2O_3 dispersion, sintering process (conventional and spark plasma sintering) and characterization of microstructure, phase aggregate, physical/mechanical properties of interest.

Chapter-4 is focused on synthesis of alloy powder and results obtained from powder characterization. Consolidation of alloy powders by different techniques and characterization of sintered products, and results are described in Chapter-5 and Chapter-6. The conclusions drawn from the present study are summarized in Chapter-7. Bibliography details are provided after these chapters.

Chapter 2

Literature Review

2.1 High Temperature Materials and its Applications

High temperature materials provide the fundamental support for extensive area of technology covering energy, electronic, photonic and chemical applications [30, 31]. High temperature metallic material starts from plain carbon steel to metals of the platinum group. These alloys have high strength, high hardness, wear resistance, creep resistance and high oxidation resistance at elevated temperatures. They can be iron base alloys, nickel base alloys, cobalt base alloys or refractory metals and alloys [32, 33]. Some of the high temperature materials and their industrial applications are given in Table 2.1. The metallic materials used for high-temperature purposes can be categorized into a few distinctive groups based on composition and structure.

Table 2.1: Different high temperature materials and their uses

High temperature materials		Uses
Irons and Steels	Cast irons	Combustion and heat-treatment equipment.
	Ferritic steels	Cold-water tanks and refrigeration cabinets.
	Austenitic steels	Wrought products and aviation construction parts.
Nickel-chromium Alloys		As electric heating element and furnace parts.
Superalloys	Iron-based superalloys	Tool making to specialized medical and chemical synthesis applications.
	Nickel-based superalloys	Jet engine components, corrosion resistant chemical process equipment and heating elements.
	Cobalt-based superalloys	Prosthetic devices, magnets and cutting tool binders.
	Tungsten alloys	Filaments for electric bulbs, electric contacts, heating elements, radiation shields and rocket nozzles.

Refractory Metals	Molybdenum alloys	Heating elements for high temperature furnaces, hooks and grids in thermionic valves in electric industry, hot working tools and dies.
	Zirconium alloys	Construction material (corrosion resistance), vacuum tubes (electrical engineering), pyrotechnical use, Cladding material, catalyst (as Zr organic compound).
Other Metals	The metals of the platinum group and alloys	For thermocouple wires, glass melting and working equipment, crystal-growing crucibles and aircraft spark plugs etc.

The main fields in which high temperature materials are used are categorized below.

- <u>Energy Generation and Conversion Sectors:</u>

  - *Steam Turbines*: In the world, majority of the power generation was provided by oil or coal fired steam, using maximum temperature of about 700 ^{o}C. In these steam generating plants some components reach high temperature and may be in severe corrosion and erosion attack. Some critical components are super heater tubes and tube supports. Piping and valves carrying steam from boilers to turbines are highly stressed and may also suffer steam erosion. In the turbines the casings and casing bolts are highly stressed due to the steam pressure, while the rotors, blades and nozzles have forced stresses due to centrifugal forces, gas pressure and thermal changes. The exploration and production of oil and gas is totally dependent on specialized steels. The alloying elements of steels for strength and durability are nickel, molybdenum, manganese, cobalt, vanadium and tungsten [34].

  - *Nuclear Reactors:* High temperature material problems arise in all types of nuclear reactors with fuel cans. This is due to stress produced by fuel expansion and corrosion by the coolant. Almost all the nuclear reactors operating with water cooled or gas cooled systems, generate steam at temperature range of 250-500 ^{o}C [35]. But in the new type of reactors coolant temperature exceeds 600 ^{o}C and above this temperature problems arise, especially in heat exchangers, steam generators, transfer piping and valves by corrosive or erosive attack by the coolant. The high temperature materials suggested for nuclear applications are nickel-super alloys, silicon carbide, high corrosion resistance steels and refractory alloys. Depending on the particular reactor design, there may be zirconium plus tin, niobium, iron, chromium nickel (Zircaloy) for fuel cladding.

- *Coal Conversion Sectors*: Processes involving coal like conventional burning, fluidised bed combustion, gasification and liquefaction may involve temperatures varying from about 400-1600 ^{o}C at high pressure. But the metal temperatures of plant components are normally restricted to less than 700-800 ^{o}C. The combustion gases containing carbon, sulphur, hydrogen, oxygen and their compounds provide a severe corrosive and erosive environment. The components exposed to severe conditions include the internal parts of combustion beds or reaction zones, transfer pipes, valves, probes and heat exchangers. For majority of coal fuels electricity generations, specialist steels are essential for turbine manufacture [34].

➢ Transport:

- *Aircraft and Space Vehicles*: Super alloys are used for air craft gas turbine applications. As these materials can resist the creep and fracture at temperature range of 700-1100 ^{o}C. These alloys are mainly required for resisting the high centrifugal or thermal stresses on the blades. For space travel the rocket motor may get into severe problems at high temperature. The high velocity and temperature the exhaust gas generates high thermal stress and erosion action. In the aerospace sector, there is a need for light alloy materials that can retain strength at high temperatures in turbines components [36].

- *Marine*: Ingested salt from marine environment can causes corrosion problems in gas turbines used in naval vessels. Merchant ships are mainly based on the diesel engine in which a number of critical components are subjected to severe mechanical or thermal stresses and corrosive attack at high temperatures. The highest temperature (about 800 ^{o}C) is reached in pre-combustion chambers and in exhaust valves, associated with high mechanical stress. Exhaust components are similar in principle to gas turbines and encounters problems of creep and thermal fatigue. Nickel base super alloys are generally used in turbines for marine vessels.

- *Road and Rail*: Road and rail transport uses diesel engines, which operate at high speeds causing its component stressed at high temperature. In spark ignition engines in automobile, the exhaust valves temperature may reach 700

^{o}C and spark electrodes may reach 800 ^{o}C. A massive amount of low grade steel is used to support underground roadways whereas more specialized steel are used in rails [37].

- Chemical Sector:

  - For the conversion of feed stock, in oil, chemical and other industries, a wide range of chemicals are required [38]. These processes involve treatment at elevated temperature or even at high temperatures and pressures. Suitable materials for high temperatures under inert conditions in chemical industries are materials with high corrosion resistant and chemical compatibility [39]. Stainless steel, molybdenum, titanium and zirconium alloys are used as structural materials in chemical plants.

- Thermal Processing:

  - Thermal processing is an essential step in many industries in the production procedure and for construction of such plant, it involves materials which are resistant to the required temperature and environment conditions. The metal industry, cement and refractory industries require furnaces for the treatment of materials, while the ceramic and glass producers similarly operate melting and firing furnaces. These industries operate at temperature even above 1400 ^{o}C and oxidation occurs at this elevated temperature. Refractory materials and their alloys are suitable for such thermal processing industry.

Nuclear and chemical industries require special attention due to irradiation condition and high temperature oxidation.

2.1.1 Nuclear Industry

In 1954, USSR constructed the first nuclear power plant and the first commercial nuclear power plant was constructed in USA in 1957. Presently around 450 nuclear reactors produce electricity throughout the world. More than 15 countries rely on nuclear power for 25% of their electricity. The nuclear share of electricity is over 30% in Europe and Japan. In the USA 20% of electricity created by nuclear power reactors [40]. China, India, USA, Russia and Japan have strong commitment to nuclear power. Other countries are acting to increase the role of nuclear power in their economies.

After thermal, hydroelectric and renewable sources, nuclear power is the fourth-largest source of electricity in India. India has 7 nuclear power plants having a capacity of 5780 MW electricity and producing a total of 30,292.91 GWh [41]. India is now trying to increase the contribution of electricity generation by nuclear power from 2.8% to 9% within next 25 years. It is estimated that by 2025, India's installed nuclear power generation capacity would be 20 GW. Figure 2.1. Shows the world nuclear share in electricity. Global nuclear industry growing faster to build nuclear power as a long-term alternative.

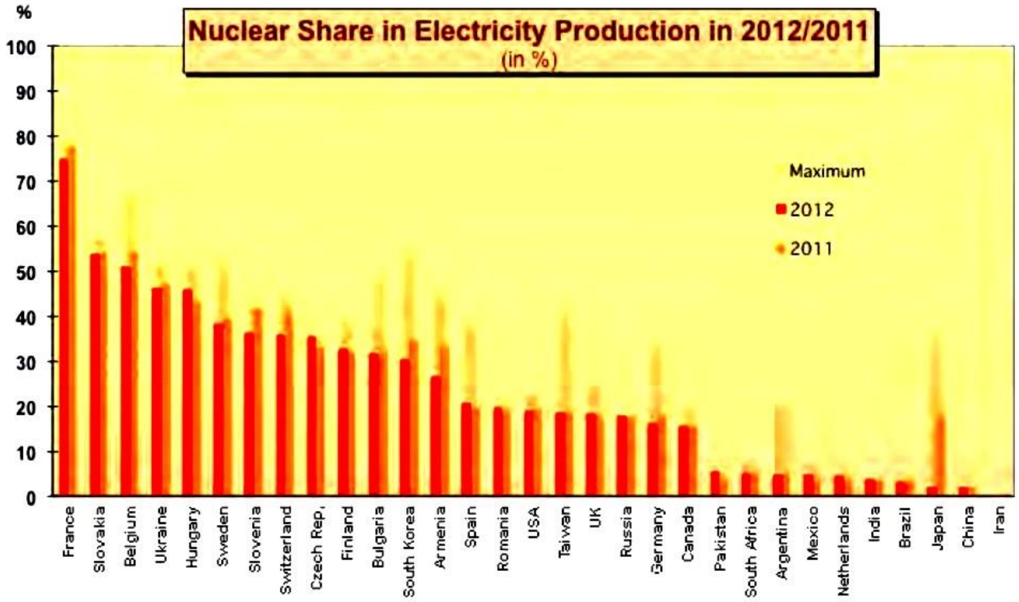

Figure 2.1: Nuclear share in electricity 2012/2011 [40]

Nowadays in nuclear power plant danger caused by the equipment failure is the most important concern. Basically the failure occurs at high temperature due to high reactivity of fuel and cladding materials. The best example of hydrogen explosion due to the reaction between cladding material and water was happened at Three Mile Island nuclear power plant in 1979. Materials for nuclear reactors must simultaneously withstand the effects of high temperature, intense gamma radiation and bombardment by neutrons [42]. At the same time they must be capable of containing the highly radioactive fission product produced in the nuclear reaction. With above mentioned properties, the materials with low rate of corrosion with fuel were the best option for nuclear cladding materials or in-core structural materials.

2.1.2 Chemical Industry

Chemicals became basic need in every day’s human life and they are helpful to survive in critical situation. The Chemical Industry is the main stream to the modern world economy [43]. The Asia-Pacific market was wide open for chemical industries to manufacture and sale. Figure 2.2 and 2.3 shows the percentage shift of chemical industry of Asia from1985 to future 2030, and world chemicals sales by region from 1999 to 2009 respectively. Chemicals manufacturing and sale is a huge economic option for the Asian-Pacific market. The rise of Asian-Pacific market provides India a chance to supply more chemicals.

In India the chemical sector contribution was 14% in overall industrial productions [38]. India has 3rd place in producing chemical in Asia after China and Japan. The chemical sector accounts 7% of GDP and 11% of National export in India [44].

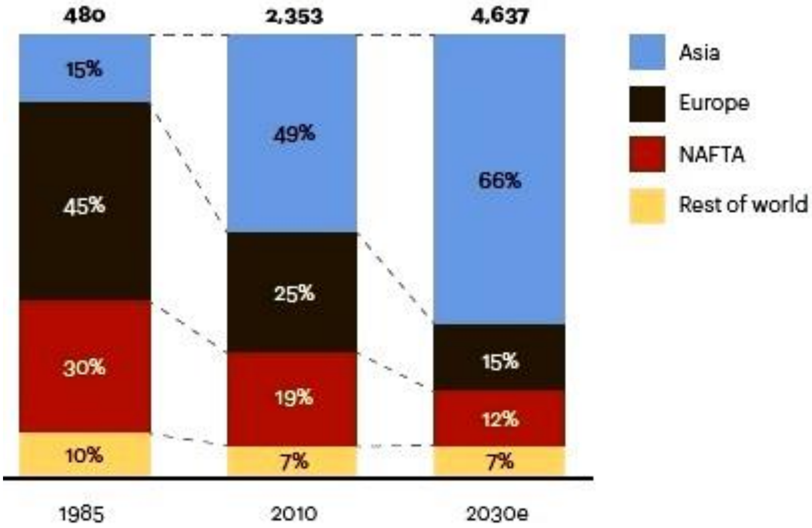

Figure 2.2: Percentage shift of chemical sector to Asia [43]

In chemical industry, sulfuric acid has multiple applications. Phosphate and nitrogen based fertilizers can be manufactured by using large quantities of sulfuric acid. Not only sulfuric acid, there are some other chemicals which can be useful in industrial processing including nitric acid, hydrochloric acid, ammonia etc. In the plants using these acid in one or more process steps generally results in severe corrosion problems. The reactivity was high at higher temperature and high concentrations [45].

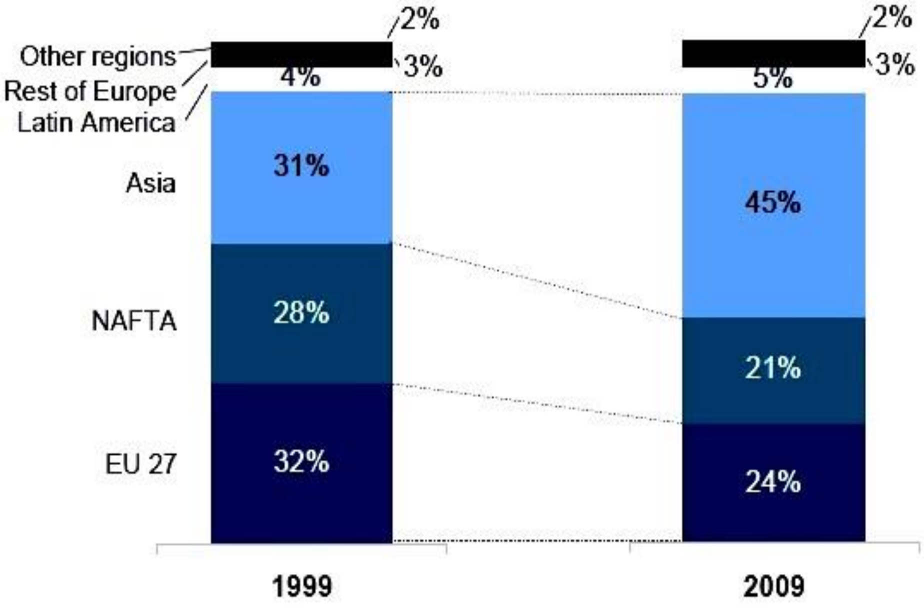

Figure 2.3: World chemical sales by region [38]

Due to the corrosion attack by these chemicals, thermal cracking occurs in the structural material at high temperature and even at high concentration. The materials with high corrosion resistance chemical compatibility are fit for these requirements.

2.1.3 Requirements

Materials for nuclear and chemical industry must withstand the effects of high temperature. These materials should sustain in harsh environment for a prolong period of time even at high temperatures and pressures [46].

The major structural material requirements for nuclear reactors are:

a) *Good mechanical properties* (Strength, Hardness, Wear resistance and Creep resistance).

b) *Low absorption of neutrons*.

c) *Radiation stability* (under intense gamma and neutron irradiation).

d) *Corrosion resistance* (with fuel, moderator and coolant): Bulk and surface stability against oxidation and corrosion during prolonged exposure to the fuel cell environment.

e) *Good thermal stability* (Thermal expansion compatibility with the other stack components).

If neutron absorption of stainless steel would have less, it could be the ideal structural material for nuclear reactors. To continue the chain reaction the fuel would have to be enriched with fissile material. But, the range of materials is limited to carbon (graphite), beryllium, magnesium, zirconium and aluminum.

Due to inherent porosity graphite is not suitable for containing moderator or coolant. In addition to this, it has poor mechanical properties under complex loading. Beryllium is brittle at room temperature, difficult to fabricate and expensive. Aluminum and magnesium have relatively low melting points (650-660 ^{o}C) and have insufficient strength for components such as pressure tubes, especially if elevated temperatures are involved. Zirconium is the most suitable material for in-core components. But, pure zirconium has insufficient strength or creep resistance so it must be alloyed to improve mechanical properties. Limited alloy additions are acceptable so that does not increase neutron absorption leading to necessary fuel enrichment [8].

Some notable requirements for the structural materials in chemical industries are:

a) *Chemical compatibility*: Chemical compatibility with other materials in contact with inter-connects such as seals and cell materials.
b) *Corrosion resistance*.
c) *Mechanical reliability and durability* at the device’s operating temperature.

Ferritic and austenitic steels have been used for different high temperature applications in oil and chemical plants and in power generation equipment. However, there are particular characteristics of these two classes of material which severely restrict their range of application in terms of permissible operating parameters and these can lead to failures in service. The excellent corrosion resistance in many organic/inorganic acids, good strength and ductility at moderately high temperatures made zirconium the suitable material for chemical industry [8].

2.2 Zirconium Alloys

Zirconium is a commercially available refractory metal with excellent corrosion resistance, good mechanical properties and very low thermal neutron cross section. The unique properties of zirconium made it ideal cladding material for the U.S. Navy nuclear propulsion program in the 1950's. The earlier commercial nuclear power reactors used stainless steel to clad the uranium dioxide fuel due to cost. But by mid-1960 zirconium alloys were the principal cladding material due to the superior neutron economy and corrosion resistance. These same zirconium alloys are convenient to designers of high level nuclear waste disposal containers as internal components or external cladding materials [48]. The advantages of zirconium alloys for long term nuclear waste disposal include exceptional radiation stability and 100% compatibility with existing Zircaloy fuel cladding to ease any concerns of galvanic corrosion.

Zirconium was discovered by Klaproth in 1789. In 1925 Van Arkel and De Boer refined and produced high purity zirconium. The first zirconium material was used in the electronic industry for residual gas gettering. US Bureau of Mines developed the Zirconium sponge in 1947. In 1949 zirconium was selected as the structural material for nuclear reactors of submarines due to its good mechanical properties and low neutron absorption cross section. Thermal neutron cross sections of some elements given in Table 2.2. In the late 1950’s zirconium became the chemical process equipment in severe corrosion environments. In 1960’s zirconium became main cladding material for water cooled reactors. By the middle of 1970, world production of zirconium was about 4000 tons and been used 55% in commercial nuclear reactors, 30% in US naval nuclear reactors, and 15% as chemical process equipment. Magnesium and aluminums were replaced by zirconium also for photoflash applications and can be used as getter for oxygen and other gases. Moreover, Zirconium intermetallics are suitable as hydrogen storage materials [8, 47].

Table 2.2: Thermal neutron cross section (10^{-28} m^2) [8]

Element	Al	Steel	Fe	Pb	Mg	Ni	Ti	Zr	Zircaloy-4
Thermal neutron cross section	0.23	3.1	2.56	0.17	0.05	4.5	6.1	0.18	0.22

2.2.1 Properties of Zirconium Alloys

Zirconium alloys are much attractive materials in the fields of chemical and nuclear sectors for high temperature activities due to its low thermal neutron cross section, good mechanical and corrosion properties. Some of Zirconium and its alloy properties are mentioned in Table 2.3. Zirconium alloys mechanical properties are given in Table 2.4. From Table 2.4 it can be noticed that the elastic limit and tensile strengths are substantially increasing with the higher alloy content of the material, while the elasticity remains almost constant. The main reason for the modest elasticity value is the material's hexagonal atomic structure, due to having the limited number of glide planes.

Table 2.3: Physical and Mechanical properties of Zirconium, Zircaloy-2 and Zircaloy-4

Property	Zr	Zircaloy-2	Zircaloy-4
Density, g/cc	6.5	6.55	6.55
Melting T, ^{o}C	1845	1830	1850 ^{o}C
Transition T, ^{o}C	862	1000	-
Recrystallization T, ^{o}C	450-550	550-600	-
Thermal neutron Cross section (barns)	0.18	>0.18	-
Ultimate Strength-psi	34800	68600	-
Yield Strength-psi	9900	44800	-
Elongation-%	47	22	
Crystal structure (α phase)	Hexagonal <865 ^{o}C	-	810 ^{o}C
Crystal structure (β phase)	β - 865 to 1845 ^{o}C - bcc	-	980 ^{o}C
Coefficient of expansion (α), /^{o}C	10^{-4} x 6.38	-	6
Thermal conductivity (k) cal/cm-s-^{o}C	0.050	0.035	0.0513
Heat capacity (C) J/g-^{o}C	-	-	0.285
Hardness (Rb)	-	-	89
Modulus of elasticity (GPa)	-	-	99.3
Poisson's ratio	-	-	0.37
Shear modulus (GPa)	-	-	36.2

Table 2.4: Mechanical values of zirconium and zirconium alloys

Grade	Zr702	Zr704	Zr705	Zr706
Tensile strength in MPa	379	411	552	510
Elastic limit 0.2% in MPa	207	241	379	345
Elasticity in%	16	14	16	20

Zirconium is categorized as a reactive metal because it forms a solid and neatly packed layer of zirconium oxide on the surface without electrolyte. The oxide layer is noble and very stable, providing the underlying metal with optimum protection against all kinds of chemical reagents. Zicaloy-4 corrosion rate in different chemical media is given in Table 2.5. Zirconium resists corrosive attack in most organic and mineral acids, strong alkalis, and some molten salts. Solutions of nitric acid (HNO_3), sulfuric acid (H_2SO_4), and hydrochloric acid (HCl) with impurities of ferric, cupric and nitrate ions generally result in corrosion rates of less than 0.13 mm/a (5 mpy) even at temperatures well above the boiling point curve [8]. A tightly adherent and protective oxide film protects the metal-oxide interface to provide corrosion resistance. An additional benefit for zirconium alloys in long-term geological disposal options is the inert nature of zirconium oxide. Application of zirconium alloys alleviates the concern of nickel and chromium contamination in the ground water in severely corroded spent fuel containers.

Table 2.5: Corrosion rate of Zicaloy-4 in different chemical reagent

Corrosion media	Concentration (%)	Temperature (^oC)	Corrosion rate (mm/a)
HCl	70	160	0.36
HNO_3	70	120	0.05
H_2SO_4	70	150	<0.13
$CuCl_2$	0.1	144	0.03
$FeCl_3$	1	135	0.18
NaCl	25	250	nil

2.2.2 Applications of Zirconium Alloys

The key characteristics of Zr metallurgy come from its strongly anisotropic hexagonal crystal structure which during thermo-mechanical processing leads to the development of a textured material. It has high reactivity with oxygen and due to different types of chemical interactions with the alloying elements, shows both complete solubility and intermetallic compound formation.

Different types of zirconium alloy grades used in water-cooled nuclear reactors and are also available for nuclear waste disposal components. The materials with low hafnium content are suitable for nuclear action. The hafnium content shouldn't reach more than 0.010%. The American Society for Testing and Materials (ASTM) reported widely used reactor grades of zirconium alloys. Commercial Zirconium alloys and their compositions were mentioned in Table 2.6. Zircaloy-2 (Grade R60802) has been predominantly used as fuel cladding in Boiling Water Reactors (BWR) and as calandria tubing in CANadian Deuterium Uranium (CANDU) reactor types. Zircaloy-4 (Grade R60804) has no nickel and increased the iron content for less hydrogen uptake in certain reactor conditions for eliminating the hydrogen embrittlement problem. The alloy is typically used as fuel cladding in Pressurized Water Reactors (PWR) and CANDU reactors. Controlled composition Zircaloy offers optimized in-reactor corrosion resistance by adjusting the alloy aim point within the ASTM specification ranges. Zircaloy-4 has lower tin (1.3%) and higher iron (0.22%) than the standard grade. Zr-2.5Nb (Grade R60904) is a binary alloy with niobium to increase the strength [8, 49]. The alloy has been utilized for pressure tubes in CANDU reactors. Non-reactor grade Zirconium 702 (Grade R60702) has 4.5% maximum hafnium.

Table 2.6: Composition of commercial zirconium alloys

Alloy	Tin	Iron	Chromium	Nickel	Niobium
Zircaloy-2	1.2-1.7	0.07-0.20	0.05-0.15	0.03-0.08	-
Zircaloy-4	1.2-1.7	0.18-0.24	0.07-0.13	-	-
Zr-2.5Nb	-	-	-	-	2.4-2.8

Zircaloy-2 and Zircaloy-4 have a hexagonal close-packed (HCP) crystal structure at room temperature which is alpha phase. The beta phase is body centered cubic (BCC) and begins to form upon heating around 810 ^{o}C. The complete beta transform occurs at 980 ^{o}C temperature. Zircaloy exhibits anisotropy as a result of the HCP crystal structure. The hexagonal crystal deforms by both slip and twinning to produce a strong preferred orientation of the crystals (texture) during cold working. The anisotropic properties of Zircaloy strip results in significantly higher yield strength values in the transverse direction due to the orientation of basal planes orientation about 35 degrees.

Pure zirconium has low strength and low corrosion resistance in water reactors. Up to mid 1980's only four commercial alloys were used. For fuel assembly Zircaloy-2, Zircaloy-4 and Zr-1Nb are used and Zr-2.5Nb for pressure tubes. The total supply of the Zirconium is 7000 mt [50] in which 5000 mt can be used in nuclear sector and 2000 mt is used in non nuclear sectors. It is important to note that about 70% of all metallic zirconium goes into the nuclear industry which utilizes the element's property as a low neutron absorber. The amount used by different countries through the total supply of 7000 mt is Wah Chang 2000 mt, Cezus 1800 mt, Toshiba-Westinghouse 1000 mt, China 800 mt, India 400 mt and Russia 1000 mt as shown in Figure 2.4, Zirconium alloy uses in nuclear and non nuclear applications are shown in Figure 2.5.

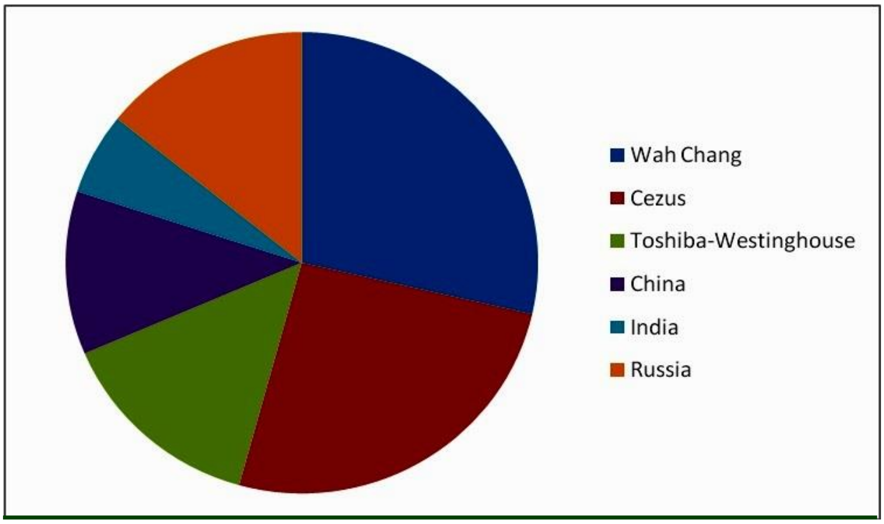

Figure 2.4: Total zirconium supply by different countries [50]

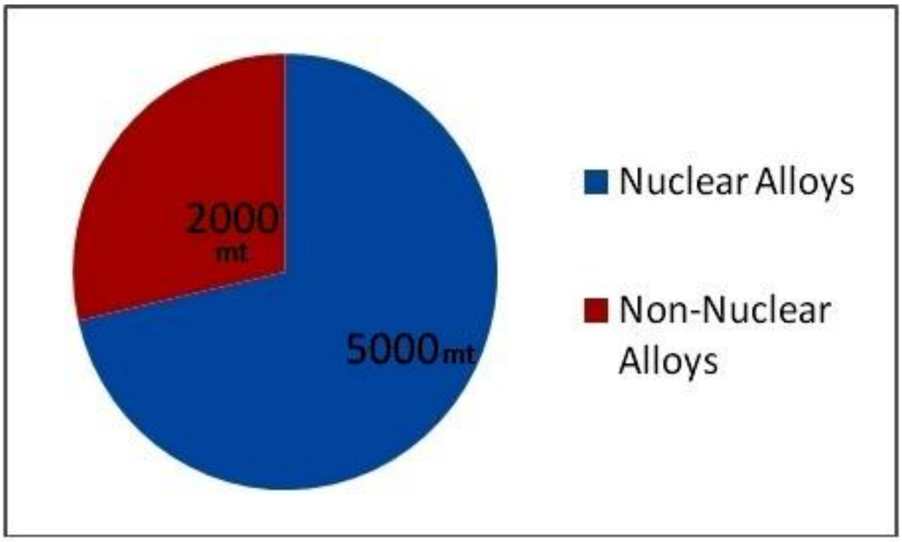

Figure 2.5: Zirconium alloy uses in nuclear and non-nuclear fields [50]

2.3 Oxide Dispersion Strengthened (ODS) Alloys

Oxide Dispersion Strengthened (ODS) alloys are very important high temperature alloys for many areas due to their thermal stability and high strength at high temperatures. Oxides are different from their metals. They have higher melting point and mostly the metal and oxides differ from their inter-atomic bonding. The main advantage of ODS alloys is their ability to maintain high strength and creep resistance at elevated temperatures of the order of 80% of the matrix melting point [51, 52]. In oxide dispersion strengthening process, the resistance to the motion of dislocation is increased by introducing finely divided hard particles of second phase in the matrix. The increased hardness and T.S. is due to the interaction of the stress field around the particles with the stress field of a moving dislocation and also due to a physical obstruction by the hard particles to the moving dislocations [53]. The dispersion particles are normally oxides carbides, borides, etc.

The extent of strengthening or hardening produced depends upon the amount of second phase particles, characteristics and properties of second phase and particle size, shape and distribution. As the amount of second phase increases, hardness increases. For a given amount of second phase, the hardness and T.S. depend on the particle size, shape and distribution [54, 55]. Too fine and too course particles have less hardening and strengthening effect. The distance between the particles i.e. the inter particle distance depends on their size. Finer the particles, lesser is the inter particle distance because the particles come closer to each other. Coarser the particles, more is the inter particle distance. Therefore maximum hardening/strengthening is observed at some intermediate spacing of particles, not too small and not too large (10^{-4} cm). Amongst the round, disc and needle shaped particles, needle shaped particles have better hardening and strengthening effect. For better and uniform properties, the distribution of particles should be uniform. The optimum properties are usually observed at a concentration of particles from 2 to 15% by volume [56, 57].

The increase in yield strength due to very hard and inert fine particles is given by:

$$\tau = Gb/l \tag{2.1}$$

where, G is the shear modulus of the crystal, b is the Burger's vector and l is the mean spacing between the particles. The above equation gives the stress necessary to move a dislocation line of length l pinned at both the ends with a Burger's vector of b i.e. to operate a Frank-Reed source of length l through a matrix of shear modulus G.

Sintered aluminum powder (SAP) and thoriated polycrystalline tungsten are the common examples of this type. Hard alumina particles are dispersed in soft aluminium matrix and thorium dioxide particles are dispersed in tungsten [58]. Another common class of ODS alloy is thoria dispersed nickel system.

2.3.1 High Temperature Applications of Various ODS Alloys

Oxide-dispersion-strengthened (ODS) alloys have potential for use in demanding elevated-temperature environments, such as aircraft turbine engines and heat exchangers. Some industrial applications of ODS alloys are mentioned in Table 2.7. These alloys possess good elevated-temperature strength and over-temperature capacity plus excellent static oxidation resistance [59, 60].

Table 2.7: Industrial applications of ODS alloys

Industry sector	Alloy base	Component/application
Aerospace/military	Fe	Gas turbine combustor liners Fuel nozzles shrouds.
	Ni	Turbine, compressor blades, nozzle guide vanes.
	Al	Low density aerospace forgings, spars, ribs, wing tip panels, compressor vanes, torpedo hulls Spars, ribs, wing tip panels, compressor vanes, torpedo hulls.
Automotive	Fe	Diesel fuel inlet atomizer Turbo chargers.
	Ni	Recombustors.
	Al	Composite pistons, compressor rotors, vanes, impellors.
Power generation	Fe	Burner nozzles High temperature heat exchangers
	Ni	Gas turbine compressor blades.
Furnace furniture etc	Fe	Nozzles, stirrers, insert tubes–glass, Furnace skid rails, charge carriers, Creep/fatigue rig test bars, Heating element wires.

2.3.2 Synthesis of ODS Alloys

The interest of high temperature materials includes not only advanced alloys, but also oxide and non oxide ceramics. Synthesis and the processing of high temperature materials can be hard. Different material processing techniques, such as casting and sintering are performed above the application temperature, which is difficult for high temperature materials. One can find difficulty in the joining of high temperature materials from individual materials. High temperature processes are of energy hungry techniques. Minimizing the energy loss and improving energy efficiency during high temperature material processing appeared to be an important target to work for developing a new product line. High melting points of high temperature material make powder metallurgy the method of choice for fabricating components from these metals [61, 62]. Ceramic dispersion in base alloys becomes more difficult with increasing melting temperature. Low temperature alloys can be mechanically stirred while they are liquid. Noble metals can have reactive components that oxidize in situ to form nanometer sizes dispersed ceramics. Processing alloys with high melting temperature components is almost exclusively done through powder metallurgy [63, 64].

For low temperature alloys, such as aluminum and magnesium, the large two-phase or slush region encountered on solidification allows mechanical alloy dispersion. These alloys can be sheared by flowing through a porous ceramic filter, as is standard casting practice, or mechanically agitated with a ceramic or ceramic coated impeller. Metallic impellers are susceptible to liquid metal corrosion even when fabricated from refractory metals. To overcome the surface tension of the metal, shear dispersion requires a significant amount of mechanical agitation [65].

High temperature oxide dispersion strengthened alloys are most commonly mechanically alloyed and mixed via ball milling and powder pressing. By mechanically mixing of powders there may be reduction of particle size to the order of ~1µm and energy can be stored on the free surface of each particle. There is also a substantial enthalpy gain from the introduction of dislocations during the severe plastic deformation during milling [66]. This energy is then released in the sintering step to reduce the total energy of the system. The release of surface energy allows the grains to remain small and prevents solute segregation. Powder metallurgy finds much of its roots in research that was performed do develop high temperature oxide dispersion strengthened alloys. The achievements in ODS alloys started from Thoriated tungsten in 1910, SAP Aluminum in 1950, Thoriated (TD) Nickel in 1960 and to TD Nichrome around 1965 [67].

2.4 Mechanical Alloying

Mechanical alloying (MA) is a notable process to produce super alloys and nano structured materials at room temperature [68, 69]. MA technique involves powder processing in a high energy ball mill. In the beginning it was difficult to produce nickel base super alloys due to their thermal instability. After long search to find the way of producing high temperature alloys, MA was found to be a suitable technique. Development of such high-temperature alloys can only be possible by mechanical alloying to avoid the disintegrated melting casting processing route. Starting from the blended elemental powders to homogenization of alloy MA has capable of synthesizing a variety of equilibrium and non-equilibrium phases. Including supersaturated solid solutions, MA has proven its potential in producing variety of metastable, quasi crystalline phases, nano structures and amorphous alloys [70, 71].

It is known that alloying is a process to make an alloy (metallic substance) made by mixing and fusing one metal with one or more than one metal or nonmetal, to obtain desirable qualities such as hardness, strength etc. and it is the common technique at least for low temperature materials. MA has been discovered as easily carried out technique for high temperature material and for the production of nano-powder [25]. From the past 50 years the chronological development of MA was mostly concerned with the development of ODS (Oxide Dispersion Strengthened) alloys. Currently there has been a wide research for novel applications of MA products and is also continuing for developing newer and better materials through MA. From the early 1970’s to 1990’s there has been a rapid development of mechanical alloying in producing ODS alloys, amorphous materials, nano crystalline phases etc. Alloys produced by mechanical alloying were given in Table 2.8.

Table 2.8: Alloys produced by MA in the mid 1990’s [12, 14, 23, 27, 28, 29]

Type of Material	Alloys
Light alloys	Al-Mg-Li
ODS alloys	FeCrAl+Yttria; Al-Fe-Ce (RS)
MMCs	Al-SiC
Intermetallics	Cr3Si; MoSi2; NiTiAl
Cermets	Ni-TiC (reactive milling)
Metastable systems	Fe-Zr; Co-Zr (amorphous/glassy)
Nano-crystalline materials	Cu-Ta; Fe-Ta-W
Superconductors	Si-Pb (metallic); Ba-Ln-Cu (ceramic)
Super-corroding alloys	Mg-Fe
Magnetic materials	Fe-Nd-B

The chronological development of mechanical alloying was given in Figure 2.6 and Figure 2.7 which indicates the publications concerning materials developed by mechanical alloying.

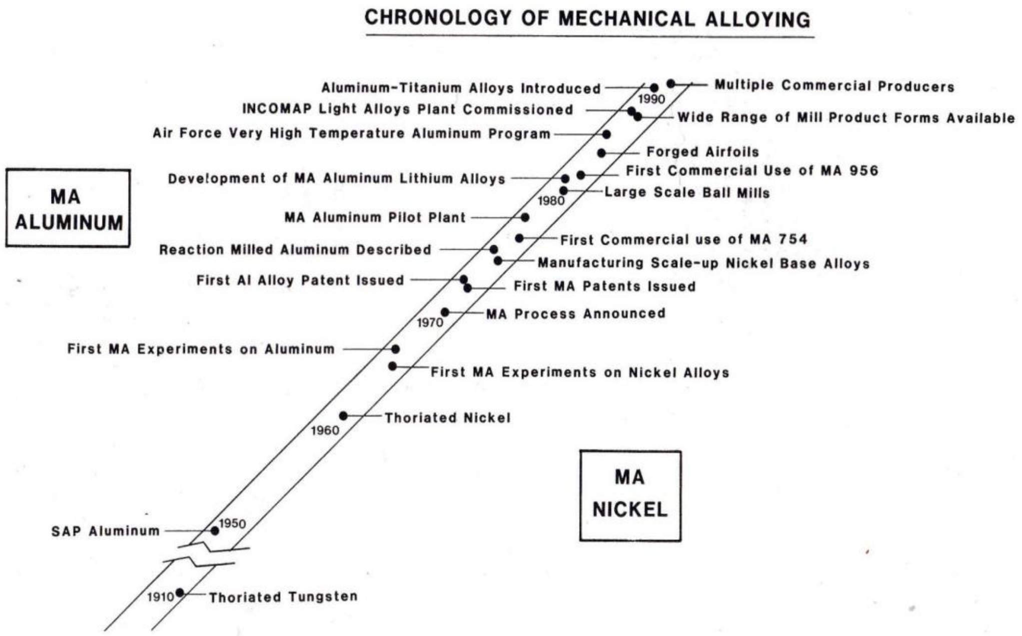

Figure 2.6: Chronological developments of mechanical alloying [72]

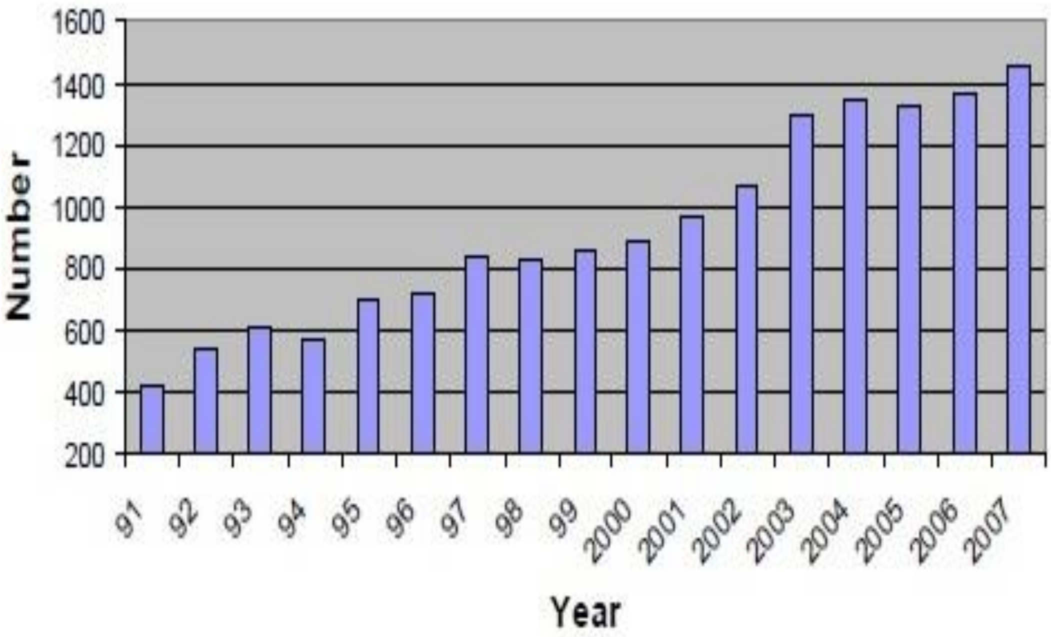

Figure 2.7: Number of publications concerning materials developed by mechanical alloying [28]

Some breakthroughs in the development of mechanical alloying are [64]:

- In 1966 The International Nickel Company (INCO) developed ODS nickel-base alloys for turbine applications.

- In 1970 ball mill technique was developed to produce oxide dispersion strengthened alloys for high temperature structural applications.
- In 1983 MA method has been successfully employed for the formation of $Ni_{60}Nb_{40}$ amorphous alloy.
- In 1987/88 Synthesis of nano-crystalline phases and in 1989 Synthesis of quasi-crystalline phases reported.
- In 1998 homogeneous nano composites of Al and SiC has been prepared.

2.4.1 Potential of Mechanical Alloying

Powder metallurgy begins with the production of metal or non metal powders. There are various methods for the manufacture of powders and each method gives a powder of different size, shape and distribution and has different characteristics. Therefore a right type of powder in the correct proportion must be used for obtaining the desired properties in the final sintered product.

MA is able to synthesize advanced materials by bringing them to metastable state or non equilibrium state by external dynamical forces [73, 74]. These dynamical forces would be in the form of either thermo dynamical or physical. Thermo dynamical processes involve melting, evaporation, and irradiation are waste of energy. Different methods like solid state quenching, rapid solidification, irradiation/condensation from vapour operates at different heating/quenching rates. Among the physical processes, mechanical alloying has high departure energy from equilibrium [75]. Different types of processes and their departure energies from equilibrium are mentioned in Table 2.9.

Table 2.9: Different techniques and their heat/quench rate, and departure energies from equilibrium [12, 74]

Processes	Techniques	Heat/Quench rate (K/s)	Departure energies from equilibrium (kJ/mol)
Thermal	Solid state quench	10^3	16
	Rapid solidification	10^5-10^8	24
	Irradiation/ion implantation	10^{12}	30
	Condensation from vapour	10^{12}	160
Physical	Mechanical alloying	-	30
	Mechanical cold work	-	1

With the above mentioned 30 kJ/mol Maximum departure energy from equilibrium, Mechanical Alloying improves grain refinement, homogeneous dispersion of oxide, and the formation of non-equilibrium phases, leading to better mechanical and high-temperature properties.

In early 1970’s, Benjamin and co-workers [76] found that during milling, the oxide layers formed on the surface of powder particles of nickel or aluminium in an oxidising atmosphere, are fractured and further these oxides are incorporated into the solid powder particles via cold welding. In early 1980’s, Koch [77] reported milling of Ni and Nb mixer for a long time that produced an amorphous alloy powder. Mc. Cormick and Schaffer [78] reported that chemical reactions occur between Ca and CuO prompted by high-energy mechanical milling.

The most important application of mechanical alloying is synthesis of ODS alloys. These alloys have typical compositions and it is difficult to process them through conventional metallurgy methods. Mechanically alloyed materials are strong both at room and elevated temperatures. The elevated temperature strength is derived from different mechanism. First, the uniform dispersion of very fine oxide particles (commonly used are Y_2O_3) which are stable at high temperatures, obstruct dislocation motion in the metal matrix, and increase the resistance of the alloy to creep deformation. Another function of the dispersoid particles is to impede the recovery and recrystallization processes, which allow a very stable grain size to be obtained. These grains resist grain rotation during high-temperature deformation. Moreover, the homogeneous distribution of alloying elements during MA gives the solid solution strength.

2.4.2 Effect of Mills on Mechanical Alloying

The effect of MA depends on some important factors in the fabrication of homogeneous materials. The main factor that effects the particle size distribution, degree of disorder and amorphization is the type of mills [77, 78]. The attritor was invented by Szegvari for vulcanization process of rubber. The first high energy ball mill was attritor ball mill and was used by Benjamin. Generally high-energy milling equipment is used to produce mechanically alloyed powders. The main differences between those mills are their capacity, efficiency of milling and additional arrangements for cooling, heating, etc. Planetary mills, vibratory mills and ball mills are the mostly used in Laboratories. Some mills and their capacities are mentioned in Table 2.10.

Table 2.10: Mills and their capacities [67]

Mill type	Maximum Sample weight
Mixer mills	40g
Planetary mills	1000g
Uni-ball mill	8kg
Attritors	100kg

SPEX shaker mills: These mills are used for laboratory uses to mill about 10±20 g of the powder at a time.

Planetary ball mills: A few hundred grams of the powder can be milled at a time. The highest speed is 360 rpm.

Attritor mills: Attritors are the mills in which large quantities of powder (0.5 to 40 kg) can be milled at a time. The capacity (volume) ranges between 3.8×10^{-3} m^3 to 3.8×10^{-3} m^3. The rotational speed about 250 rpm (4.2 Hz).

Commercial mills: Commercial mills are used for industrial purposes, to produce up to about 1250 kg capacity.

Initially the starting elemental powders usually agglomerate at the early stage of milling in ball milling process to form powder particles of greater diameters, up to several hundred microns, and this is followed by continuous disintegration until the particle size is less than a few microns. Some of the mills and their milling processes were shown in Figure 2.8.

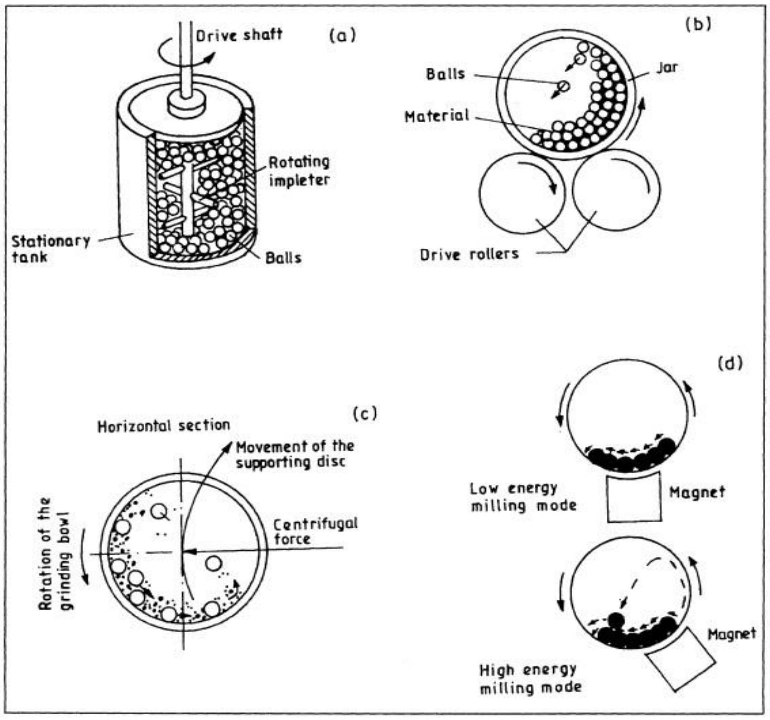

Figure 2.8: Milling process in some of the mills [81]

2.4.3 Mechanism of Mechanical Alloying

The actual process of MA starts with mixing of the powders in the right proportion and loading the powder mix into the mill along with the grinding medium. This mix is then milled for the desired length of time until a steady state is reached when the composition of every powder particle is the same as the proportion of the elements in the starting powder mix. The milled powder is then consolidated into a bulk shape and heat treated to obtain the desired microstructure and properties [82--84].

Figure 2.9 shows the mechanism of alloying during via mechanical alloying. During high-energy milling the powder particles are subjected to repeated flattening, cold welding, fracturing and rewelding to produce quality powders with controlled microstructure. The collisions occur between ball to ball, ball to powder and ball to vial. When two balls collide, some amount of powder is trapped in between them. The impacted force plastically deforms the powder particles leading to work hardening and fracture. In case of ductile materials the powder got flattened and work hardened. Some new surfaces created by fracture and are able to weld together and this causes the increase in particle size and particle size as large as three times bigger than the starting particles can be produced. The particles get work hardened and fractured with continuous deformation by fatigue failure. After that the particle size will get reduced by the absence of agglomeration [76, 81]. Further application of forces fracture predominates over cold welding. Due to the continued impact of grinding balls, the structure of the particles is steadily refined, but the particle size continues to be the same.

During MA, heavy plastic deformation is introduced into the particles due to the high energy milling. This deformation causes crystal defects such as dislocations, vacancies, stacking faults, and increased number of grain boundaries.

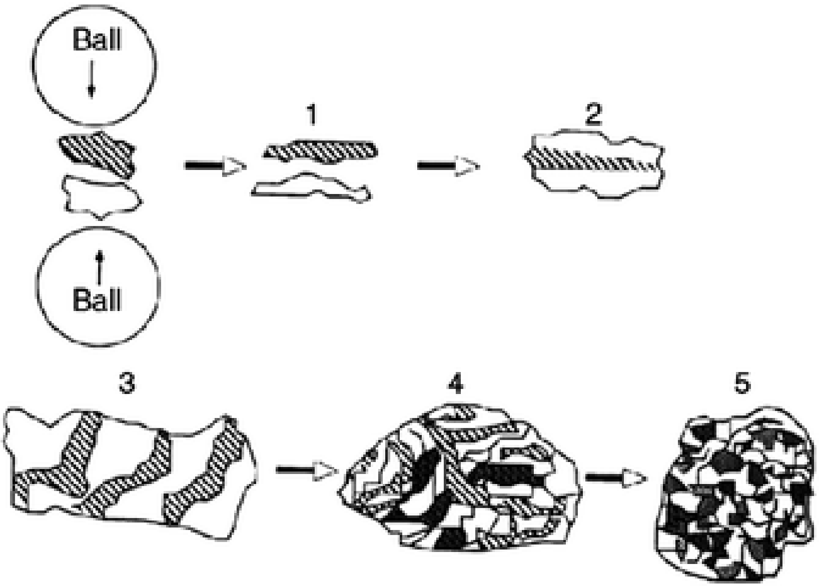

Figure 2.9: Steps of powder evolution during mechanical alloying [85]

2.4.4 Thermodynamic and Kinetic View of Mechanical Alloying

The extent of welding and fracturing depends on deformation behavior and temperature induced by ball-powder-ball impact. The kinetics of amorphous, nano crystal and intermetallic phase formation during milling can be the milling temperature driven. Shen and Koch [86] reported that smaller crystallite size was obtained at 188 K temperature compared to room temperature milling. At low milling temperature the size of CoZr intermetallics are smaller. During milling large temperature rise may happen due to some exothermic reaction. Milling at subzero temperatures prevent additional welding whereas fracture is favoured at low temperature due to the deformation characteristic of powder. There have been some reports on microscopic temperature of the mill. Davis and Mc Dermott [87] reported the maximum temperature rise in Spex mill was 323 K, Kimura [88] reported 445 K for attritor. Borzova and Kaputkin [89] reported 373-488 K for attritor using SiC and diamond sensors. Kuhn [90] reported 120 K temperature rise in vibratory mill. The temperature of the powder for the instant impact could be high. Schwarz and Koch [91] measured the temperature rise of 40 K for $Ni_{32}Ti_{68}$ and $Ni_{45}Nb_{55}$ powders in a Spex mill. Davis and Koch [92] predicted the temperature rise was less than112 K in above system by using previous approaches.

Schwarz and Johnson [93] mentioned the thermodynamic and kinetic principles for solid state amorphization with multi layers of A and B constituents. For producing A-B binary alloy, there should be a negative heat of mixing between the A and B, there should be a large imbalance in the diffusion coefficient of one in the other (i.e. $D_B >> D_A$) [94]. Yavari and Desre reported the thermodynamic and kinetic requirements for amorphization during mechanical alloying. Even they have mentioned that for amorphization of A-B alloy there should be a large negative heat of mixing and the inter-layers should be below a critical thickness with $\Delta H_{mix} \backsim 0$. This distinction is due to the fact that amorphous phase undergoes work softening and the crystalline phase work hardening during mechanical alloying. The conclusion they have made, amorphous phase occurs even when $\Delta H_{mix} \backsim 0$ and $D_B \backsim D_A$ [95].

Amorphization during MA is not entirely a mechanical process and the amorphous phase forms by reactions within the solid state. Haruyama and Asahi [96] have prepared amorphous Ni-Zr alloy (Ni_xZr_{100-x}, x=20-70) by mechanical alloying for 30 hours milling in a high speed vibratory mill. The heat of mixing is mostly negative for intermediate compositions. Lee [97] has reported that the Fe-Zr system has got solid state amorphization obtained by inter-diffusion between layers and further milling results in crystallization of amorphous phase in to α-Fe, and Zr_2Fe crystalline phases. These things happen due to increase in free energy through accumulation of structural defects such as vacancies, dislocations, grain boundaries and anti-phase boundaries.

Computational thermodynamic is one way to resolve the problems of materials, which arises with temperature. During MA process high amount of energy can transfer from balls to powder by milling. High plastic deformation in powder particles leads in creating defects such as dislocations and grain boundaries, which increases the free energy of the system [95]. The increase in free energy due to the decrease of grain size can be determined by the equation

$$\Delta G_b = \gamma \, (A/V) V_m \tag{2.2}$$

where, γ is the grain boundary energy, A/V the surface/volume ratio and Vm is the molar volume. A cubic or spherical form of grain size is assumed to estimate the A/V ratio. The change in free energy due to the variation of dislocation density can be calculated by the equation [98]

$$\Delta G_b = \xi \rho \, V_m \tag{2.3}$$

where, ξ is the dislocation elastic energy per unit length of dislocation lines and ρ is the dislocation density. The smallest grain size L, can be estimated, for one metal, using following equation [99] proposed by Nieh and Wadsworth.

$$L = 3Gb/H\,(1-\upsilon)\,\pi \tag{2.4}$$

where, G is the shear modulus, b the burger vector, v the Poisson's modulus and H is hardness. Thus, the stored energy was sufficient to increase the solubility between metal systems which had positive Gibbs free energy of mixing [100].

The particle size reduction efficiency of conventional ball mills was around 0.1%, this is very low. But in case of high energy ball mills the efficiency was somewhat higher than that of conventional mills. However the efficiency of high energy ball mill is less than 1% [12]. The remaining energy has been lost mostly in the form of heat and small amount of energy is utilized in the elastic and plastic deformation of the powder particles.

2.4.5 Zirconium based ODS Alloys

Since 1980 many techniques have been used to prepare nanostructured or amorphous metals and alloys. All these techniques involve quenching rate above 10^5 K/min such as rapid solidification techniques (melt spinning, laser melting, splat cooling etc.), solid state quenching, irradiation and condensation from vapour. These melting casting routes are not suitable, due to the thermal instability of alloying elements at high temperatures causes the anisotropic properties of the end product. Development of such high-temperature alloys can only be possible by mechanical alloying to avoid the disintegrated melting casting processing route. Assisting high energy deformation by mechanical alloying, amorphous alloys can be produced [28, 101]. The Melting point of Zirconium is 1855 ^{o}C. Below 865 ^{o}C, Zirconium has a hexagonal packing structure (α-phase) which transforms into a bodycentred cubic structure (β-phase) above this temperature. It is impossible to obtain this β-phase at room temperature with any type of heat treatment. In this situation the solid state powder processing techniques are of favorable consideration and mechanical alloying has proven as the potential process even for the production of oxide-dispersion strengthened zirconium alloys.

Zr-Cu is the first metal-metal system in which amorphization was studied by rapid solidification. Amorphous hydride was formed due to the reaction of hydrogen with Zr and Rh by mechanical alloying. This solid state amorphization reaction was reported in 1983 [102]. Zr based alloys shows amorphization at much lower cooling rates. But the preparation of ternary, quaternary alloys is challenging due to high melting temperatures and low solid solubility of alloying elements. Mechanical alloying is adopted to alloy elements those are difficult to alloy by conventional processing routes. Moreover formation of extended solid solubility with controlled microstructure without the need of high temperature is possible by mechanical alloying. Mechanical alloying can also be used to produce nanocrystalline materials and is also capable of producing variety of alloy compositions.

Fundamentally and industrially, intermetallic compounds are of great interest having high strength and corrosion resistance at high temperature. MA allows the formation of intermetallic compounds between Zr and Fe [103]. Zirconium alloy system exhibit wide supercooled liquid region. But changes in the composition effects the supercooled liquid region. So, the alternative processing route for the preparation of amorphous alloys with extended supercooled liquid region is mechanical alloying. The progress of amorphization by solid state reaction also can be possible by MA [19, 104, 105].

The concept of oxide dispersion strengthening (ODS) is considered to increase the strength of the zirconium-based alloy up to high temperatures. ODS alloys can be used for structural material components in nuclear power plants, since such alloys have a high mechanical strength at high temperatures, even of up to 800 ^{o}C. This type of alloy is generally manufactured through mechanical alloying from its source metal and dispersiod powders.

Zirconium alloys can be used at high temperature because of their high recrystallization temperature. But low temperature hexagonal (α) zirconium has a very low solubility of hydrogen, resulting in any excess hydrogen getting precipitated as zirconium hydride. This leads to embrittlement, delayed hydride cracking (DHC) and hydride blistering, all of which limit the lifetime of reactors and cause serious environmental concerns in spent nuclear fuel rod [106, 107]. In addition, zircaloy-4 shown to perform extremely favorably in case of reducing hydrogen uptake relative to earlier Zr alloys. With regards to both crack initiation and subsequent DHC propagation research results have been used to determine the life of pressure tubes. Inert particle strengthening concepts were extended to zirconium-base alloys for high temperature applications.

Zirconium alloys are good to improve corrosion resistance and high compressive stresses due to the oxide dispersion. By using powder metallurgy techniques inert particles of Y_2O_3 were mechanically dispersed in a Zircsloy-2 matrix. The elevated temperature yield strength of Zircaloy-2 was increased. Much of the increase was related to oxygen contamination. At 344 ^{o}C, the creep resistance of ODS Zircaloy-2 was high than the

Zircaloy-2. The dispersion of nano Y_2O_3, results in increasing the corrosion resistance in 400 ^{o}C steam [108]. In case of powder metallurgy process of dispersion-strengthened zirconium alloys, oxygen contamination is the major technological problem. Alloy additions of Be are suggested for minimizing both the corrosion and oxygen contamination problems. Corrosion tests in supercritical water and 500 ^{o}C steam were performed by the Minerals, Metals & Materials Society on Zr-based model alloys up to 132 days to evaluate the potential use of Zr alloy cladding in the supercritical water reactor (SCWR) [109].

Zr-based powders alloyed in attritor mill with 7 vol % dispersions of La_2O_3, ThO_2 and Y_2O_3 was reported. The oxide particle size was larger and the dispersion achieved was not optimum desired dispersion strengthening [58, 110]. Antony and Klepfer [111--113] dispersed 0.1, 1 and 10 vol % yttria in Zircaloy-2 hydride mill scrap and produced material by vacuum hot pressing at 1125 ^{o}C temperature with subsequent beta quenching and extrusion at 815 ^{o}C temperature. Again the particle parameters were not suitable for significant dispersion strengthening and a well defined interpretation of the results was not possible due to the oxygen contamination of the scrap material [114].

A more detailed and comprehensive study was carried out by Rezek and Childs [115]. Milled zirconium hydride sponge was re-milled with suitably prepared yttria powder and the resulting mixed powder was cold compacted and sintered at temperatures generally in excess of 1000 ^{o}C. The material was fully densified by hot rolling, clad in mild steel. It was also noted that particle distribution was improved by rehydriding and reprocessing. At a sintering temperature of 1000 ^{o}C the average particle diameter was about 200 nm. No tensile measurements were reported but stress rupture properties at 500 ^{o}C for Zr-5 vol % yttria alloys showed a 10-fold improvement.

P.O. Parsons and E. Adolph [116] studied the mechanical properties of Zircaloy-2 alloys containing yttria particles and was compared to some other zirconium alloys, Zircaloy-2 and zirconium-2.5 wt. % Nb. The comparisons show that the dispersion- strengthened alloys are worthy of further development.

2.5 Sintering

Sintering is carried out to increase strength and hardness of a green compact and consists of heating the compact to some temperature under controlled conditions with or without pressure for a definite time. Until the 1930's, sintering was defined as a technological process of obtaining sintered materials from powder systems. In 1930, F. Sauervald reported the problem of sintering after that in 1934, V. Trzebyatovski and M.Yu. Balshin supported his theory. Later Balshin mentioned sintering means forming contacts between particles during heating of a dispersion system [21].

Sintering process concerns with:

Diffusion: This takes place especially on the surface of the particles at elevated temperature [117]. Nanostructures obtained by mechanical alloying promote the diffusion process by increasing the surface area required for diffusion.

Densification: This decreases the porosity present in the green compact and increase the particle contact area. Due to this effect compact size decreases but this may not occur uniformly because of variations in the density of compact and hence distortions of component may arise.

Recrystallization and grain growth: This occurs between the particles at the contact area, leading to formation of the original one. The main driving force for sintering is the decrease in free energy due to decrease of surface area.

2.5.1 Conventional Sintering

Depending on the temperature of sintering, sintering process is classified as solid phase sintering or liquid phase sintering. The most common method is solid phase sintering in which the green compacts are heated usually above the recrystaliization temperature. The liquid phase sintering is carried out above the melting point of one of the alloy constituents or above the melting point of an alloy formed during sintering. The first physical theory of liquid phase sintering was established by Ya. I. Frankel in 1945. In 1946, B. Ya. Pines proposed a theory on solid state sintering. Frenkel approach of sintering theory [118] was coalescence of viscous particles driven by surface tension and Pines approach for solid phase sintering was evaporation of emptiness [119].

For conventional sintering usually a green compact needs to be prepared externally using a suitable die and hydraulic machine for applying the necessary pressure. After this the green compact is sintered in a furnace [120].

The sintering process is governed by some parameters such as temperature and time, geometrical structure of the powder particles, composition of the powder mix, density of the powder compact and composition of the protective atmosphere in the sintering furnace.

The practical significance of these parameters can be described briefly as follows:

Temperature and time: The higher the sintering temperature, the shorter is the sintering time required to achieve a desired degree of bonding between the powder particles in a powder compact.

Geometrical structure of the powder particles: At given sintering conditions, powders consisting of fine particles or particles of high internal porosity (large specific surface), sinter faster than powders consisting of coarse compact particles. Fine powders are usually more difficult to compact than coarse powders, and compacts made from fine powder shrink more during sintering than compacts made from coarse powder.

Composition of the powder mix: If the powder mix contains a component that forms a liquid phase at sintering temperature bonding between particles as well as and alloying processes are accelerated.

Composition of the protective atmosphere in the sintering furnace: The protective atmosphere has to fulfill several functions during sintering which in some respects are contradictory. On the one hand, the atmosphere is to protect the sinter goods from oxidation and reduce possibly present residual oxides.

Due to the large surface area and high free energy of nanometric powder, there are many destructive aspects for the processing and obtaining the homogeneous microstructures. Allen et al., 1996 [121, 122]; Averback et al., 1992 [123] reported that the possibility of formation of thermodynamically unstable phases and appearance of strong effect of adsorbed gases on the surface can effects the microstructure. Many studies (Chen & Chen, 1996, 1997) [124], (Hanh, 1990) [125] found sintering of nanometric size particle was lower than those conventional sintering.

2.5.2 Spark Plasma Sintering (SPS)

High performance applications require higher densities. Conventional methods leads to lower density products in compared with hot consolidation processes (hot pressing, HIP, spark paslma sintering, extrusion etc) enable production of full-density or near full-density powder materials/products [126, 127].

Spark Plasma Sintering is a new technique which takes hardly few minutes to complete a sintering process compared to conventional sintering which may take hours or even days for the same. High sintering rate is possible in SPS [128, 129]. The heating rates normally reached in conventional furnaces are 5 to 8 ^{o}C/min which can go maximum up to 10 ^{o}C/min. So, to reach a temperature of 1200 ^{o}C we usually need 2 to 4 hours or more whereas in SPS, heating rates exceeding 300 ^{o}C/min are easily obtained hence a temperature of 1200 ^{o}C can be obtained in only 4 minutes. In the presence of pressure and electric current, localized necking occurs faster due to joule heating. Consequently, the temperature rises very fast (faster than conventional sintering and Hot pressing) and the densification is completed within few minutes [130, 131].

With SPS technique one can easily achieve high densities, which are nearly comparable to theoretical density values due to application of temperature and pressure at same time, and lowers the sintering temperature range by 200-250 ^{o}C than in conventional process. Moreover, it avoids coarsening and grain growth which in-turn results in high densities [132, 133]. This process has potential to use for powders with nano-size, nano-ceramics or nano composite these exhibits excellent mechanical properties (strength, hardness).

High reactive materials can be easily sintered because of rapid heating and cooling cycle, and avoids formation of undesirable phases. When spark discharge appears in the gap between the particles of a material, a local high temperature state occurs. This causes vaporization and melting which creates bond between the powder particles and narrow shapes or “necks” is formed around the contact area. These necks gradually grow and develop as diffusion progresses, resulting in a sintered compact of 99% density. Since only the surface temperature of the particles rises rapidly by self-heating, particle growth of the starting powder materials is controlled [22, 134].

Production of refractory metals and intermetallics (ZrB_2, Ni_3Al, FeAl and TiAl), ultra high temperature ceramics (ZrB_2, ZrC), transparent ceramics, Nano structured non-equilibrium and functional graded materials can developed by spark plasma sintering [22]. Gao *et al*., 2000 [135]; Chakravarty *et al*., 2008 [136], Bernard-Granger & Guizard, 2007 [148] studied production of polycrystalline ceramics with high density and small grain size was obtained by spark plasma sintering. Pierri *et al*., 2005 [121] observed that the small amounts of zirconia (1 vol %) presence was sufficient to cause grain growth inhibition of alumina allowing the sintering process without application of pressure that results in higher final densities and increased mechanical strength and wear resistance.

Zamora *et al* [138] reported that the reduction of crystal size to nano scale can improve the sintering kinetics and final densities. For increasing the density of powder refining is a common process in ceramic processing. Thompson *et al* [139] studied the densification of ZrB_2 with different powder particle milled in attritor mill. The reduction in particle size increased the final relative density from 70 to 97%.

2.6 Scope of this Study

Considering the uses of zirconium alloys in different high temperature fields, development of nano Y_2O_3/TiO_2 dispersed zirconium based alloy followed by conventional and spark plasma sintering is worth. It was rarely reported on development of Y_2O_3 dispersed zirconium alloys by mechanical alloying. Moreover, development of TiO_2 dispersed zirconium based alloy is different from previous one because of titanium having high thermal neutron flux. In terms of use in an application where corrosion is a major problem, zirconium is often considered together with either titanium or tantalum. So, with the alloying elements of Mo, Fe, Ni and TiO_2 dispersiod, improvement of structural properties could be possible applicable for chemical sector. So, two different ODS alloys; one, Y_2O_3 dispersed zirconium alloy for nuclear applications and other TiO_2 dispersed zirconium alloy for chemical applications were studied.

In the present work developments of these alloys by mechanical alloying was carried out and effects of following was examined:

(a) Milling parameters (Production of alloy powder with optimum speed and less processing time).

(b) Dispersoids (Y_2O_3/TiO_2) and

(c) Sintering mechanisms (Effects the physical, mechanical and oxidation properties).

Final and intermediate conditions of the powder and sintered products was characterized by:

a) X-ray diffraction (XRD), Scanning electron microscope (SEM) and Transmission electron microscope (TEM) for phase analysis and crystallite size measurement.

b) Particle size analyzer and SEM for particle size analysis.

c) Differential scanning calorimetry and thermal gravimetry (DSC/TG) for activation energy study.

d) Hardness, compression test and wear testing for mechanical property.

e) Potentio dynamic polarization for corrosion analysis.

Chapter 3

Experimental Procedure

3.1 Introduction

In this chapter, the details of raw materials and experimental techniques used are discussed. Synthesis of zirconium based alloy starts with alloy powder production by mechanical alloying route followed by consolidation and sintering techniques. The alloy powders characterization involves particle and grain size measurement, microstructural study, phase analysis and recrystallization behaviour. The characterization of sintered products involves phase and microstructural analysis, physical and mechanical property study, isothermal and non-isothermal oxidation and corrosion studies. The overall experimental work flow is summarized in Figure 3.1.

3.2 Alloy Powder Production

3.2.1 Materials and Methodology

In the present study the alloy powders were produced by mechanical alloying. The mechanical alloying starts with blending of the elemental powders for homogeneous mixer and these powder blends were milled in ball mill for desire length of time until the study state is reached. The raw materials used to prepare the desired alloys were elemental (Zr, Fe, Ni, Mo) and compound TiO_2/ Y_2O_3 powders. The source and purity of the powders are summarized in Table 3.1. The starting elemental powders of Zr, Fe, Ni and Mo (about 50-150 µm particle size) along with TiO_2/ Y_2O_3 (~40 nm) as shown in Table 3.2, were blended for 2 hours in a TURBULA (SYSTEM SCHATZ) followed by milling in a high energy ball mills.

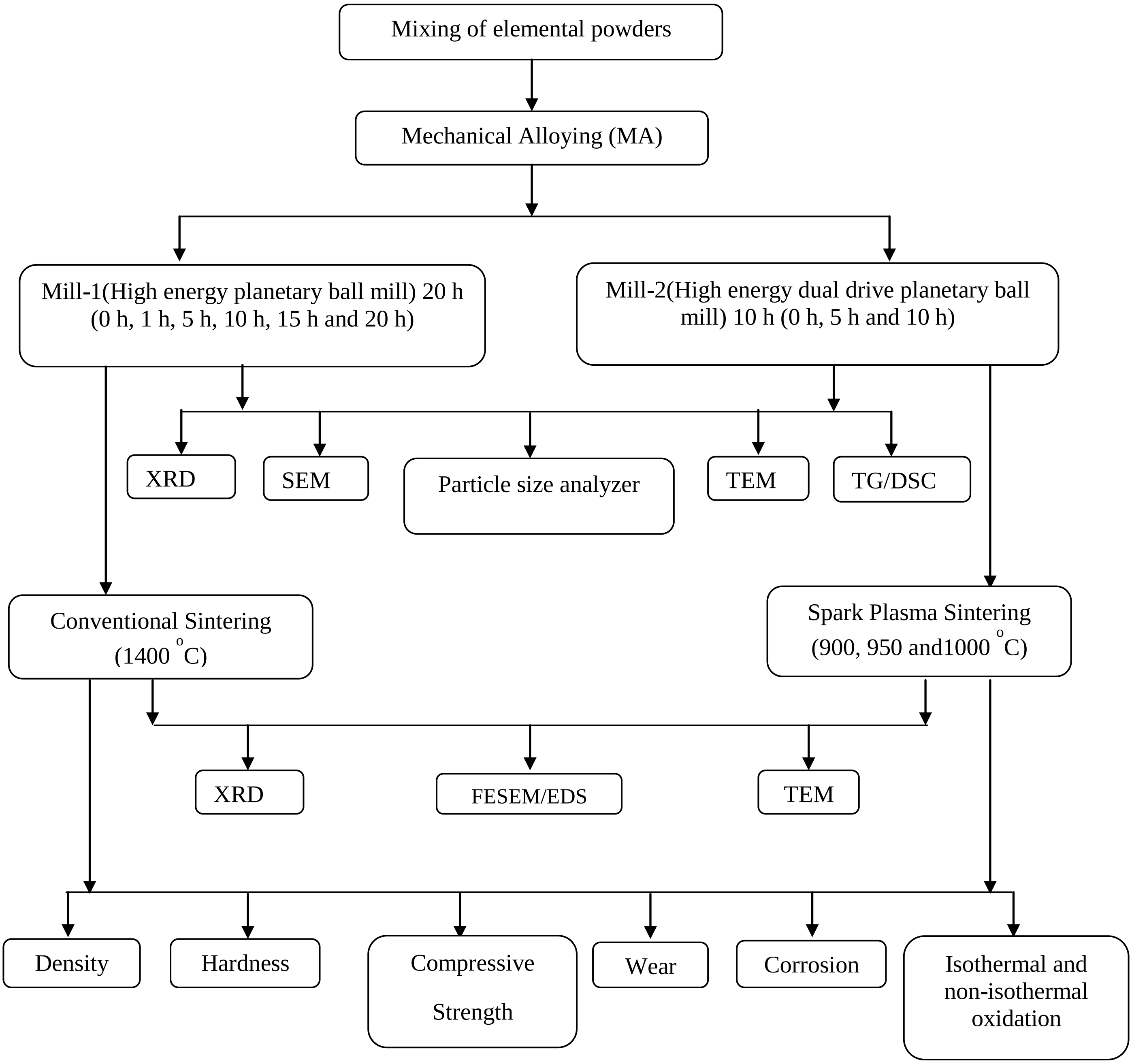

Figure 3.1: Work flow

Table 3.1: Source and purity of raw materials used in the present study

Powder	Source	Purity
Zr	Chempure Private Limited	99%
Fe	Loba Chemie Pvt Ltd	99.7 %
Ni	Loba Chemie Pvt Ltd	99.5 %
Mo	Strem Chemicals	99.9%
TiO_2	Alfa Aesar	99.9%
Y_2O_3	Alfa Aesar	99.995

Table 3.2: Initial powder composition

Alloy	Composition (Wt. %)					
	Zr	Fe	Ni	Mo	TiO_2	Y_2O_3
A	45	30	20	5	0	0
B_1	44	30	20	5	1	0
B_2	44	30	20	4	2	0
C_1	44	30	20	5	0	1
C_2	44	30	20	4	0	2

3.2.2 Mill Type

The effect of mechanical alloying mainly depends on type of mills, which affects the particle size and distribution, degree of disorderness and amorphization. Generally for producing mechanical alloy powders for a few hundreds of grams high-energy milling equipment is used. In the present study two types of planetary ball mills were used. First one is FRITCSCH, Pulverisette-5 as shown in Figure 3.2(a) and High energy dual drive planetary ball mill as shown in Figure 3.2(b).

Generally, FRITCSCH, Pulverisette-5 is used for the pulverization of soft, fibrous, hard and brittle materials. It generates a very high final fineness powder down to the submicron range. Due to the opposite rotational direction of grinding bowls and supporting disc the centrifugal forces are alternately synchronised and opposite. Thus friction results from the grinding balls and the material being ground by alternately rolling on the inner wall of the bowl, and impact results when they are lifted and thrown across the bowl to strike the opposite wall. The impact is intensified by the grinding balls striking one another. The impact energy of the grinding balls in the normal direction attains values up to 40 times higher than gravitational acceleration. The bowls have capacity of 250 ml, size of the balls was 10 mm and maximum speed 360 rpm. The bowls and balls are made of WC (Tungsten Carbide).

The dual drive planetary ball mill consists of a gyratory shaft having length of 640 mm (*L*) and two cylindrical steel jars of diameter 100 mm (*2R*) (Volume 1000 ml each), both can rotate simultaneously and separately at high speed. The shaft and Jars can rotate at the speed of 275 and 620 rpm respectively. Such high-speed rotation of both jars and the shaft makes the balls to move strongly and violently, leading to large impact energy of balls that improves the grinding performance.

(a) **(b)**

Figure 3.2: Planetary ball mills used for alloy powder processing (a) FRITCSCH, Pulverisette-5 and (b) High energy dual drive mill

The planetary mill is powered by two motors: one 5 *HP* motor works on the main rotating shaft and another 3 *HP* motor drives the jars. The rotating speed of both motors can be varied independently and continuously by a frequency controller. The design specifications of mill are reported in an article [140].

3.2.3 Milling Parameters

The morphology of the milled powders and the end product properties depends on different milling parameters such as milling media, milling time, rotational speed and balls to mixed powder weight ratio. The two mills and their milling parameters are summarized in Table 3.3. Generally metal powders are wet milled with liquid medium to avoid oxidation. To optimize the balance between welding and fracture, active organic agents may be added to the powders. Optimization speed should be chosen for the mill to obtain proper bombardment of ball to powder or ball-powder-ball or ball-powder-vial. During long milling time the temperature rise can affects the size reduction and reactions between powders. Here milling of the alloy powders were done for 20 hours in FRITCSCH, Pulverisette-5 planetary ball mill (mill-1) and 10 hours in High energy dual drive planetary ball mill (mill-2). The mechanically alloyed powders produced by mill-1 was consolidated and sintered via conventional sintering technique and the mechanically alloyed powders obtained from mill-2 was sintered by spark plasma sintering technique.

Table 3.3: Milling parameters of planetary ball mills

Planetary ball mill type	Rotational speed	Ball to powder weigh ration	Milling media (liquid)	Milling time (hour)
Mill-1(Figure 3.2(a))	300	10:1	Toluene	20
Mill-2(Figure 3.2(b))	275 (shaft), 620 (Jars)	10:1	Toluene	10

3.3 Powder Characterization

3.3.1 Phase and Microstructural Characterization

For systematic analysis of the milled powders, samples of 0, 1, 5, 10, 15, and 20 hours were collected and characterized by means of X-ray diffraction (XRD), scanning electron microscopy (SEM), and particle size analysis (Mastersizer). The crystallite sizes (L) and lattice strains (ε) of the milled constituents were analyzed by XRD using a standard diffractometer (Philips X'Pert MPD) with Ni filtered Cu K_α radiation (λ = 0.154051 nm). These parameters were calculated by means of the modified Williamson-Hall method. The compositional and morphological study was done using a JEOL/EO type scanning electron microscope/energy-dispersive spectroscope. Final milled powder was also characterized using a transmission electron microscope (JEM 1200, JEOL) with 200 kV working bias.

3.3.2 Recrystallization Behaviour

Thermal properties (glass transition and crystallization of the amorphous phase) of final milled powders of alloy A were evaluated by differential scanning calorimetry (NETZSCH STA 409 C). The scanning is done over a temperature of 200 ^{o}C to 1200 ^{o}C with various heating rates of 4, 6, 8, and 10 K/min in argon atmosphere.

3.4 Powder Densification

3.4.1 Cold Compaction

Compaction of alloy powders reduces the voids between the powder particles and increases the density of compact. It produces adhesion and cold welding of the powders and gives sufficient green strength. Pressure should be properly controlled since lower pressure gives fragile compacts and higher pressure cause tool distortion and breakage. The density of the compact depends on the pressure applied. Compaction of 20 hour milled powder of all the alloys was carried out at 1 GPa pressure for 5 minutes in a uniaxial hydraulic pressing unit. 10 mm diameter cylindrical die was used for compaction of alloy powders.

3.4.2 Conventional Sintering

The green compacted pellets of the alloys were conventional sintered in a high temperature tube furnace (evacuated to 1x 10^{-5} mbar pressure) at 1673 K (1400 ^{o}C) for 1 hour in Argon gas. The heating rate 10 ^{o}C/min and flow rate of Argon gas 100 ml/min were maintained.

3.4.3 Spark Plasma Sintering

The blended powders were sintered by SPS technique at three different temperatures of 1173 K (900 ^{o}C), 1223 K (950 ^{o}C) and 1273 K (1000 ^{o}C) under a constant pressure of 50 MPa and dwell time 5 minutes with a constant pulse on: off ratio of 12:2 and each pulse duration of 3.3 min were maintained in a spark plasma sintering unit, SCM 1050 (Sumitomo Coal Mining Co. Ltd., Japan).

Figure 3.3 shows the schematic diagram of SPS process used in the present study. SPS consists in applying uniaxial force and ON-OFF DC pulse energizing. The ON-OFF DC pulse voltage and current creates spark discharge and Joule heat points between material particles (high-energy pulses at the point of intergranular bonding) as shown in Figure 3.4. The high frequency transfers and disperses the spark/Joule heat phenomena throughout the specimen, resulting in a rapid and thorough heat distribution, high homogeneity and consistent densities. Current lines will spread in different ways depending on the geometry of sample, die and electrical resistivity. The molds were made of graphite, load can apply upto100 kN and the vacuum level was upto 6 Pa. The process is carried out by two stages; initially, the powder compacts were loaded to 50 MPa at 500 ºC for 3 min to remove the absorbed gases within the powder particle surface. After degassing, the compacts were further heated to the sintering temperature of 900 ºC to 1000 ºC with uniaxial pressure at 50 MPa for 5 min (shown in Figure 3.5).

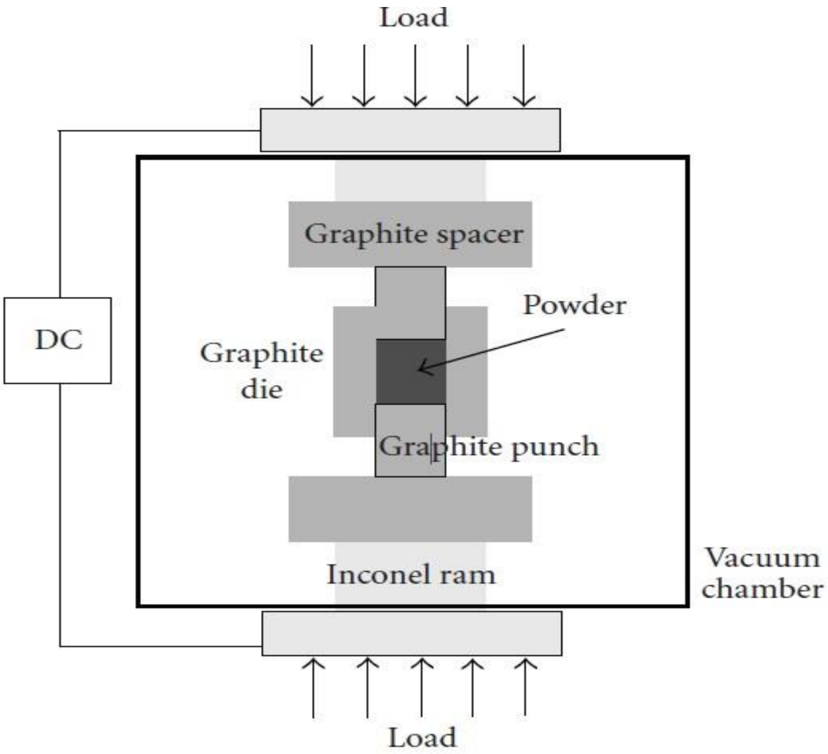

Figure 3.3: Schematic drawing of the SPS process

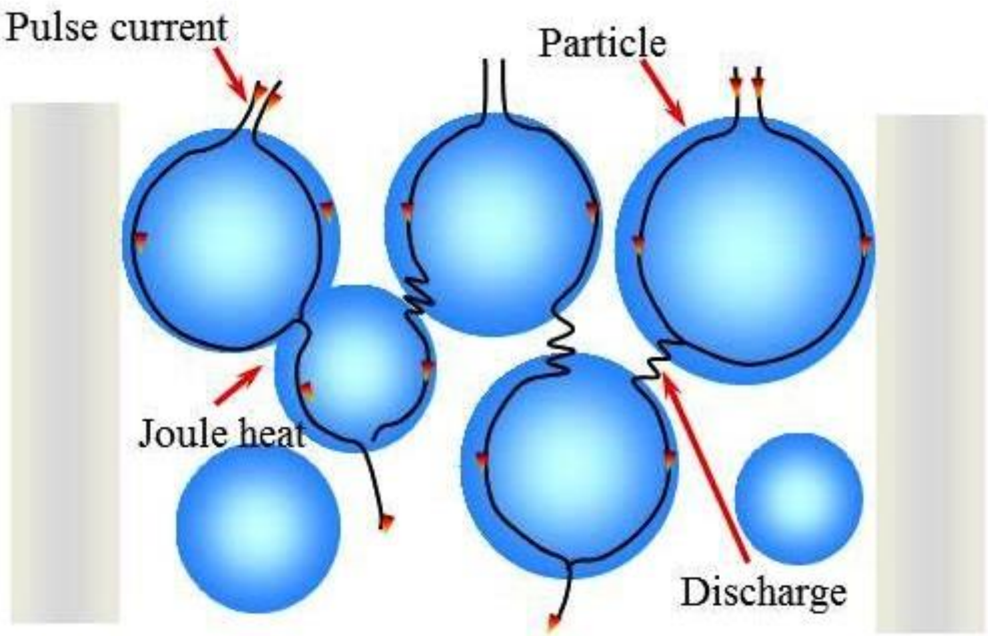

Figure 3.4: ON-OFF pulsed current path through the powder

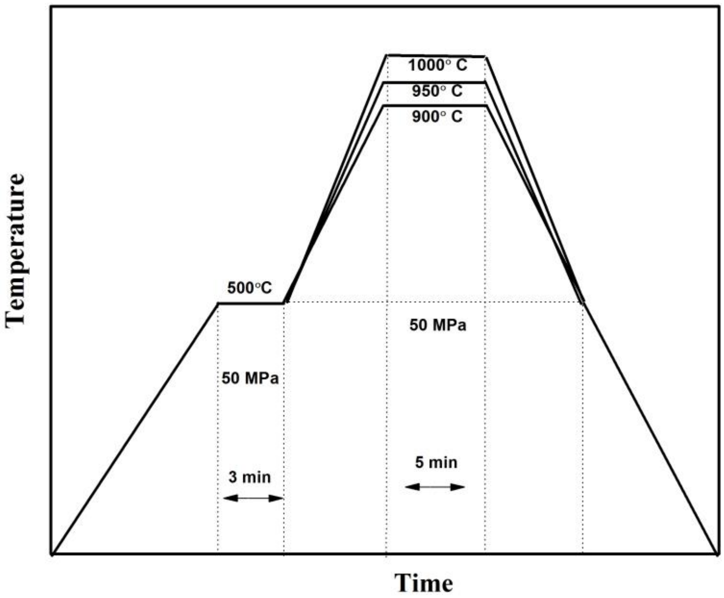

Figure 3.5: Thermal cycle and load variation at different temperature during spark plasma sintering

3.5 Characterization of Sintered Products

3.5.1 Phase and Microstructural Characterization

To study the phase evaluation and morphology of both conventional and spark plasma sintered products the samples were characterized by X-ray diffraction (XRD), scanning electron microscopy (SEM) and Transmission electron microscope (TEM). The morphologies and chemical compositions were studied by using a JEOL/EO type scanning electron microscope and Nova Nano SEM/FEI field emission scanning electron microscope fitted with energy dispersive spectrometer (EDS).

3.5.2 Physical and Mechanical Property Study

Density of the sintered products has been measured by Archimedes' principle after weighing them in air and water separately using an electronic balance with a precision of 0.1 mg. The consolidated samples were subjected to micro hardness test with 50 g load and 15 second dwell time with Vicker’s indenter in a LECO (LN 248AT) micro hardness tester. Compressive tests of the sintered samples were performed using a universal testing machine (Instron SATEC-600 kN & 1000 kN). The test was carried out in open air at room temperature with a cross head velocity of 0.2 mm/min. The fractography of the specimens were also studied by SEM. Wear characteristics of the sintered products were studied by a ball on plate type wear tester (DUCOM) fitted with a Rockwell shape diamond indenter at 20 N and 40 N force for 10 minutes with a velocity of 20 rpm. The specimen was held stationary and the disc was rotated while a normal force was applied through a lever mechanism as shown in Figure 3.6. Worn out samples were seen under SEM to study the wear mechanism.

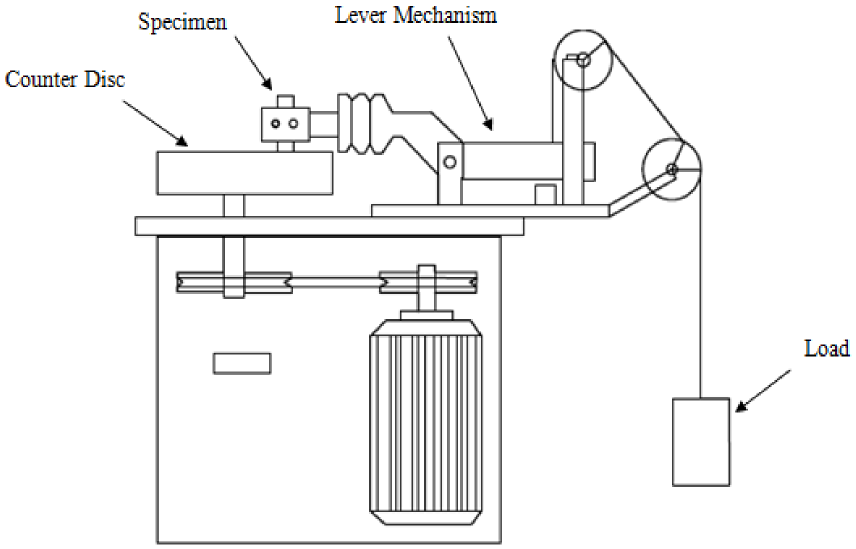

Figure 3.6: Schematic diagram of ball on plate apparatus

3.5.3 Corrosion Study

Sintered samples were metallographically polished with emery papers of different grit size and alumina oxide dispersed fluid media. The mirror polished surfaces of the specimens were subjected to potentio-dynamic polarization test in a 3 mole NaCl solution to study the mechanism and rate of corrosion. A PS6 Meinsberger Potentiostat/Galvanostat connected to a standard three electrode cell comprising the sample as the working electrode (WE), a saturated calomel reference electrode (RE) and a platinum counter electrode (CE) was used for corrosion study. The schematic diagram of corrosion test setup was shown in Figure 3.7. The compositional and morphological study of corrode samples was done using a JEOL-JSM-6480 LV type scanning electron microscope/energy-dispersive spectroscope.

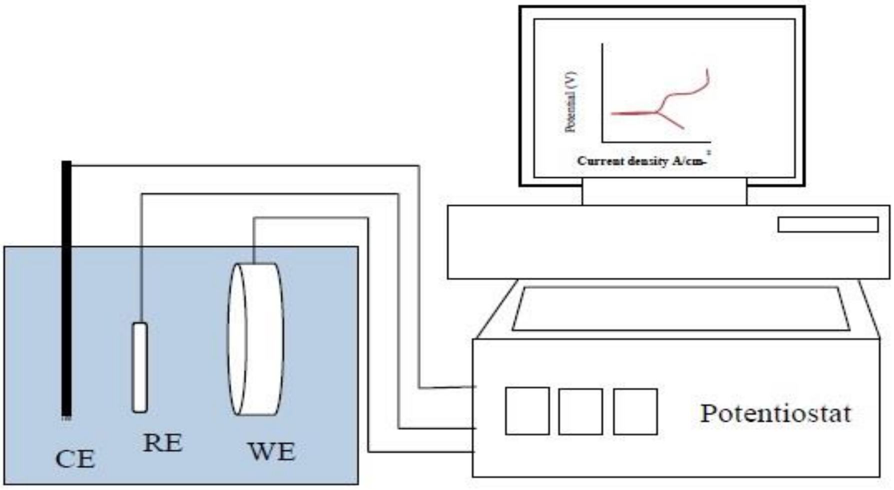

Figure 3.7: Schematic diagram of corrosion test setup

3.5.4 Isothermal and Non-Isothermal Oxidation Study

The alloy specimens prior to Isothermal and non-isothermal oxidation study were rinsed and cleaned with acetone. The isothermal oxidation test was carried out in a tube furnace with provision of flow of excess air. The temperature range of the tests was from 800 ^{o}C to 1100 ^{o}C for 50 hours. During oxidation, the weight gains of specimens were measured after every per each 5 hours till 50 hours. After oxidation, oxidized specimens were analyzed by XRD. Surface morphology of oxidizes specimens were also observed by scanning electron microscope (SEM).

During the oxidation of different metals, various empirical rate laws can be used.

Linear law: $w = K_L t$ (3.1)

Where, w is weight gain per unit area (or) oxide thickness, K_L-rate constant and t-time. Equation (3.1) is typical for metals with porous or cracked oxide films (transport of reactant ions occurs at faster rates than the chemical reaction), e.g., K, Ta.

Parabolic law: $w^2 = K_p t + C$ (3.2)

Equation (3.2) is typical for metals with thick coherent oxides, e.g. Cu, Fe. In this case, the oxidation rate is determined by the diffusion of oxygen through the oxide scale.

Logarithmic rate: $w = K_e \log (Ct + A)$ (3.3)

Equation (3.3) is typical for oxidation at elevated temperature, e.g., Fe, Cu, Al; fast oxidation at the start, the rate decreases to a very low value.

Some of the metals are catastrophic at high temperatures causing rapid exothermal reactions and the oxides are volatile, e.g. Mo, W, V.

Non-isothermal oxidation studies were carried out by TG/DSC (Netzsch, Germany, Model 449 C) from room temperature to 1273 K at a heating rate of 4 K, 6 K and 8 K and 10 K/min. Post oxidation study was also carried out similarly as of isothermal tests. The fraction of the sample oxidized (α) was determined from the change of mass of the sample:

$$\alpha = w/W \tag{3.4}$$

where, w is the increase in mass of the sample and W is the total amount of oxygen required for the complete conversion of alloy to its stable oxides.

Chapter 4

Synthesis of Alloy Powders by Mechanical Alloying

4.1 Introduction

Synthesis of alloy powders by mechanical alloying strongly involves in solving the problems of powder contamination and oxide formation. The extent of contamination increases with increasing milling energy and milling time. In this chapter, effect of milling parameters on alloying of powder, milled powder homogenization and fast amorphization are discussed.

4.2 Phase and Microstructural Characterization

The alloys $Zr_{45}Fe_{30}Ni_{20}Mo_5$ (alloy-A), $Zr_{44}Fe_{30}Ni_{20}Mo_5$ $(TiO_2)_1$ (alloy-B_1), $Zr_{44}Fe_{30}Ni_{20}Mo_4(TiO_2)_2$ (alloy-B_2), $Zr_{44}Fe_{30}Ni_{20}Mo_5$ $(Y_2O_3)_1$ (alloy-C_1) and $Zr_{44}Fe_{30}Ni_{20}Mo_4(Y_2O_3)_2$ (alloy-C_2) were processed by a planetary ball mill (FRITCSCH, Pulverisette-5) (Mill-1) for 20 hours and the samples were collected after 0 h, 1 h, 5 h, 10 h, 15 h and 20 h milling. The same alloy powders were milled in a high energy dual drive planetary ball mill (Mill-2) for 10 hours. 0 h, 5 h and 10 h milled powders were collected for characterization. Milling was processed under toluene liquid medium to obtain finer ground products, for faster amorphization and to prevent oxidation. The collected powder samples from both mills were characterized by means of XRD, SEM and Particle size analysis. The final milled powders obtained from both mills (i.e. 20 h and 10 h milled powders) were characterized by TEM and DSC.

4.2.1 XRD Study

Figure 4.1 shows the series of XRD spectra of all the alloy powders subjected to milling of 0 to 20 hours in Mill-1. Figure 4.1(a) shows the XRD pattern of alloy A and indicates that Fe, Ni, and Mo undergo into solid solution in the Zr matrix; it can be observed clearly that with an increase in milling time, peak intensities, except those for Zr peaks, decrease.

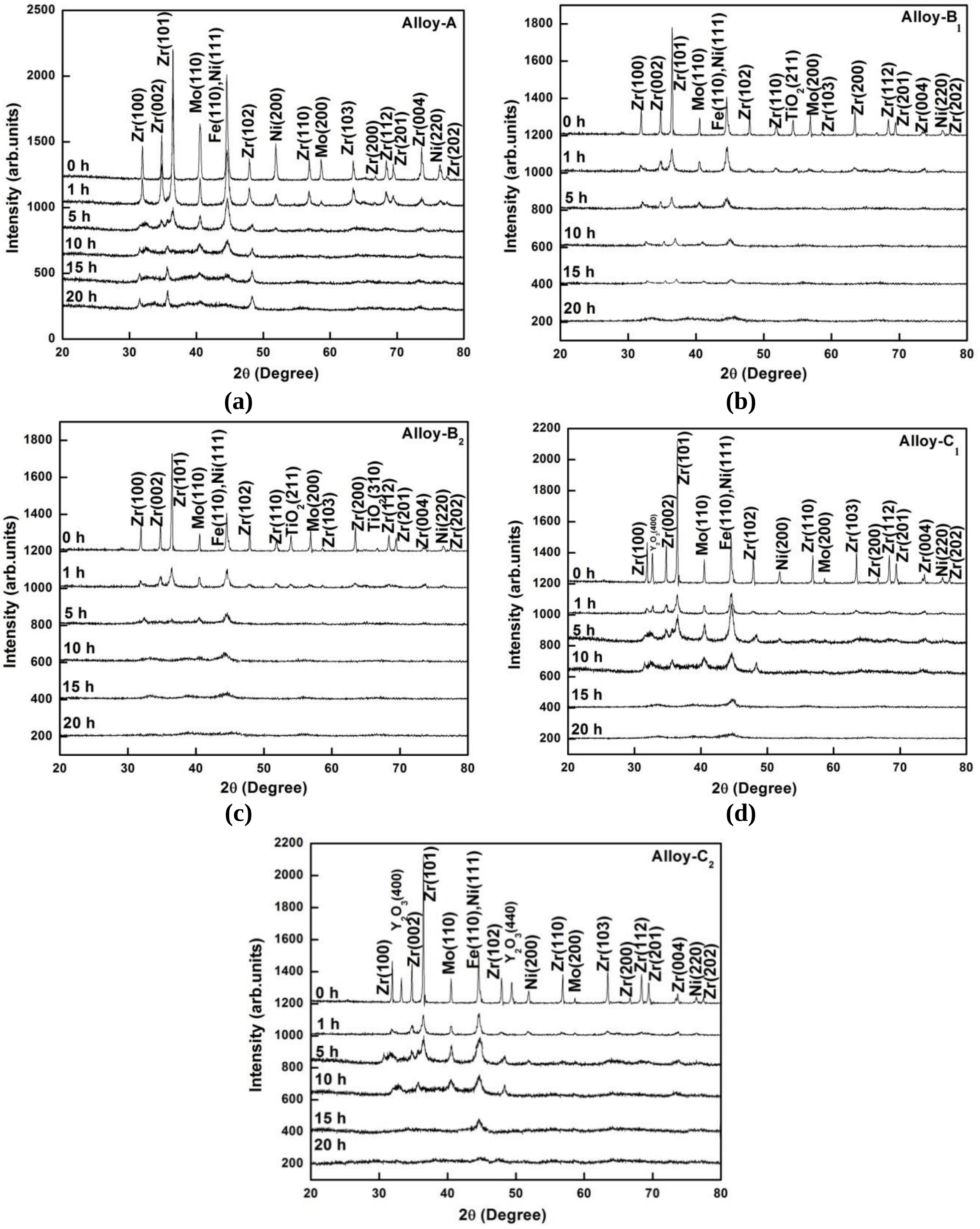

(a) **(b)**

(c) **(d)**

(e)

Figure 4.1: XRD patterns of mechanically alloyed powders by Mill-1 of alloy (a) A, (b) B_1, (c) B_2, (d) C_1 and (e) C_2 at different milling times

Pronounced peak broadening was also observed in 5 to 20 hour milled samples. A similar trend was found in alloys B_1 through C_2 (Figures 4.1(b) through (e)). The increase in full-width at half-maximum (*β*) with increasing milling time suggests that both crystallite size reduction and plastic strain accumulation are occurring. In Figure 4.1(b) and 4.1(c) apart from peaks similar to Figure 4.1(a), TiO_2 peaks were also visible up to 5 hours of milling. Similarly in Figure 4.1(d) and 4.1(e) Y_2O_3 peaks were observed.

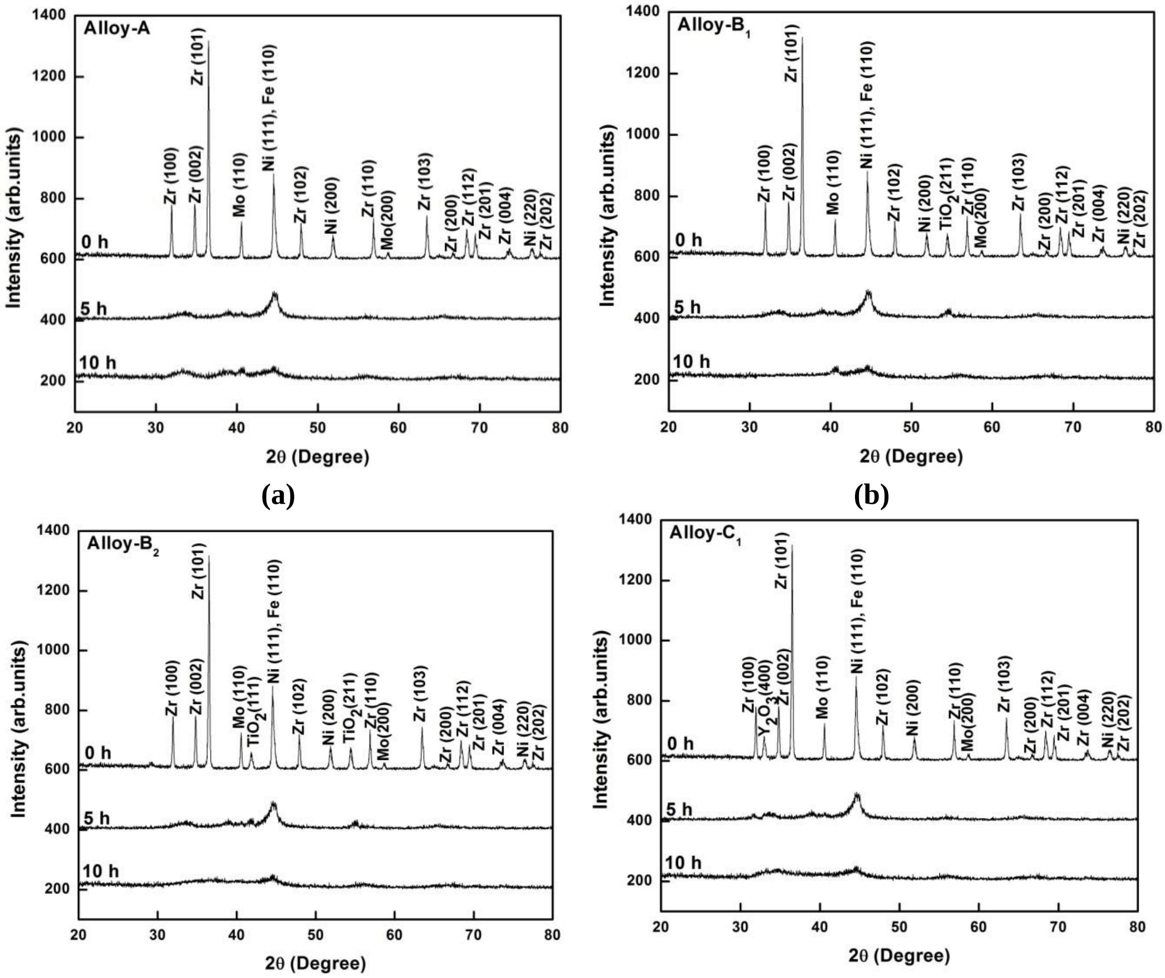

(a) (b)

(c) (d)

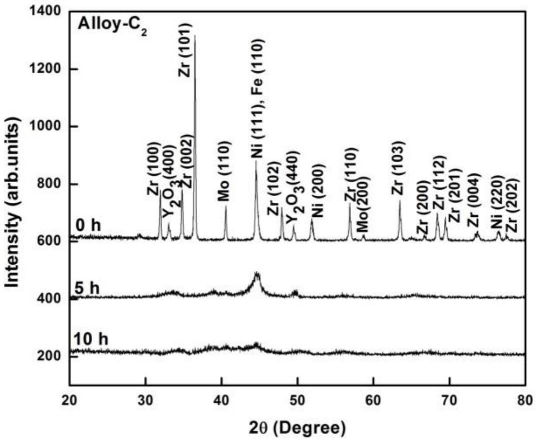

(e)

Figure 4.2: XRD patterns of mechanically alloyed powders produced by Mill-2 of alloy (a) A, (b) B_1, (c) B_2, (d) C_1 and (e) C_2 at different milling times

Figure 4.2 shows the XRD spectra of milled powders of (a) alloy A, (b) alloy B_1, (c) alloy B_2, (d) alloy C_1 and (e) alloy C_2 at different milling times processed in Mill-2. The XRD of alloy powders reveals that the high intensity peaks of the elements (Zr, Fe, Ni, and Mo) present at 0 h of milling were progressively diminishing due to refinement and alloying with increasing milling time. It can be seen that even after 5 h of milling all the elements undergo solid solution formation which also cause broadening of peak. After 10 h of milling, intensity of the peak further decreases indicating complete solid solution and grain refinement. Increased broadening and decreased intensity of the elemental peaks was mainly due to decrease in crystallite size and increasing lattice strain which is quite common with milling operation.

Close scrutiny of β of the most prominent peak in a given XRD profile determines the plastic strain and crystallite size. The crystallite size and lattice strains of the mechanical alloyed powders processed via Mill-1 and Mill-2 measured by Scherrer equations and inter correlated Williamson-Hall (W-H) analysis are shown in Figures 4.3(a) and 4.3(b) respectively.

The average nanocrystalline size and strain induced in powders due to crystal imperfection and distortion was calculated simultaneously calculated by using Williamson-Hall equation[141] as follows:

$$\beta cos\theta = \frac{K\lambda}{D} + 4\varepsilon\ sin\theta \tag{4.1}$$

where, D = crystalline size, K = shape factor (0.94) and λ = wavelength of Cuk$_{\alpha}$ radiation, ε= the root mean square value of microstrain, β = full width at half maximum (FWHM) and θ = the diffraction angle.

It can be observed that the crystallite size gradually decreases and residual strain increases with the increase in milling time. The average crystallite sizes of all the alloys after 20 hours of milling by Mill-1 were calculated and were in the range of 20 to 30 nm. The minimum crystallite size measured in the powder process by Mill-2 was 20 nm after 10 h milling. From the XRD data of alloys B_1,B_2, C_1 and C_2, it was found that for fixed milling hours, the degree of fineness increases with the dispersion. This may be due to the introduction of a higher amount of brittle oxides in the matrix and its subsequent effect during fragmentation of the matrix material.

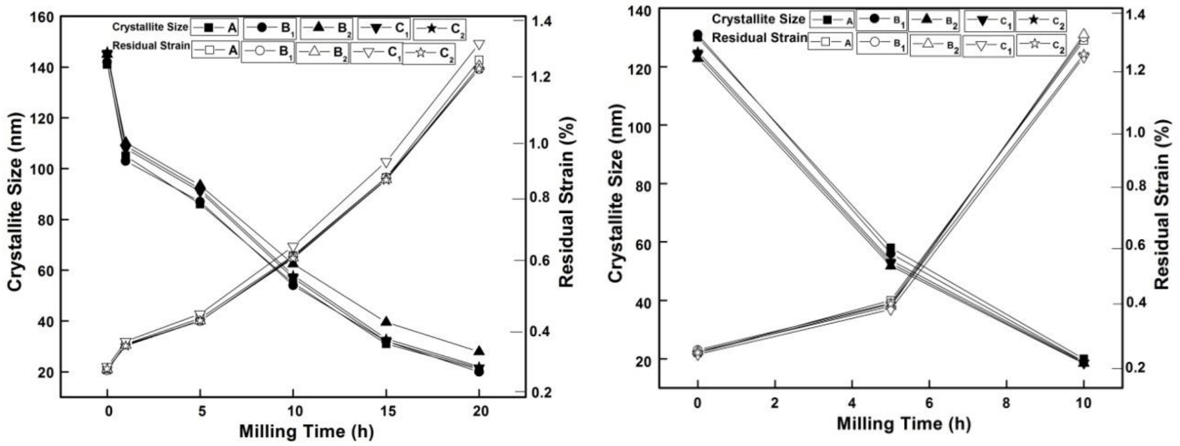

(a) **(b)**

Figure 4.3: Variation of crystallite size and residual strain of the milled powders of alloy A processed (a) by Mill-1 and (b) by Mill-2

4.2.2 SEM Study

Figures 4.4(a) through (f) show scanning electron micrographs of alloy A in each stage of milling by Mill-1(from 0 to 20 hours), revealing that there is refinement of particles from the micron to submicrometer level. Figures 4.4(a) and (b) demonstrate coarser particles and there is a change from 35 to 26 μm due to milling of only 1 hour. As milling time increases (Figures 4.4(c) through (f)), the particle size decreases drastically with a more homogeneous distribution.

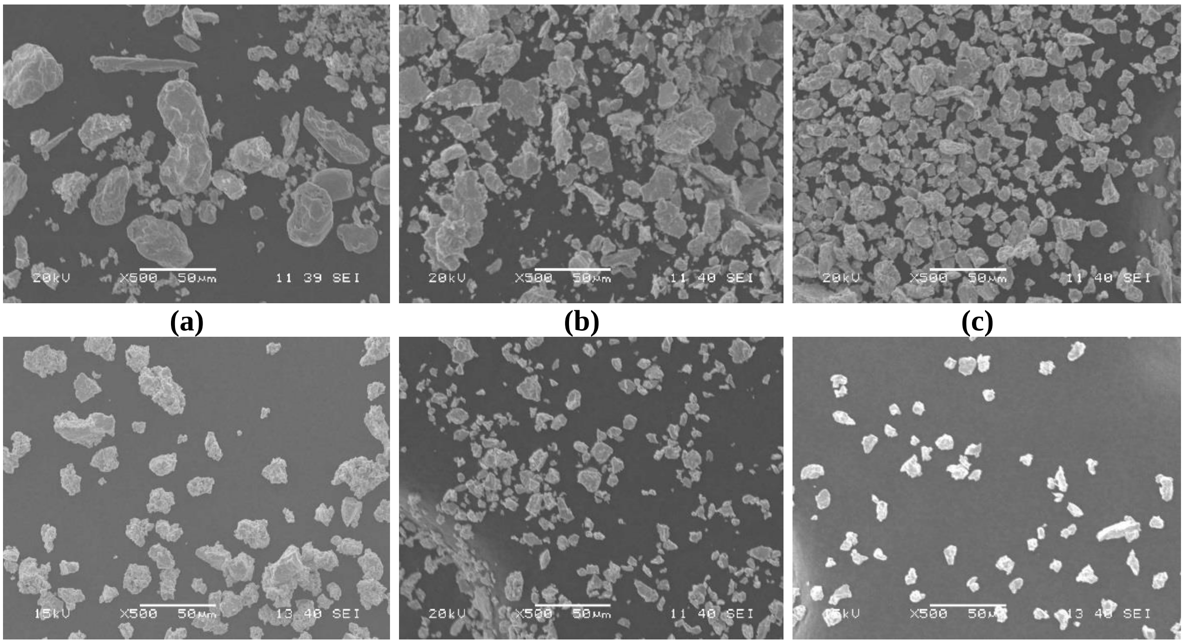

(a) **(b)** **(c)**

(d) **(e)** **(f)**

Figure 4.4: SEM photographs of powder morphology of alloy A after different milling times:(a) 0 h, (b) 1 h, (c) 5 h, (d) 10 h, (e) 15 h and (f) 20 h processed in Mill-1

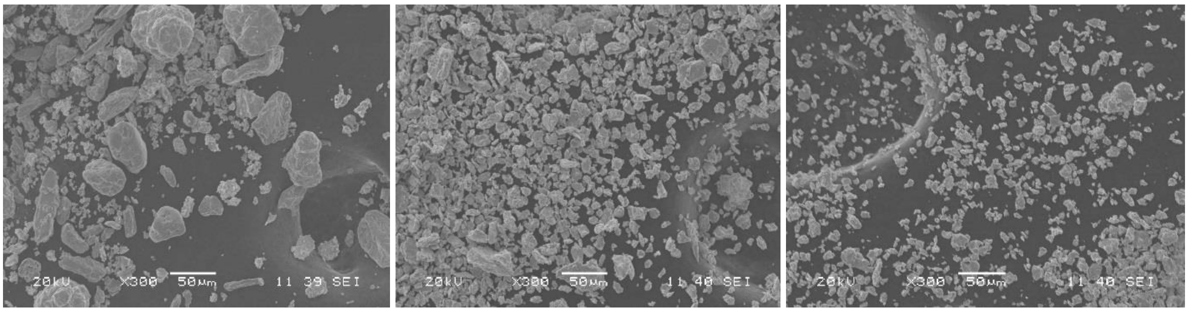

(a) **(b)** **(c)**

Figure 4.5: Powder morphologies of alloy A processed in Mill-2 at milling times: (a) 0 h, (b) 5 h and (c) 10 h observed by SEM

Figure 4.5 shows the SEM micrographs of as-milled powders of alloy A at each stage of milling by Mill-2. It indicates that the initial irregular shaped large particles have been converted to regular uniform finer shaped particles with increase in milling time. The apparent powder particle size was reduced from 50 µm to 18 µm and 11 µm, respectively, with increase in milling time from 0 h to 5 h and 10 hrs. The SEM images of Figures 4.4 and 4.5 indicate that the particles did not get agglomerated due to the presence of toluene during the milling

4.2.3 Particle Size Analysis

Figures 4.6(a) show particle size distribution of alloy A at different milling times (0 to 20 hours) by Mill-1 and the particle size distribution and average particle size measured by particle size analyzer of powder obtained by Mill-2 after milling time of 0 h, 5 h and 10 h are shown in Figure4.6(b).

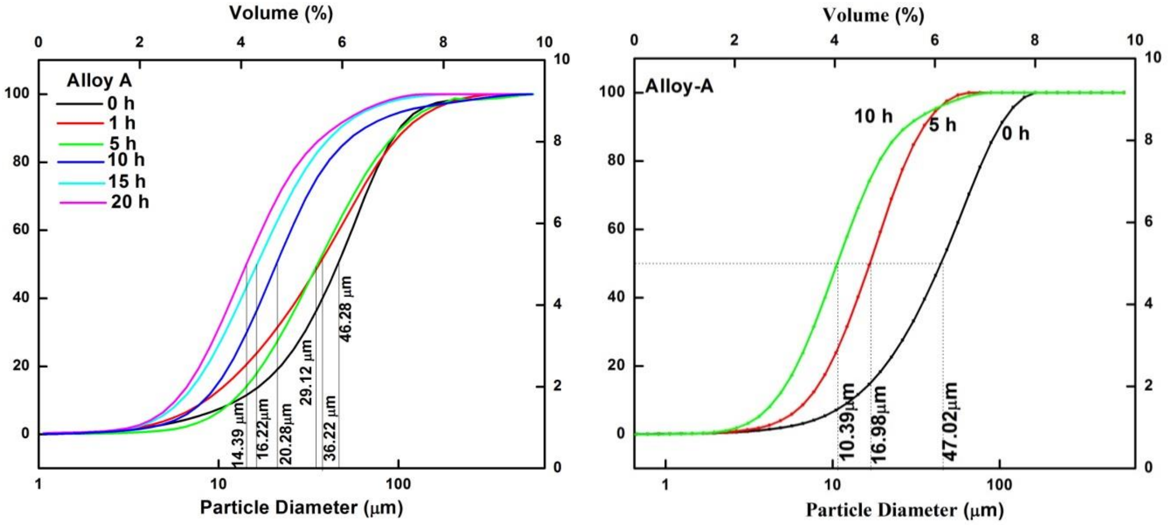

(a) **(b)**

Figure 4.6: Particle size distribution of alloy A at different milling times: Mechanically alloyed powder by (a) by Mill-1 and (b) by Mill-2

The comparative values of average particle size measured from SEM and Particle size analyzer is summarized in Table 4.1. Identical trend was observed in both the measurements of SEM and Particle size analyzer for the powders collected from Mill-1 and Mill-2.

Table 4.1: Average particle size of the milled powders by Mill-1 and Mill-2 of alloy A at different milling time observed by SEM and Particle size analyzer

Milling time (h)	Mill-1		Mill-2	
	Particle Size (µm)		Particle Size (µm)	
	SEM	Particle size analyzer	SEM	Particle size analyzer
0	35	46	49	47
1	26	36	-	-
5	21	29	18	16
10	19	20	11	10
15	18	16	-	-
20	13	14	-	-

The particle size, measured by the particle size analyzer was in close approximation with the particle size observed under SEM. After 20 h of milling the average particle size observed from both SEM and particle size analysis was ~14 μm from Mill-1 and ~10 μm from Mill-2 after 10 h of milling. The particle size reduction was sharp in case of Mill-2 as compared with the powder produced by Mill-1. This is due to higher milling energy associated with the dual drive planetary ball mill.

4.2.4 Transmission Electron Microscopy Study

Transmission electron microscopy (TEM) investigations were performed for further clarification of thephase evolution of the 20 hour and 10 hour milled powder of alloy A by Mill-1 and Mill-2 respectively, and the corresponding TEM figure is represented in Figure 4.7(I) and 4.7(II). The bright field TEM image of Figure 4.7(I) shows that the alloy consists of fine crystallites with an average size of 10 nm. The corresponding selected area diffraction (SAD) pattern of Figure 4.7(I) consists of well-defined continuous rings representingthe presence of finely grained polycrystallites. The SAD pattern can be indexed as (100), (002), and (102) planesof Zr-rich solution. Corresponding inter planar spacing (*d*) values were foundto be 0.28, 0.25 and 0.18 nm. TEM bright field image in Figure 4.7(II) reveals that the average crystallite size of the 10 h milled powder was within 10-15 nm. SAD pattern of the same powder shown in Figure 4.7(II) reveals nano crystalline structure.

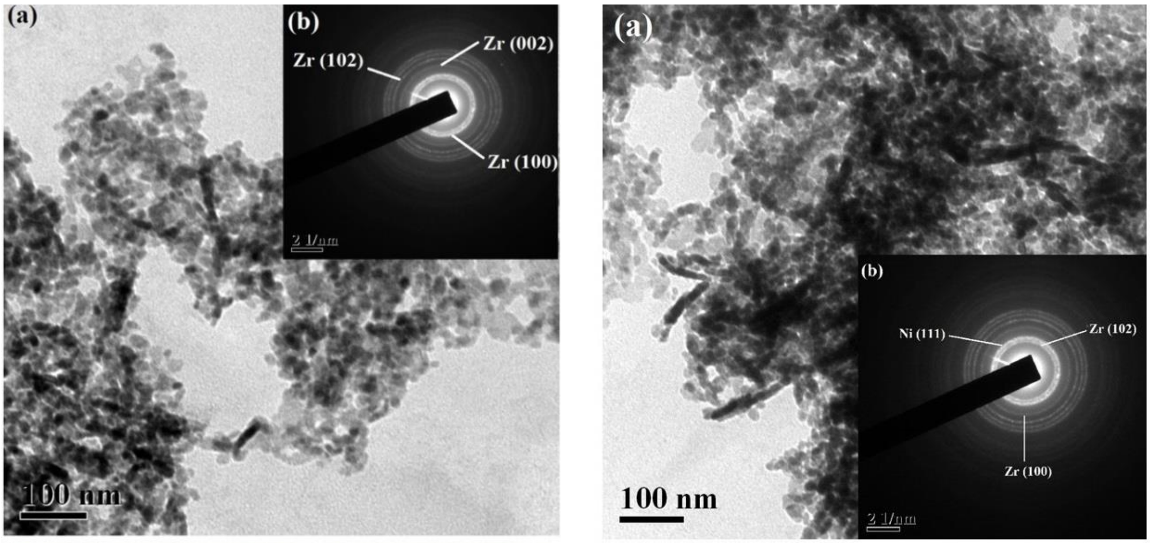

(I) **(II)**

Figure 4.7: (a) Bright field image and corresponding (b) SAD pattern TEM image of (I) 20 h milled powder by Mill-1 and (II)10 h milled powder by Mill-2of alloy A

After careful analysis of the *d* spacing of the rings, presence of Zr (100), Zr (102) and Ni (111) planes were confirmed. Similar observations were also made by XRD study and the crystallite sizes observed from both studies were in close approximation (Figures 4.3(a) and (b)).

4.3 Recrystallization Behaviour

4.3.1 Differential Scanning Calorimetry Study

Differential scanning calorimetry (DSC) analysis of milled powder of alloy A was carried out with various heating rates (4, 6, 8, and 10 K/min) up to 1473 K (1200 °C) in argon atmosphere. Figure 4.8(a) shows the DSC of the 20 hour milled powder by Mill-1 and Figure 4.8(b) shows that for 10 hour milled powder obtained by Mill-2 of alloy A for all four heating rates. In case of alloy powder produced by Mill-1, the recrystallization peak shifted toward higher temperature with an increase in heating rate and the observation of a single exothermic peak indicates that the crystallization process changes from a multistep crystallization process to a single exothermic peak with the presence of transition metal Mo [142]. From Figure 4.8(b) it can be observed that two steps (two exothermic peaks) recrystallization process was involved at lower heating rates of 4 and 6 K/min and these heating rates are not enough to remove strain induced during milling. At higher heating rates of 8 to 10 K/min the two step crystallization changes to single step.

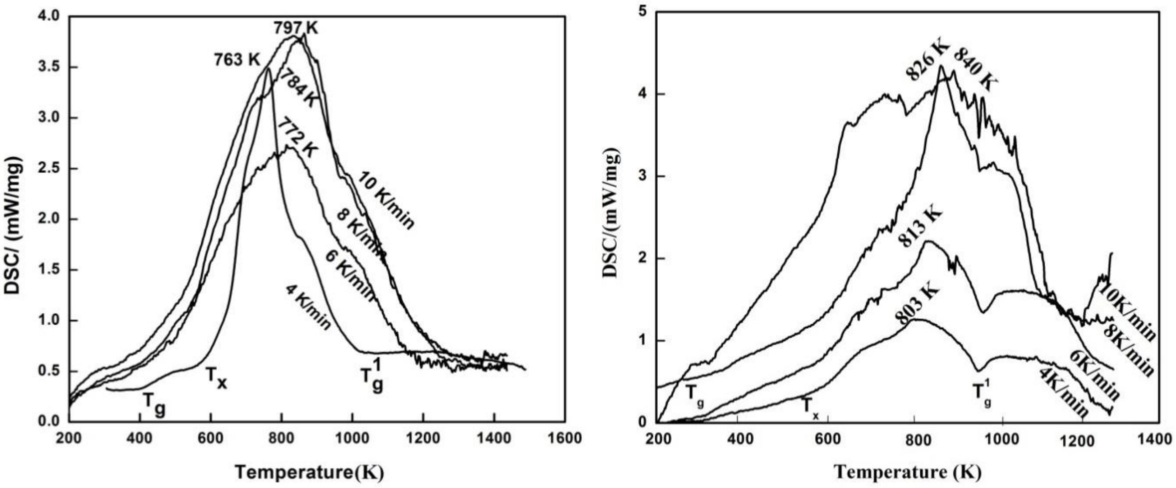

(a) **(b)**

Figure 4.8: DSC plot of (a) 20 h alloyed powder by Mill-1 and (b) 10 h alloyed powder by Mill-2 of alloy A at different heating rates of 4, 6, 8, and 10 K/min

The crystallization temperature (T_x), peak temperature (T_p), onset glass transition temperatures (T_g), glass transition end point (T_g^{l}), and supercooled liquid region (ΔT_x) observed in Figure 4.8 are summarized in Table 4.2. The activation energy of recrystallization can be calculated using Kissinger's equation as follows:

$$ln\ (\Phi/T_P^2) = -(E/RT_P) + C \qquad (4.2)$$

where, T_p is the peak temperature, Φ is the heating rate, R is the gas constant, C is the constant and E is the activation energy of recrystallization. Figure 4.9 shows the plots of $ln\ (\Phi/T_p^2)$ vs. 1000 X ($1/T_p$) based on the data shown in Table 4.2.

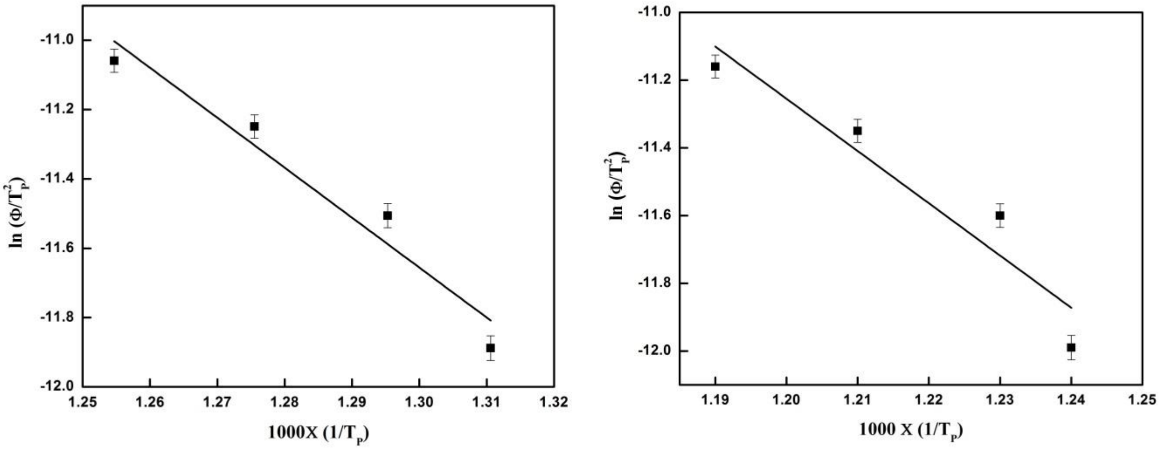

(a) **(b)**

Figure 4.9: Kissinger's plot of (a) 20 h and (b) 10 h milled powder of alloy A at different heating rates of 4, 6, 8, and 10 K/min

Table4.2: Thermal transitions obtained from DSC

Heating Rate Φ (K/min)	Onset Temperature (T_g) K	Crystallization Temperature (T_x) K	Peak Temperature (T_p) K	End Point (T_g^{l}) K	Supercooled Liquid Region (ΔT_x) K	$ln(\Phi/T_p^2)$	1000 X($1/T_p$)
Mill-1							
4	370	510	763	810	140	-11.88	1.31
6	489	612	772	830	123	-11.50	1.29
8	367	521	784	819	154	-11.24	1.27
10	378	520	797	834	142	-11.05	1.25
Mill-2							
4	300	510	803	973	210	-11.99	1.24
6	315	570	813	967	255	-11.60	1.23
8	321	582	826	951	242	-11.35	1.21
10	332	597	840	942	265	-11.16	1.19

The apparent activation energy of recrystallization of the alloy was calculated from the slope of the graph (Figure 4.9). The activation energy of recrystallization of alloy processed by Mill-1was 119.76±2.32 kJ/mol and alloy processed by Mill-2 was 128.20±3.43 kJ/mol. In spite of lower milling time in Mill-2 (10 h) compared to Mill-1 (20 h), the higher activation energy of the Mill-2 powder is due to the higher milling energy associated with the dual drive planetary ball mill (Mill-2).

4.4 Summary

Powders with different alloy compositions ($Zr_{45}Fe_{30}Ni_{20}Mo_5$ (alloy-A), $Zr_{44}Fe_{30}Ni_{20}Mo_5$ $(TiO_2)_1$ (alloy-B_1), $Zr_{44}Fe_{30}Ni_{20}Mo_4$ $(TiO_2)_2$ (alloy-B_2), $Zr_{44}Fe_{30}Ni_{20}Mo_5$ $(Y_2O_3)_1$ (alloy-C_1) and $Zr_{44}Fe_{30}Ni_{20}Mo_4$ $(Y_2O_3)_2$ (alloy-C_2)) were mechanically alloyed by two different high energy ball mills (Mill-1 and Mill-2) and subsequently were characterized by XRD, SEM, TEM, particle size analyzer and DSC. The results obtained from the study and comparison of them based on alloy composition, milling equipment and milling parameters are summarized below.

- XRD analysis of the milled powders of different compositions obtained from different stages (0, 1, 5, 10, 15, 20 h for Mill-1 and 0, 5, 10 h for Mill-2) of milling from both the mills shows that with increasing milling time elemental powders (Fe, Ni and Mo) slowly goes into solid solution and at final stage the alloys show single-phase Zr rich extended solid solution. With increasing milling time it was also observed that refinement of crystallite size and induced strain make the XRD peaks broader.

- Mechanical alloying is a promising route to synthesize nano crystalline powders. In the present study also it was observed that high energy ball milling of the elemental powder mix produced a nano-crystalline powder. XRD results and their subsequent analysis shows that Mill-2 produced nano-crystalline powders of 20 nm at 10 h of milling. But, in case of Mill-1 even after 20 h of milling the crystallite size of obtained nano-crystalline powder was 30 nm.

- The SEM and Particle size analysis studies showed gradual refinement in particle size with increasing milling time. After 20 h of milling in Mill-1, the average particle size observed from SEM and particle size analyzer was 13 and 14 μm respectively. And powders obtained from Mill-2 at 10 h shows 10 μm particle size by SEM analysis and 11 μm by particle size analyzer.

- TEM analysis of final milled powders obtained from Mill-1(after 20 h of milling) and Mill-2 (after 10 h of milling) reveals 10-15 nm crystallite size.

- The activation energyof the final milled powder of the alloy A was calculated from Kissinger’s plots and the values obtained from powders of Mill-1 and Mill-2 are 119.76±2.32 and 128.20±3.43 kJ/mol respectively.

From the abovementioned discussion it was clear that Mill-2 is more efficient to produce nano-crystalline powders than that of Mill-1.

Chapter 5

Conventional Sintering and Characterization

5.1 Phase and Microstructural Characterization

Final milled powders (20 h) of alloys processed in Mill-1 were compacted at 1 GPa pressure for 5 minutes using a hydraulic pressing unit as mentioned in experimental section. The green compacts were sintered in atmosphere controlled high temperature tube furnace at 1673 K (1400 ^{o}C) in Argon gas for 1 hour. Phases present in the sintered specimen and their distribution were studied by XRD, SEM/EDS and TEM analysis.

5.1.1 XRD Study

Figure 5.1 shows the sintered products' XRD patterns of all the alloys (A, B_1, B_2, C_1 and C_2) sintered at 1400 ^{o}C. When Figure 5.1(a) was compared with the XRD profile of 20 h milled powder, it reveals formation of newer peaks and increase in intensity of existing peaks. This implies formation of newer phases (intermetallics), release of induced strain, recrystallization and growth of the existing phases during sintering. Due to hindrance in recrystallization of the matrix with increased dispersiod, with increasing TiO_2 dispersion the peak broadening was more and intensity was decreased (Figure 5.1(b) and (c)) compared to alloy A. The same trend was observed with 1-2 wt. % Y_2O_3 dispersed alloys (Figure 5.1(d) and 5.1(e)). This increased stress field due to dispersion can enhance the hardness and tensile strength. Moreover, the peak profile exhibits the presence of some intermetallic compounds like Mo_2Zr, $FeZr_2$, NiZr and $Ni_{11}Zr_9$. In those along with the intermetallic compounds, presence of TiO_2 and Y_2O_3 were confirmed in corresponding alloys. These intermetallic compounds are generally good for improving toughness at higher temperature.

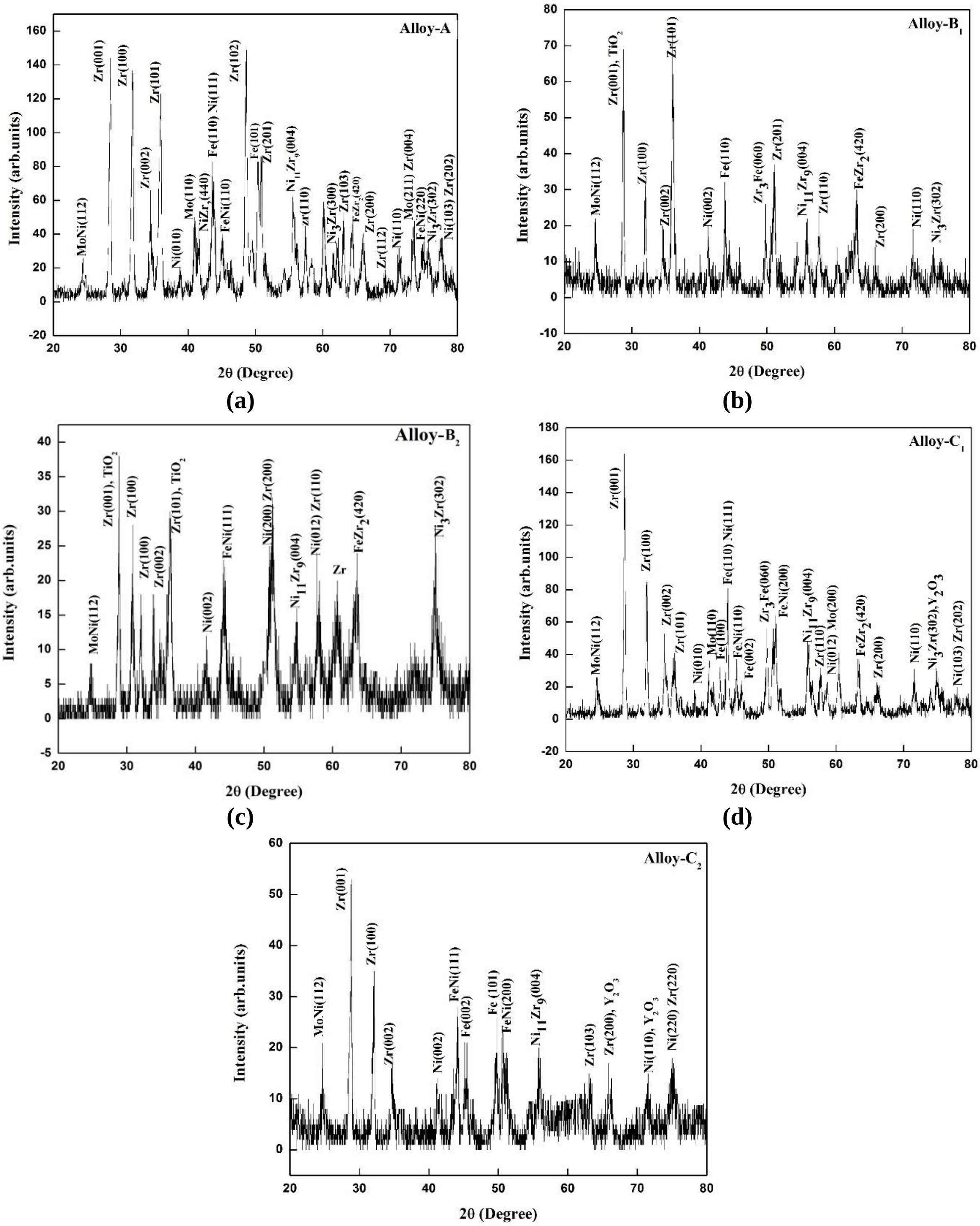

(a) (b) (c) (d) (e)

Figure 5.1: XRD patterns of sintered products of alloy (a) A, (b) B_1, (c) B_2, (d) C_1 and (e) C_2 at 1400 °C

5.1.2 SEM/EDS Study

Figure 5.2 shows the SEM image of the sintered products of (a) alloy A, (b) alloy B_1, (c) alloy B_2, (d) alloy C_1 and (e) alloy C_2. The EDS spectra's of corresponding alloys shown in Figure 5.3(a), 5.3(b) and 5.3(c). Figure 5.2 indicates that the alloys were well sintered but it seems that during conventional sintering substantial grain growth has been taken place due to longer heating period at elevated temperature. Presence of minor amount of porosity is also clear from the figure. The corresponding EDS spectra's shows the presence of all the alloying elements.

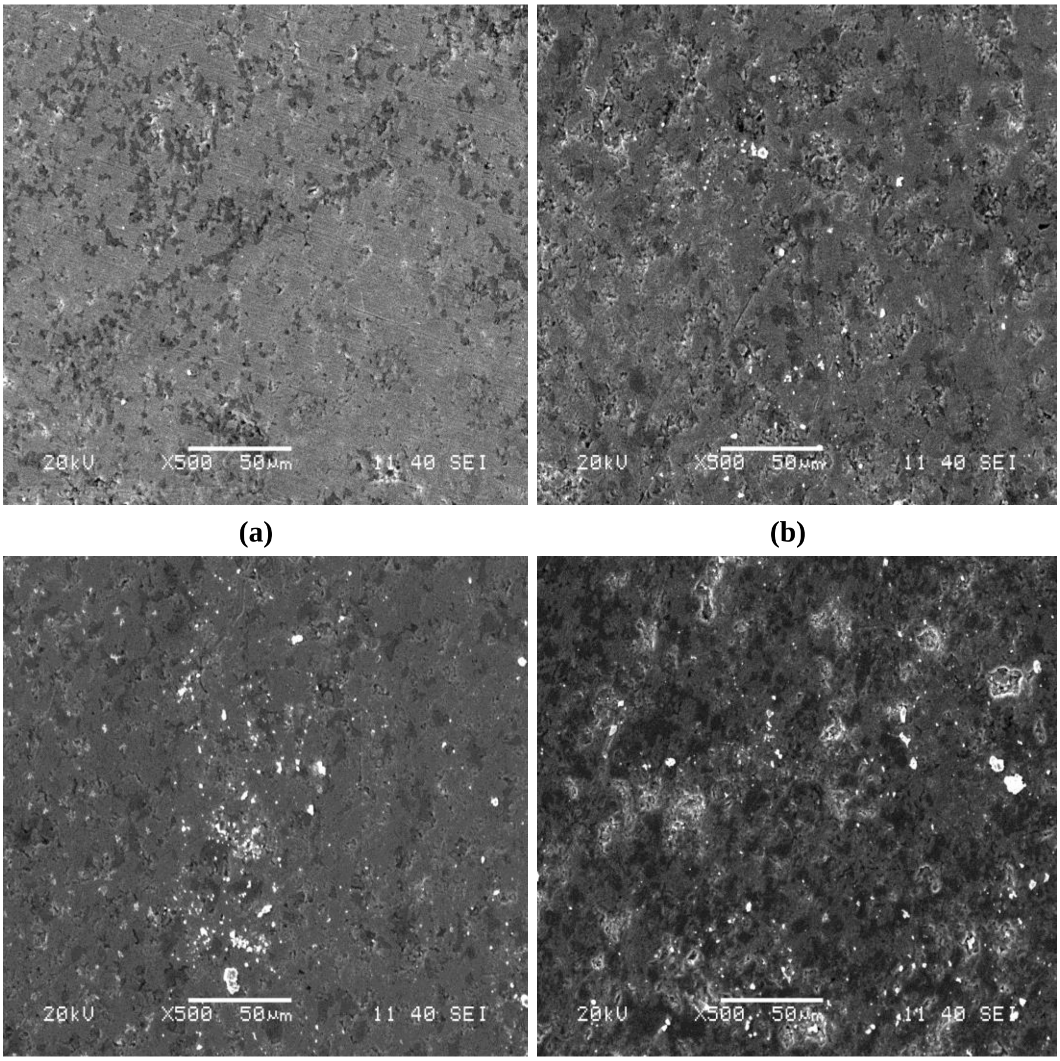

(a) **(b)**

(c) **(d)**

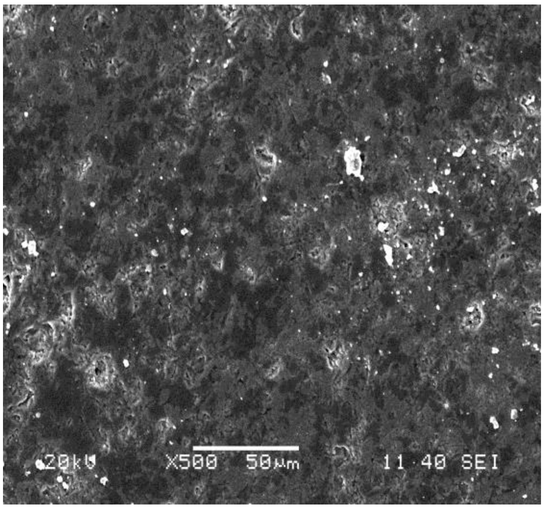

(e)

Figure 5.2: SEM sintered products photographs of alloy (a) A, (b) B_1, (c) B_2, (d) C_1 and (e) C_2 sintered at 1400 °C

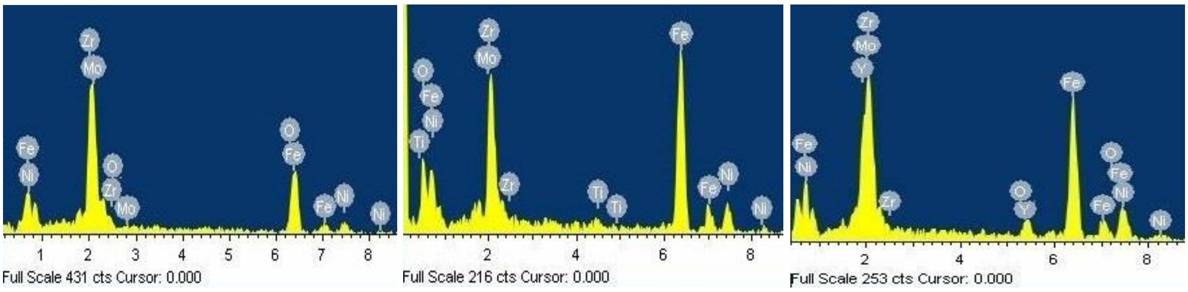

(a) **(b)** **(c)**

Figure 5.3: EDS spectra of alloy (a) A, (b) B_2 and (c) C_2 sintered at 1400 °C

5.1.3 TEM Study

TEM micrographs of sintered products of alloy A, B_2 and C_2 were shown in Figure 5.4. Bright field image of alloy A (Figure 5.4 A(a)) exhibiting the coarse grains compared with alloy B_2 (Figure 5.4 B_2(a)) and alloy C_2 (Figure 5.4 C_2(a)). Corresponding bright field images were shown in Figure 5.4 A(b) for alloy A, Figure 5.4 B_2(b) for alloy B_2 and Figure 5.4 C_2(b) for alloy C_2. The spotted ring patters of alloy A (Figure 5.4 A(b)) represents the presence of coarse grains with multiple crystal phases and these phases were indexed as (300) plane of Ni_3Zr and (201) plane of Zr by matching the corresponding *d*- values 0.153 nm and 0.106 nm with ICDD database. The ring patters of alloy B_2 (Figure 5.4 B_2(c)) represents the presence of $FeZr_2$ (420), (211) plane of TiO_2 and Zr (200) phases having *d*-values 0.142 nm, 0.166 nm and 0.139 nm respectively. Figure 5.4 C_2(c) represents the ring patters of alloy C_2 and it shows the presence of phases Zr

(103) and Y_2O_3 (763) with corresponding *d*-values 0.146 nm and 0.109 nm. All the phases presented by TEM in alloys A, B_2 and C_2 were also confirmed by XRD (Figure 5.1). From dark field and bright field TEM image analysis, the size range of the intermetallics was found in the range of 20-30 nm.

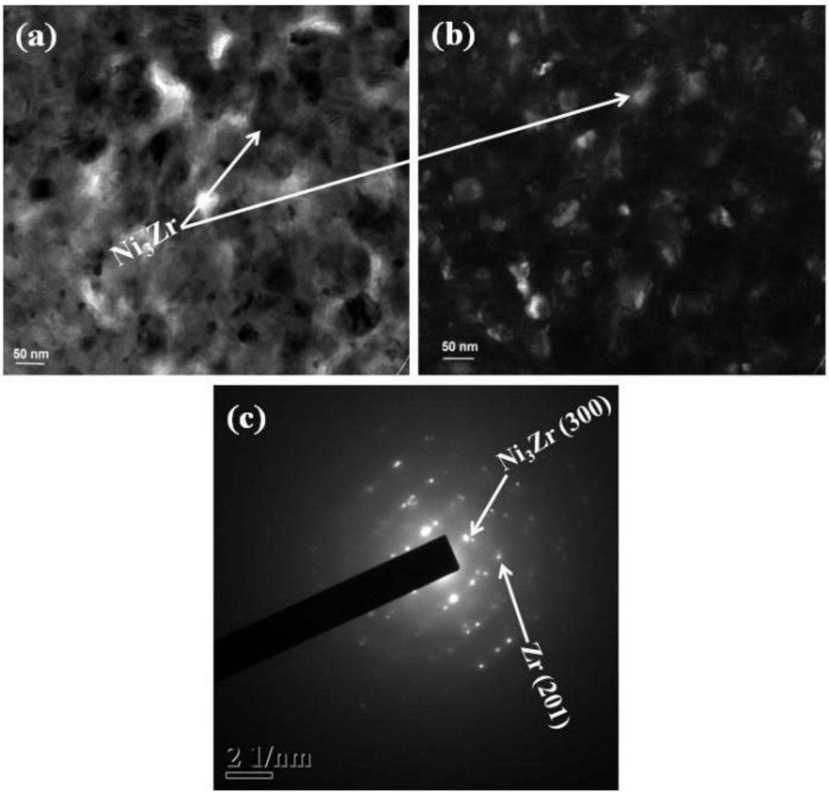

A

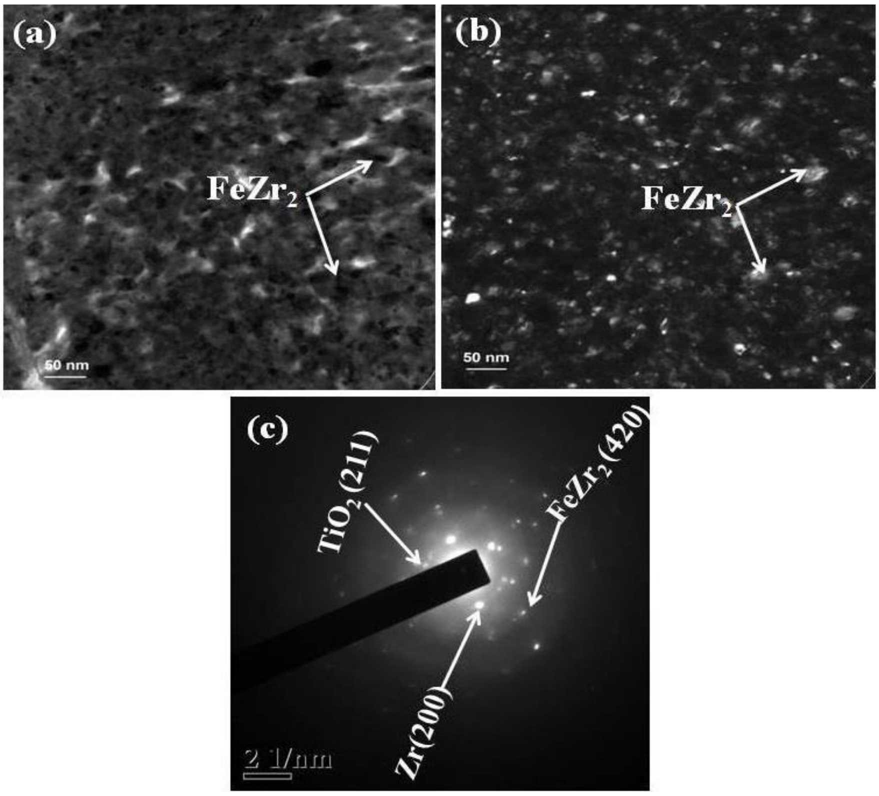

B_2

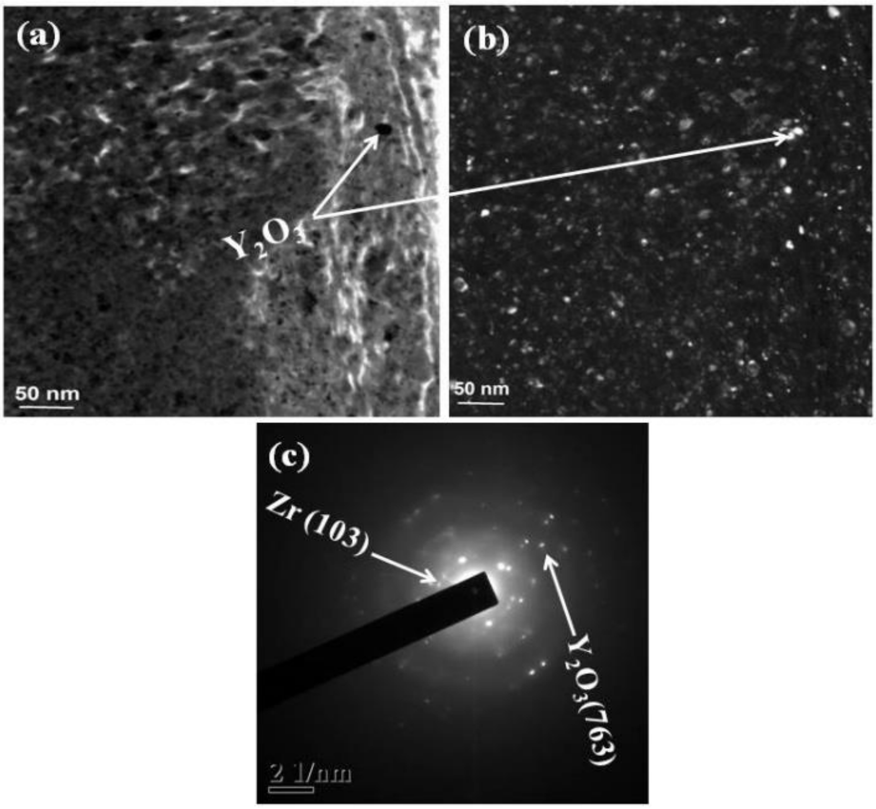

C_2

Figure 5.4: (a) Bright field, (b) dark field TEM images and (c) corresponding SAD patterns of alloy A, B_2 and C_2 sintered at 1400 ^{o}C

5.2 Physical and Mechanical Property Study

5.2.1 Density

Figure 5.5 shows the densities of sintered specimens of alloys A, B_1, B_2, C_1 and C_2 sintered at 1400 ^{o}C. It can be seen that the trends of green and sintered densities are similar with theoretical density. For all the alloys 68-69% green density was achieved and sintered densities were achieved 77-78% to the theoretical density. Table 5.1 shows the summary of density values of Zr-based alloys. The densities of alloy A, B_2, C_2's are in ascending order. This is due to the retardation of solute diffusion during sintering and less stability (thermodynamic) by the presence of nano TiO_2 and Y_2O_3 in case of alloy B_2 and alloy C_2 respectively.

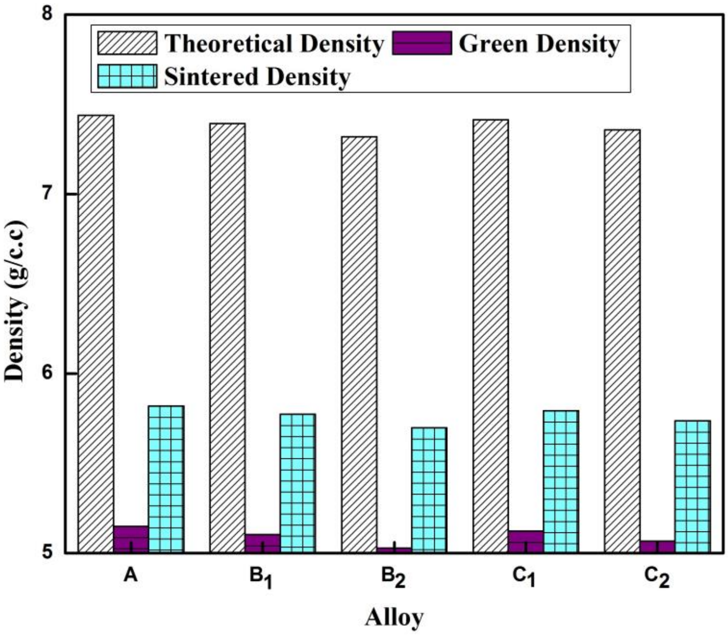

Figure 5.5: Variation of density with alloy composition

Table 5.1: Density values of Zr based alloys

Alloy	Theoretical density (g/cc)	Sintered density	
		(g/cc)	% theoretical density
A	7.439	5.820	78.23
B_1	7.393	5.774	78.10
B_2	7.318	5.699	77.87
C_1	7.413	5.794	78.15
C_2	7.357	5.738	77.99

5.2.2 Hardness

Figure 5.6 shows the variation of hardness by the dispersion of TiO_2 and Y_2O_3. From figure hardness of alloy A, which does not contain any dispersion (nano-TiO_2 / Y_2O_3), exhibits the lowest value. With dispersion of TiO_2 (1-2 wt. %), the hardness values are enhanced to 5.8 to 7.0 GPa and in case of Y_2O_3 dispersion hardness enhanced to 5.8 to 6.3 GPa. This increase in hardness can be attributed to the fine dispersion of TiO_2/ Y_2O_3. Table 5.2 shows the summary of hardness values of Zr-based alloys. The range of increased hardness from alloy from B_1 to B_2 is more than the hardness from alloy C_1 to C_2. This is due to the high modulus of elasticity of TiO_2 [143] as compared with Y_2O_3 [144].

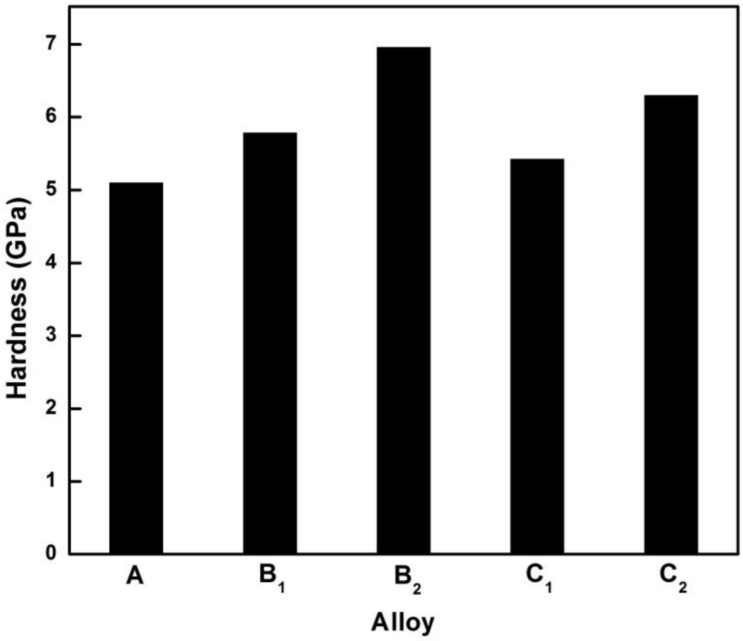

Figure 5.6: Variation of hardness with alloy composition

Table 5.2: Hardness Values of Zr based Alloys

Alloy	Hardness (GPa)
A	5.10
B_1	5.79
B_2	7.00
C_1	5.43
C_2	6.30

5.2.3 Compressive Strength

Figure 5.7 shows the compressive stress strain curves of alloy A, B_1, B_2, C_1 and C_2 sintered at 1400 ^oC. The results indicate that the compressive strength was increased by addition of TiO_2/ Y_2O_3. Moreover with increase of dispersion (TiO_2/Y_2O_3) amount the strength also increases. The compressive strength enhancement was credited by solid solution strength and dispersion (intermetallics and TiO_2/Y_2O_3) strengthening mechanism. All the alloys show marginal compressive elongation before fracture. Alloy A, B_1 and C_1 showed higher values compared to alloy B_2 and C_2 as mentioned in Table 5.3. This can be attributed to large pinning strength with hard nano oxide particles and lower ductility in alloy B_2 and C_2.

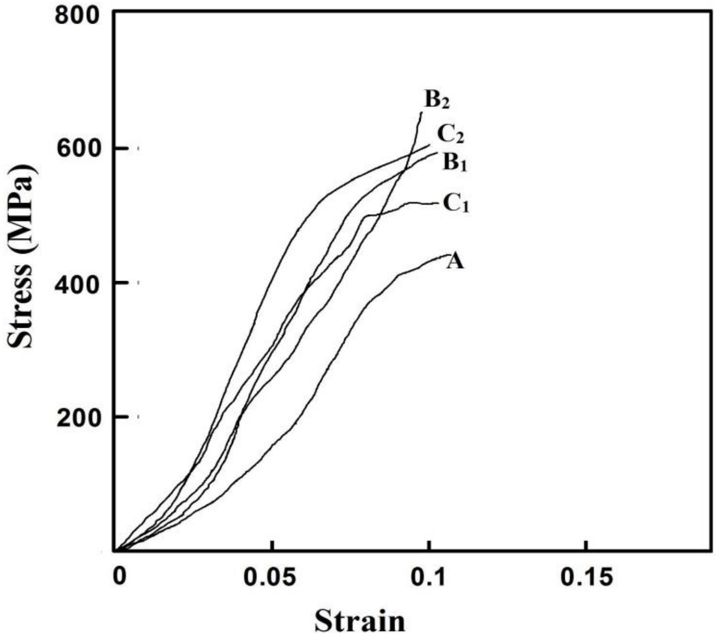

Figure 5.7: Compressive stress strain curves of sintered products of alloy A, B_1, B_2, C_1 and C_2

Table 5.3: Compressive strength and strains of sintered products of alloy A, B_1, B_2, C_1 and C_2

Alloy	Compressive strength (MPa)	Strain
A	428	0.105
B_1	586	0.100
B_2	680	0.096
C_1	510	0.102
C_2	606	0.101

Fracture surfaces of the compressive test specimens are shown in Figure 5.8. The alloy A, B_2 and C_2 (from Figure 5.8(a) to 5.8(c) respectively) indicate that the mode of failure was mixed brittle and ductile nature. It shows evidence of cleavage type failure as well as secondary trace of dimple or micro-void formation.

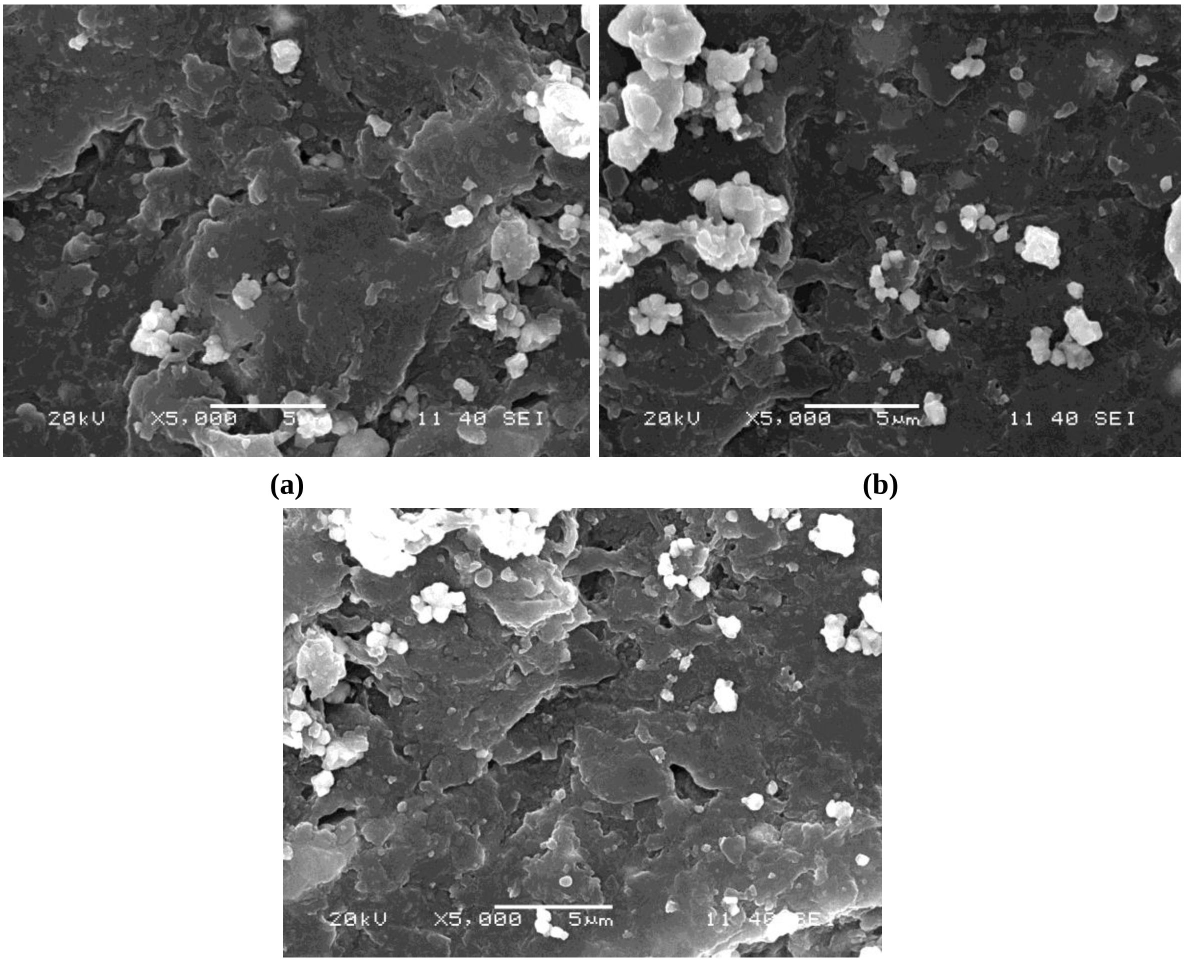

(a) **(b)**

(c)

Figure 5.8: SEM images of fractured surfaces of alloy (a) A, (b) B_2 and (c) C_2

5.2.4 Wear

Figure 5.9 shows the variation of wear loss as depth of penetration vs. sliding distance at a load of 20 N at 20 rpm sliding speed (linear sliding speed 0.004186 m/s) during wear test on a 4 mm diameter track for 10 min duration on the sintered products. The wear depth was decreasing as a function of sliding distance with 1-2 wt. % dispersoids (TiO_2 in the case of alloy B_1 and B_2, Y_2O_3 in case of alloy C_1 and C_2). Alloy A showed the maximum depth of 25 μm and after considerable sliding distance, the depth of wear was linear and smooth in nature. But in case of alloys with dispersion it shows noise in the plot due to the presence of hard TiO_2 and Y_2O_3 particles.

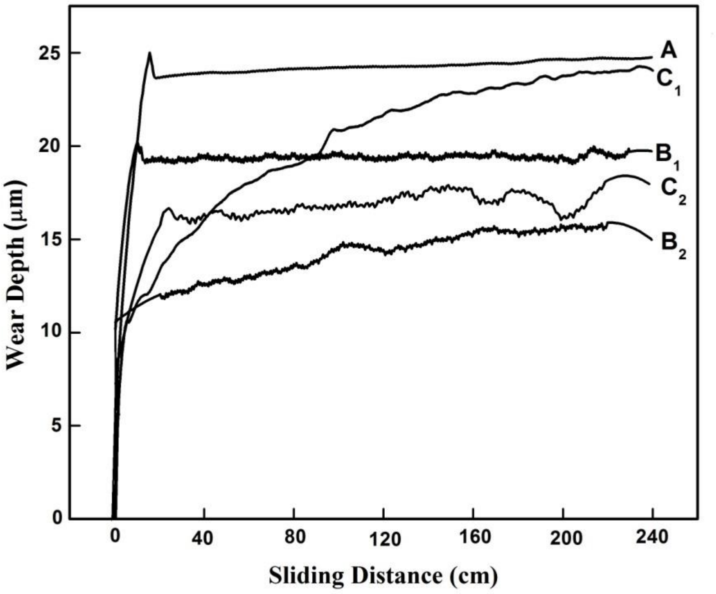

Figure 5.9: Variation of cumulative depth of wear as a function of sliding distance of alloy A, B_1, B_2, C_1 and C_2 sintered at 1400 ^{o}C

The worn out surfaces were examined by SEM are shown in Figure 5.10. The micrographs indicate predominantly abrasive type of wear. In this study the present material having high hardness was tested against diamond indenter, resulting in surface abrasion mainly. Moreover, hard phases (intermetallics) and particles (TiO_2/Y_2O_3) thrown out from the matrix during this abrasion can further increase the wear process by three body motion mechanism. Due to the evenly distribution of all alloying elements, after certain distance of sliding the wear loss shows linear.

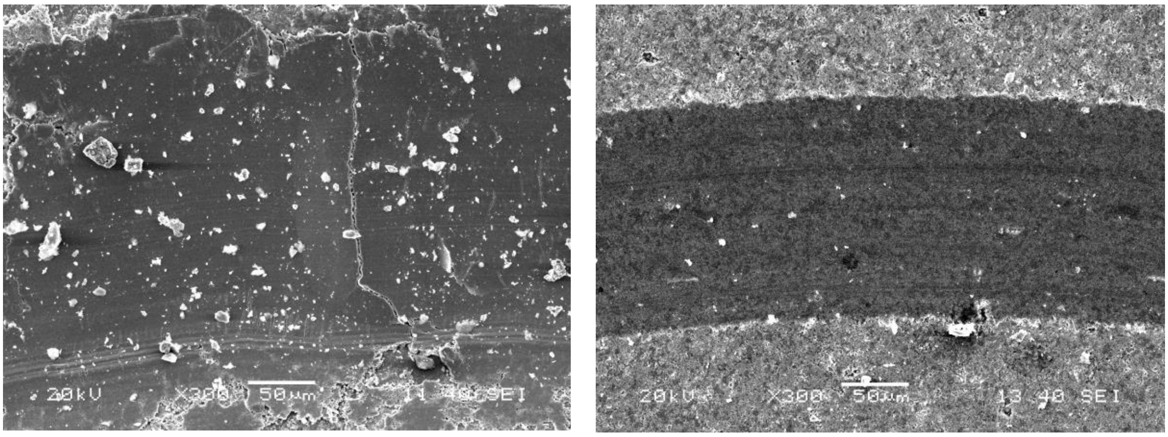

(a) **(b)**

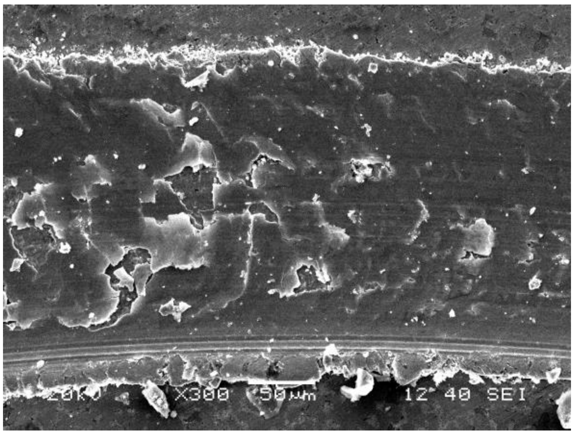

(c)

Figure 5.10: Micrograph of wear track of alloy (a) A, (b) B_2 and (c) C_2 with 20 N load

Wear track of alloy A shows higher width compared to alloy B_2 and C_2. Moreover track width of alloy C_2 is more than alloy B_2. The trend of wear track width is similar with that of wear depth as shown in Figure 5.10. Moreover the edges of the wear track of alloy A and C_2 show marks of adhesive wear mechanism due to spreading of worn out material. But in case of alloy B_2 the track is clean and the edges of the track shows only rubbing /cutting marks, which is indication of abrasive wear.

5.3 Corrosion Study

The corrosion trends of alloy A, B_1, B_2, C_1 and C_2 were observed in 3 mole NaCl solution. The potentio dynamic polarizations are scanned from -1.5 to +0.5 V (vs. Calomel electrode: SCE) with scan rate 0.008002 V/s and step potential 0.00244 V. Figure 5.11 shows potentiodynamic polarization curves of alloy A, B_1, B_2, C_1 and C_2 (respectively from Figure 5.11 (a) to 5.11 (e)). The corrosion rates were calculated in mm/year. The calculated and observed corrosion rates, E_{corr} and I_{corr} are summarized in Table 5.4. It can clearly be observed from Figure 5.11 (a) and Table 5.4 that addition of TiO_2 increases I_{corr} and corrosion rate. Further it was observed that alloy B_2 displays better corrosion property than B_1. Addition of TiO_2 hinders crystallization /growth during sintering resulting finer structure which in turn increases the corrosion attack. But, at the same time TiO_2 helps formation of primary oxide layer of Zr (ZrO_2) as adherent oxide layer formation is the key mechanism of corrosion and oxidation resistance of Zirconium alloys, TiO_2 addition in the present alloy plays two opposing roles.

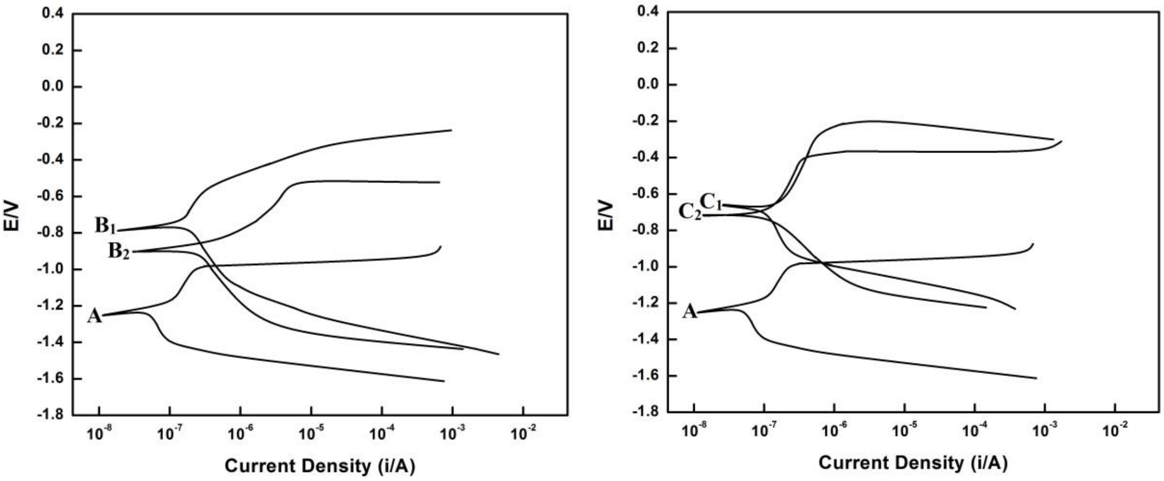

(a) **(b)**

Figure 5.11: Variation of corrosion potential as a function of current density (a) with TiO_2 dispersion and (b) with Y_2O_3 dispersion in 3 Mole NaCl solution

With addition of higher amount of TiO_2 (alloy B_2) the corrosion current and corrosion rate goes down as observed in Table 5.4. This can be attributed towards the positive role of TiO_2, i.e., helping in ZrO_2 formation. Similar trend was also observed in case of Y_2O_3 dispersed alloys (alloy C_1 and C_2). In this case corrosion property improves with addition of any amount of Y_2O_3. This may be due to better oxide stabilizing property of Y_2O_3.

Table 5.4: Potentiodynamic test result of alloy A, B_1, B_2, C_1 and alloy C_2 in 3 Mole NaCl solution

Alloy	E_{corr} (V) observed	E_{corr} (V) calculated	Corrosion rate (mm/year)X10^{-2}	I_{corr} (A/cm^2)X10^{-6}
A	-1.278	-1.284	6.4034	3.6434
B_1	-0.798	-0.802	21.0607	13.6407
B_2	-0.849	-0.833	10.5870	6.9610
C_1	-0.624	-0.610	2.7617	1.8097
C_2	-0.709	-0.701	2.1678	1.3948

5.4 Oxidation Study

5.4.1 Isothermal Oxidation

Figure 5.12 shows weight gain vs. time plot obtained during isothermal oxidation study of alloy A, B_2 and C_2 carried out at 800, 900 and 1000 ^{o}C along with corresponding kinetics study. As the weight due to oxidation shows parabolic nature [145]. Figure 5.13 compares the kinetics of isothermal oxidation in terms of rate constant as a function of temperature for alloys A, B_2 and C_2.

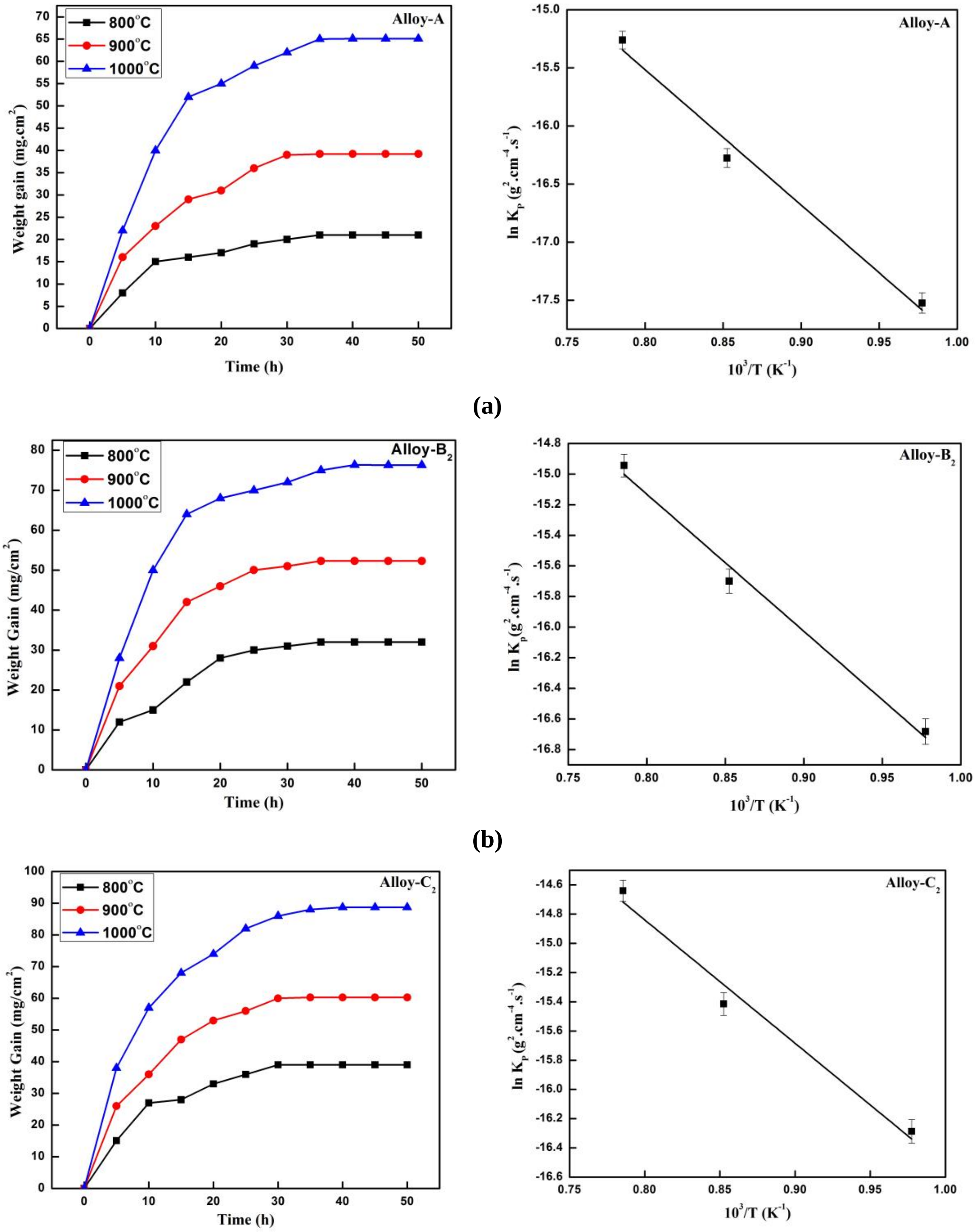

(a)

(b)

(c)

Figure 5.12: Isothermal oxidation kinetics and their corresponding Arrhenius plot for alloy (a) A, (B) B_2 and (c) C_2 at 800, 900 and 1000 °C for 50 hours

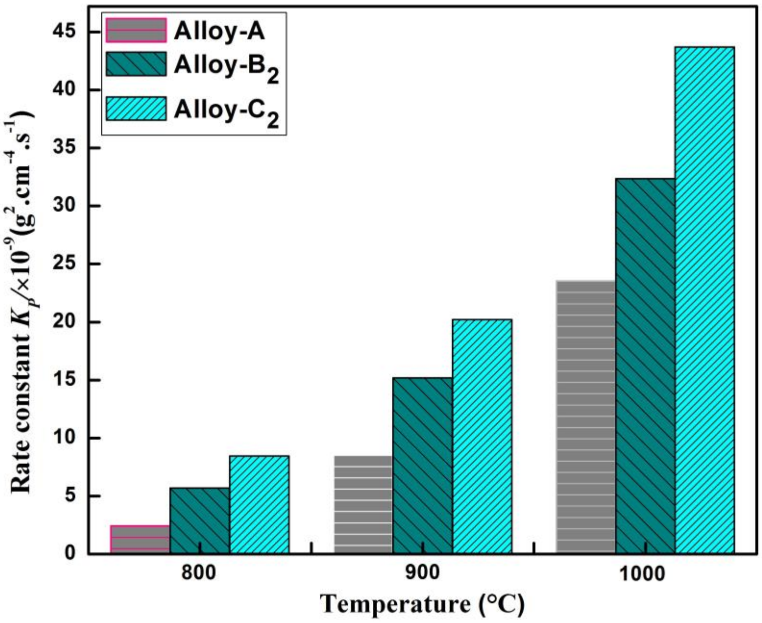

Figure 5.13: Kinetics of isothermal oxidation in terms of rate constant as a function of temperature for alloys A, B_2 and C_2

The activation energies of the alloys were calculated by using Arrhenius relationship. The plots of alloy with the parabolic rate constant ln (K_p) as a function of inverse of temperature T was shown in Figure 5.12. The co-related Arrhenius parameters are summarized in Table 5.5. For isothermal oxidation from the parabolic curves the calculated activation energies are 96.86±1.36 kJ mol^{-1}, 81.84±0.91 kJ mol^{-1} and 80.08±1.19 kJ mol^{-1} for alloy A, B_2 and C_2 respectively. From the obtained values it can be understood that compared to alloy A, oxidation of alloy B_2 and C_2 is faster and C_2 shows marginal faster kinetics over alloy B_2. Similar effect of TiO_2 and Y_2O_3 on oxide layer formation was observed during corrosion study.

Table 5.5: Arrhenius parameters of isothermal oxidation of alloys at different temperatures

Alloy	Temperature (^{o}C)	Rate constant K_P X10^{-9} (g^2.cm^{-4}.s^{-1})	Activation energy (kJ/ mol)
A	800	2.45	96.86±1.36
	900	8.536	
	1000	23.54	
B_2	800	5.688	81.84±0.91
	900	15.19	
	1000	32.34	
C_2	800	8.45	80.08±1.19
	900	20.20	
	1000	43.70	

Figure 5.14 shows the X-ray diffraction patterns of alloy A, B_2 and C_2 after oxidation at 1000 ^{o}C for 50 hours. From the XRD patterns of all three alloys it can be seen that the Zr was oxidized to ZrO_2 and Fe was oxidized to Fe_2O_3, along with other oxides and intermetallics. From the XRD pattern of alloy B_2 (Figure 5.14(b)), formation of ZrO_2 is more active than the alloy A (Figure 5.14(a)) due to the dispersion of TiO_2. Diffusion of these metals may leads to the formation of ZrO_2 or TiO_2 ceramic membrane. In alloy B_2 the continuous and high intensity ZrO_2 peaks confirmed the formation of ZrO_2 oxide layer. In case of Y_2O_3, formation of more ZrO_2 was observed (Figure 5.14(c)) as indicated earlier by kinetics study.

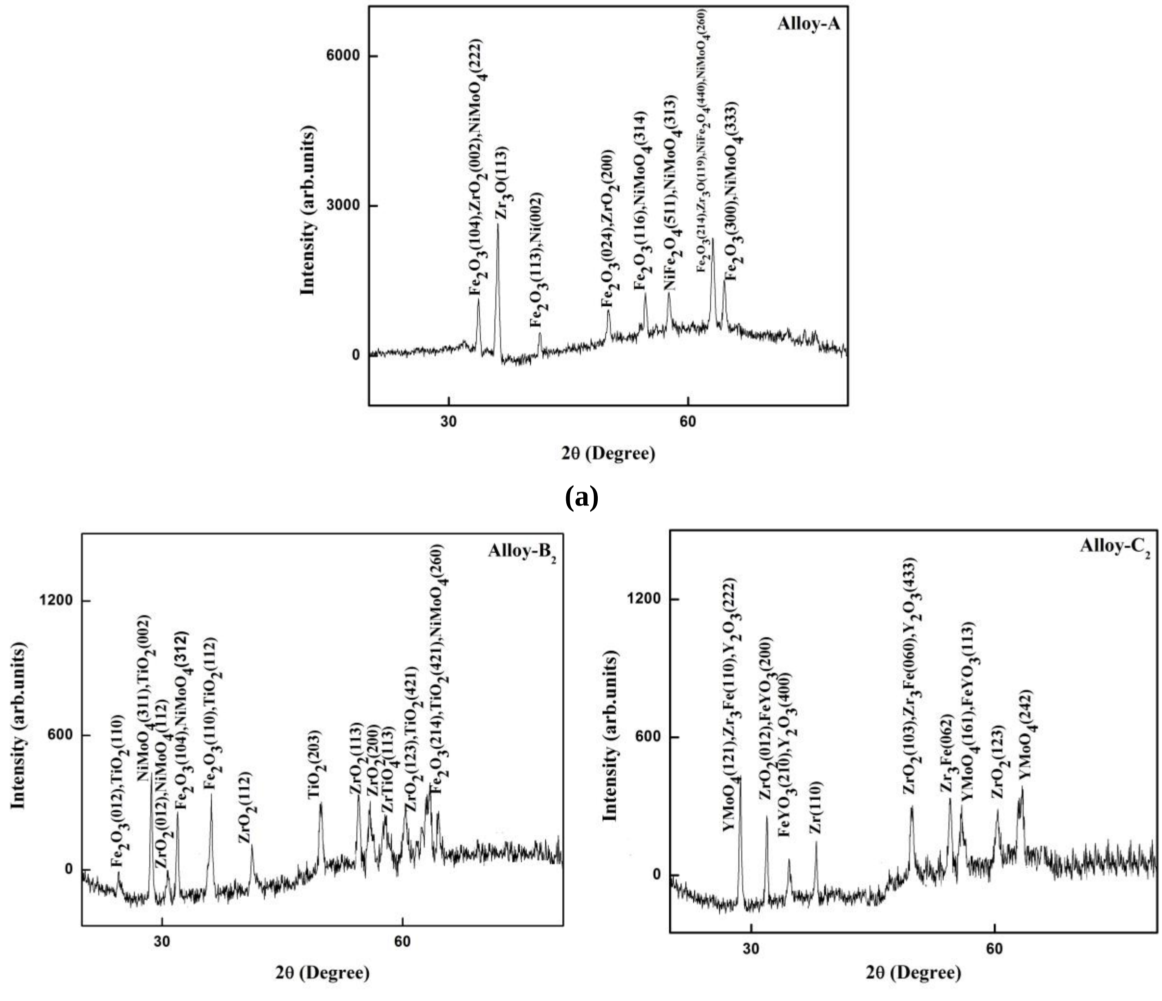

(a)

(b) **(c)**

Figure 5.14: Oxide samples XRD patterns of alloy (a) A, (b) B_2 and (c) C_2 at 1000 ^{o}C for 50 hours

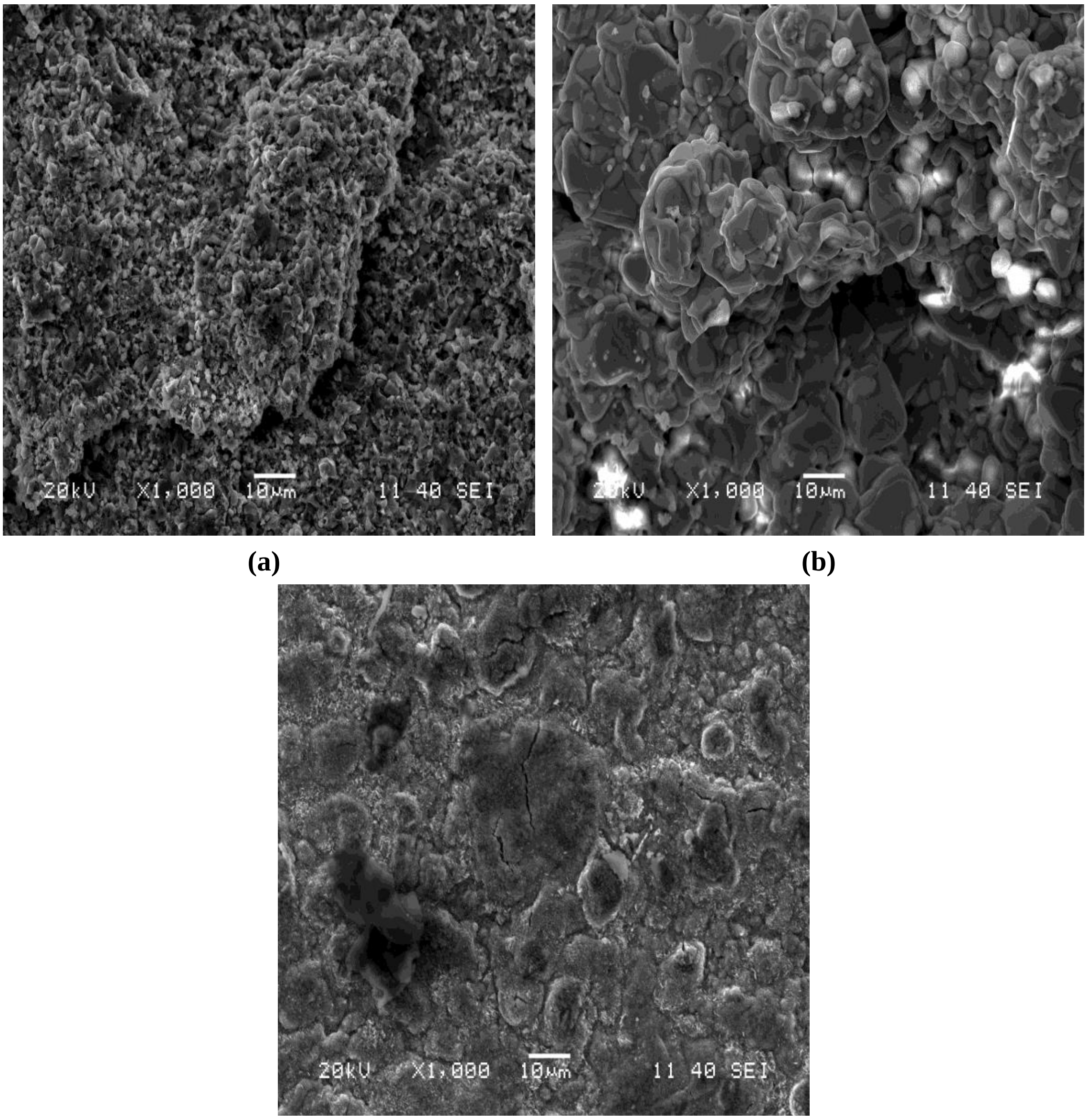

(a) **(b)**

(c)

Figure 5.15: Surface morphologies of alloy (a) A, (b) B_2 and (c) C_2 specimens after oxidized at 1000 °C

Figure 5.15 a-c shows the surface morphologies of the oxide scale formed on alloys A, B_2 and C_2 respectively after isothermal oxidation for 50 h at 1000 °C. It is seen that the oxide layer in case of alloy A (Figure 5.15 (a)) was discontinuous and fine in nature. The oxide layer formed in alloy B_2 (Figure 5.15 (b)) was discontinuous, thicker and relatively larger. The oxide layer formed on the surface of alloy C_2 (Figure 5.15 (c)) was free of pores and dense. Moreover, thickness of the oxide layer seems to be thicker indicating stable oxide growth. Some depleted zones are formed in alloy A and B_2 as indicated in SEM images. This can be linked with the isothermal kinetic curve (1000 °C) of alloy A and B_2 (Figure 5.12) where some data points are not truly in parabolic path.

5.4.2 Non-Isothermal Oxidation

Figure 5.16 compares the extent of oxidation (α) in alloys A, B_2 and C_2 at different heating rates (4, 6, 8 and 10 K/min). In case of 10 K/min (Figure 5.16 (d)), the oxidation of alloy B_2 is negligible until about 380 K and then the alloy shows a rapid oxidation, which slows down beyond about 800 K. The alloy A shows a higher onset temperature for oxidation (620 K) and a better oxidation resistance to start in comparison to the alloys B_2 and C_2. Data obtained from other heating rate show similar trend.

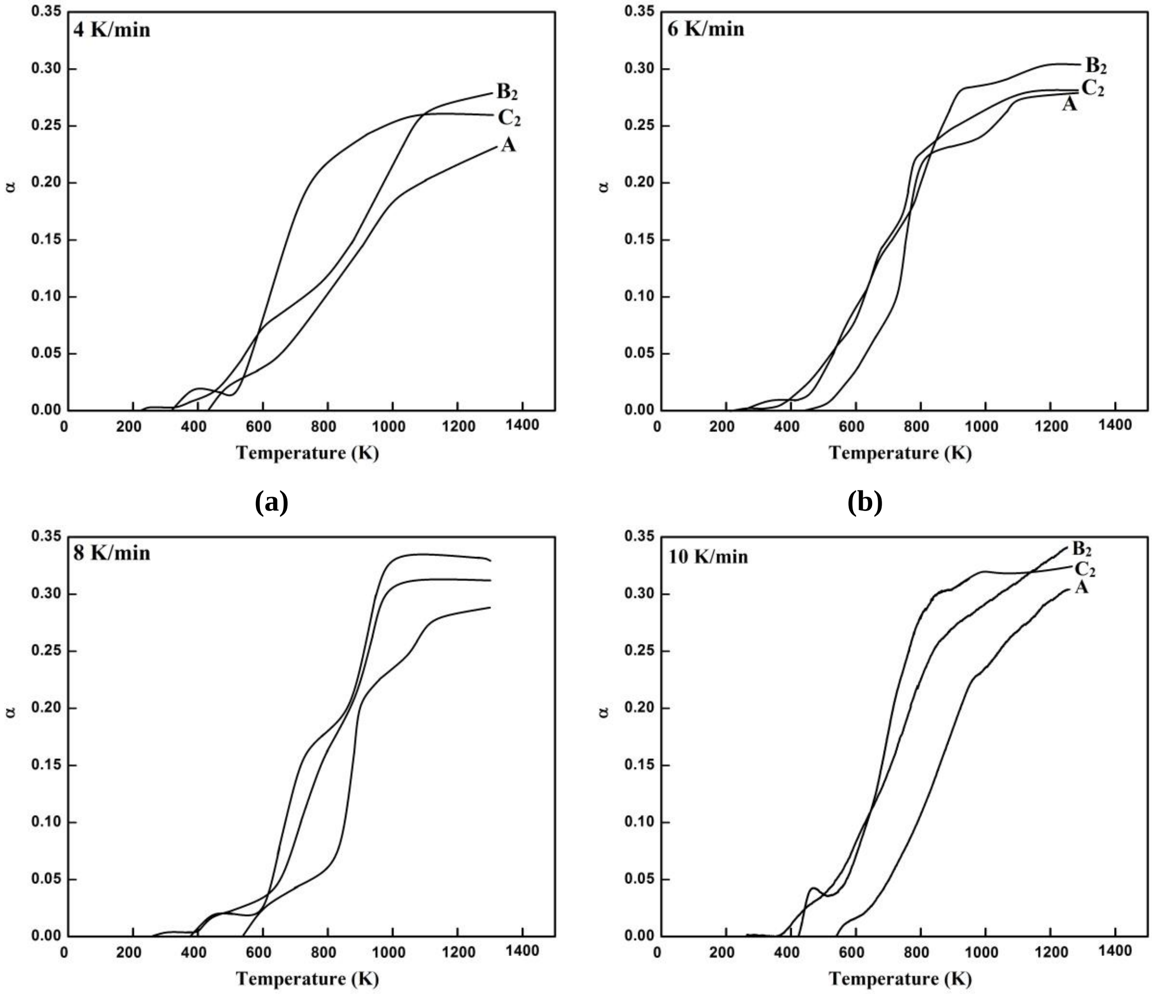

(a) (b)

(c) (d)

Figure 5.16: Non-isothermal oxidation behavior (α vs. T plot) of A, B_2 and C_2 alloys

The activation energy for the start of oxidation in all the alloys is calculated from the Kissinger plot using the onset temperature of oxidation at different heating rates (4-10 K/min), and the same is shown in Table 5.6. From the table it can be summarized that the energy values obtained from isothermal and non isothermal experiments are in close proximity. The alloy A shows clearly much higher activation energy for the start of oxidation suggesting a higher resistance for initiation of oxidation in comparison to the alloys B_2 and C_2.

Oxidation study of different alloys tells that addition of dispersion (TiO_2/Y_2O_3) deteriorate high temperature oxidation property of the present alloy. But, on the other hand it improves corrosion resistance of the alloy in aqueous medium due to similar mechanism.

Table 5.6: Activation energy for the start of oxidation in alloys A, B_2 and C_2 calculated from Kissinger plot

Alloy	Activation energy for the oxidation to start (kJ/mol)	Start temperature or oxidation (10 K/min)
A	94.36±2.16	620
B_2	80.61±1.96	500
C_2	78.63±1.53	380

5.5 Summary

In the present chapter, powders obtained from Mill-1 were conventionally sintered at 1400 ^oC for 1 h in Argon atmosphere in a vacuum furnace. The sintered product was subjected to characterize to understand the phase evolution and its related physical, mechanical, electrochemical and oxidation properties. Effect of dispersoids (nano TiO_2/Y_2O_3) addition on the above mentioned properties is summarized below.

- Phase evolution of consolidated products by XRD analysis showed presence of intermetallic compounds like Mo_2Zr, $FeZr_2$, NiZr and $Ni_{11}Zr_9$ along with TiO_2/Y_2O_3 phase in Zr matrix.

- From SEM analysis it was observed that grain growth has been taken place due to longer heating period at elevated temperature during conventional sintering. Presence of minor amount of porosity was visible from the SEM micrographs. EDS analysis confirms the presence of Zr along with other alloying elements.

- From bright and dark field TEM image and SAD analysis, presence of different intermetallics ($FeZr_2$, Ni_3Zr) of 20-30 nm size along with TiO_2/Y_2O_3 (10-20 nm) throughout the matrix was confirmed.

- It was found that hardness increases with increase in dispersion of TiO_2/Y_2O_3 and maximum hardness of 7.0 GPa was recorded for alloy B_2 compared to other alloys sintered at 1400 ^oC.

- Similar trend as hardness was also recorded during compressive test. Amongst all the alloys, alloy B_2 showed maximum compressive strength of 680 MPa.

- Wear test results display similar trend as that of hardness and compressive strength. The wear mechanism was found mainly abrasive in nature in all the samples.

- Potentio dynamic polarization test results indicate that increase in TiO_2 dispersion from 1 to 2 wt. % (alloy B_1 and B_2) decreases the corrosion rate drastically. On the other hand the alloy dispersed with Y_2O_3 (alloy C_1 and C_2) shows continuous decrease in corrosion rate from 0 to 2 wt. % Y_2O_3. Thus, alloy C_2 displays minimum corrosion rate (2.1678 mm/year X 10^{-2}) compared to all alloys discussed here.

- Samples sintered with addition of TiO_2/Y_2O_3 dispersoids (alloy B_2 and C_2) shows marginal higher oxidation rate in both isothermal and non isothermal study as compared to alloy A. Similar trend was noticed in terms of activation energy of oxidation calculated by both isothermal and non isothermal analysis.

Finally, it can be concluded that sample conventionally sintered with addition of TiO_2/Y_2O_3 dispersoids enhances mechanical properties in terms of hardness, compressive strength and wear resistance with marginally higher oxidation rate.

Chapter 6

Spark Plasma Sintering and Characterization

6.1 Phase and Microstructural Characterization

The 10 hours milled powders of all the alloys collected from Mill-2 were sintered in a spark plasma sintering unit at three different temperatures of 900, 950 and 1000 ^{o}C. To study the phase evaluation and morphology of the sintered products, the samples were characterized by X-ray diffraction (XRD), scanning electron microscopy (SEM) and Transmission electron microscope (TEM).

6.1.1 XRD Study

Figure 6.1 represents the XRD results of sintered products of alloy A, B_1, B_2, C_1 and C_2 at different sintering temperature (900, 950 and 1000 ^{o}C). From the XRD patterns of alloy A (Figure 6.1(a)) and with reference to its milled condition it can be observed that there was recrystallization after sintering. But, due to minor recrystallization, peak broadening still persists and change in peak position was also negligible. Moreover, with increase in sintering temperature there was not any appreciable change in the patterns. During sintering, formation of intermetallic compounds like MoNi, FeNi, Ni_3Zr, Mo_3Zr, Fe_3Zr and $Ni_{11}Zr_9$ was also noticed as shown in Figure 6.1(a). Due to the thermal activation during sintering, intermetallic formation of reactive metals is a common phenomenon. Formation of Zr based intermetallics during sintering in different systems was reported by several researchers [146]. It is worth mentioning that such intermetallics are capable of retaining toughness of the material at high temperature. In case alloys B_1 and B_2, C_1 and C_2 similar XRD results were obtained as shown in Figure 6.1(b) and (c), Figure 6.1(d) and (e) respectively. In those, along with these intermetallic compounds, presence of TiO_2, Y_2O_3 were confirmed in corresponding alloys.

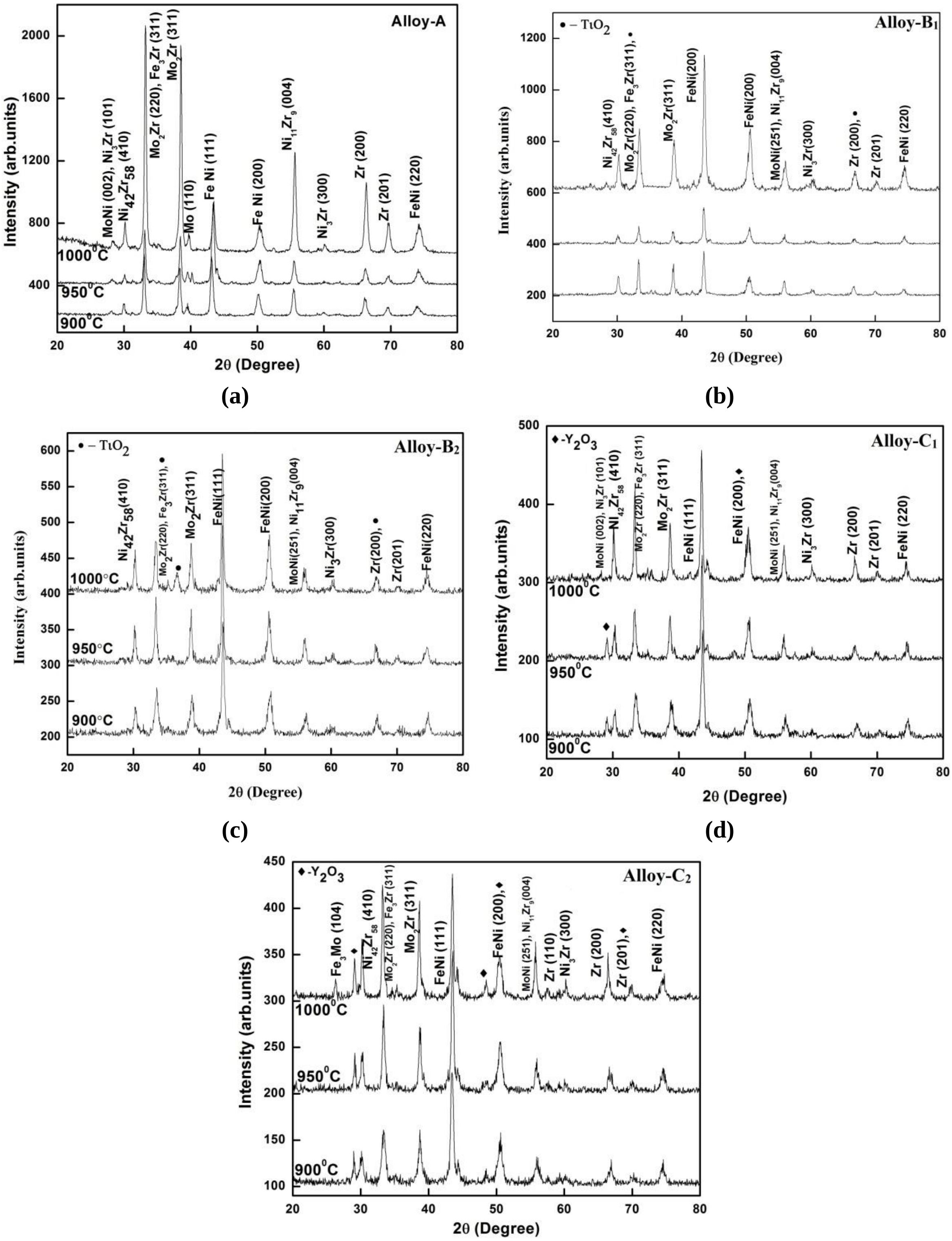

(a) **(b)**

(c) **(d)**

(e)

Figure 6.1: XRD patterns of sintered products of alloy (a) A, (b) B_1, (c) B_2, (d) C_1 and (e) C_2 at different sintering conditions

6.1.2 SEM/EDS Study

Figure 6.2 shows the FESEM images and corresponding EDS spectra of sintered samples of alloys A, B_2 and C_2 consolidated at 1000 ^{o}C. There was no substantial grain growth after sintering and neck formation was also observed. In some specific region of the micrograph liquid phase formation took place possibly due to localized high temperatures during SPS. Due to the small sintering time in SPS the grain size was limited to 100-200 nm. Similar fine structure using SPS was reported earlier [147]. The EDS spectra showed the presence of all alloying elements.

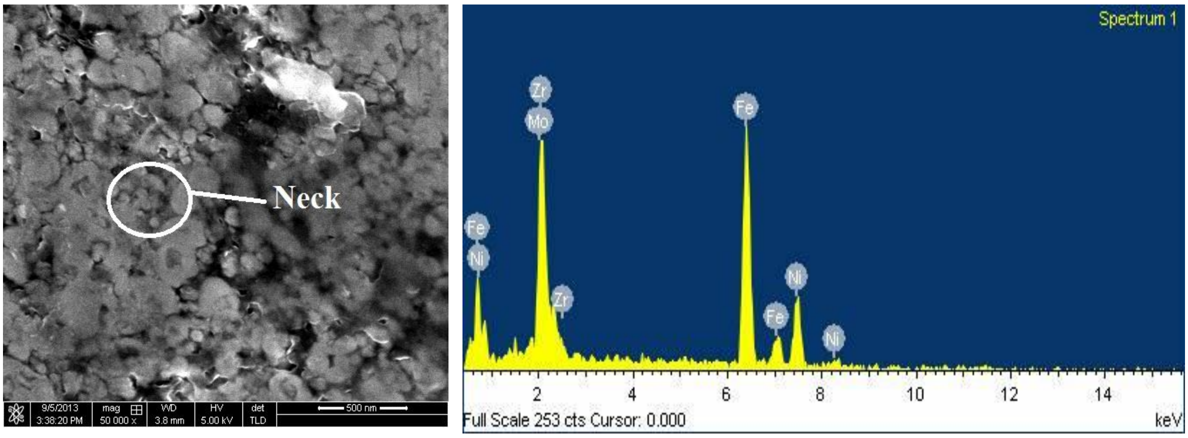

(a)

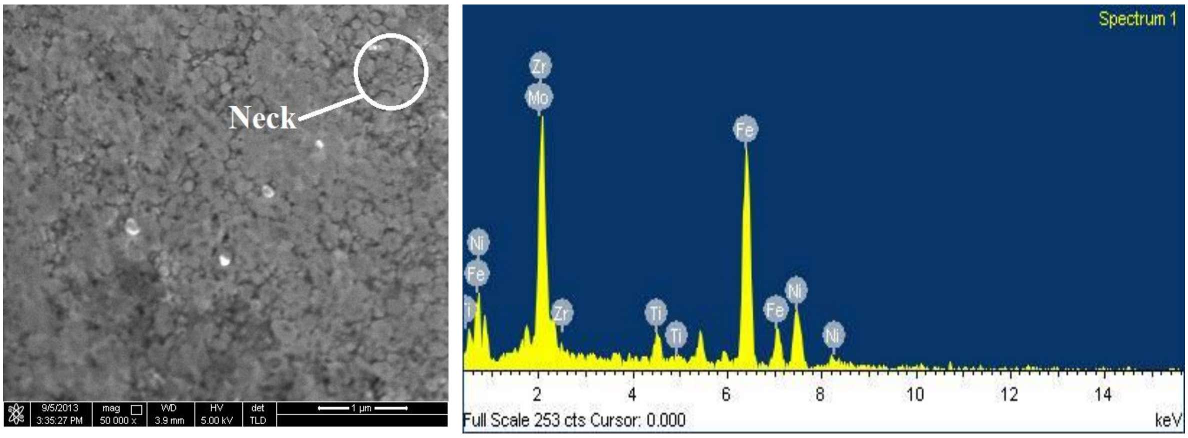

(b)

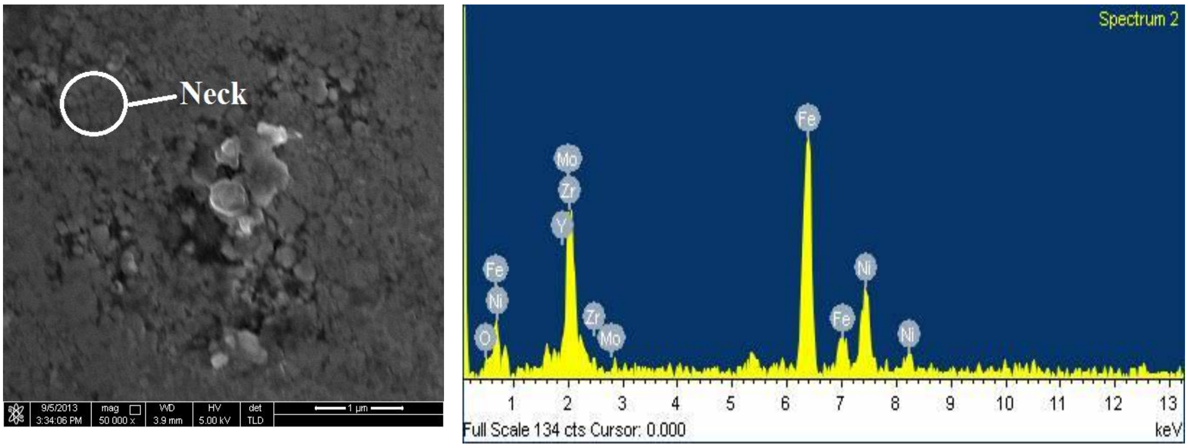

(c)

Figure 6.2: SEM photographs and corresponding EDS spectra of alloy (a) A, (b) B_2 and (c) C_2 sintered at 1000 ^{o}C

6.1.3 TEM Study

Figure 6.3 shows the TEM micrographs of SPS (sintered at 1000 ^{o}C) products of alloy A, alloy B_2 and alloy C_2. In the bright field TEM image (Figure 6.3A(a)), continuous dense appearance of the matrix was evident which can be due to partial liquid phase sintering as indicated earlier from the SEM analysis (Figure 6.2(a)). The SAD pattern (bright spots and intermittent diffraction rings) of alloy A confirmed the formation of FeNi and Mo_2Zr intermetallics after mapping the *d* spacing (0.178 nm for Zr (201), 0.227 nm for Mo_2Zr (311) and 0.127 nm for FeNi (220)) of these with the observed rings. Presence of these was also indicated by XRD study (Figure 6.1(a)).

Figure 6.3(B_2) represents the bright and dark field images and corresponding SAD pattern of the alloy B_2. From the bright and dark field images (Figure 6.3B_2(a) and 6.3B_2(b)) it can be observed that the secondary and intermetallic phases of 10-20 nm size were distributed uniformly in the matrix. The analysis of SAD pattern (Figure 6.3B_2(c)) confirmed the presence of (110) plane of TiO_2 (*d* spacing 0.349 nm), (311) plane of Fe_3Zr (*d* spacing 0.268 nm) and (111) plane of FeNi (*d* spacing 0.207 nm).

Figure 6.3(C_2) represents the bright and dark field images and corresponding SAD pattern of the alloy C_2. From the bright and dark field images (Figure 6.3C_2(a) and 6.3C_2(b)) it can be observed that Y_2O_3 and other intermetallics of 10-20 nm size were uniformly distributed within a nano crystalline matrix. In Figure 6.3C_2(c), one specific interplanar spacing was measured as 0.305 nm, which corresponds to the interplanar spacing of BCC

Y_2O_3. It is evident from the image (Figure 6.3C_2(d)) that the sample consists of several nano crystalline grains. SAD pattern of alloy C_2, (Figure 6.3C_2(d)), presence of (200) plane of FeNi (*d* spacing 0.181 nm), (220) plane of Mo_2Zr (*d* spacing 0.269 nm) and (313) plane of Y_2O_3 (*d* spacing 0.21 nm) were confirmed. Presence of these phases was also confirmed by the XRD analysis (Figure 6.1(e)). Formation of intermetallics is a common phenomenon during sintering of mechanically alloyed powder as recently reported by Karak et al. for nano Y_2O_3 dispersed ferritic alloys [148], Roy et al. for nano TiO_2 dispersed Al based alloys and others [149]. Metastable extended solid solution formed during milling tend to form intermetallics as per their contributing elements and chemical affinity with help of thermal energy supplied during sintering and release of stored milled energy.

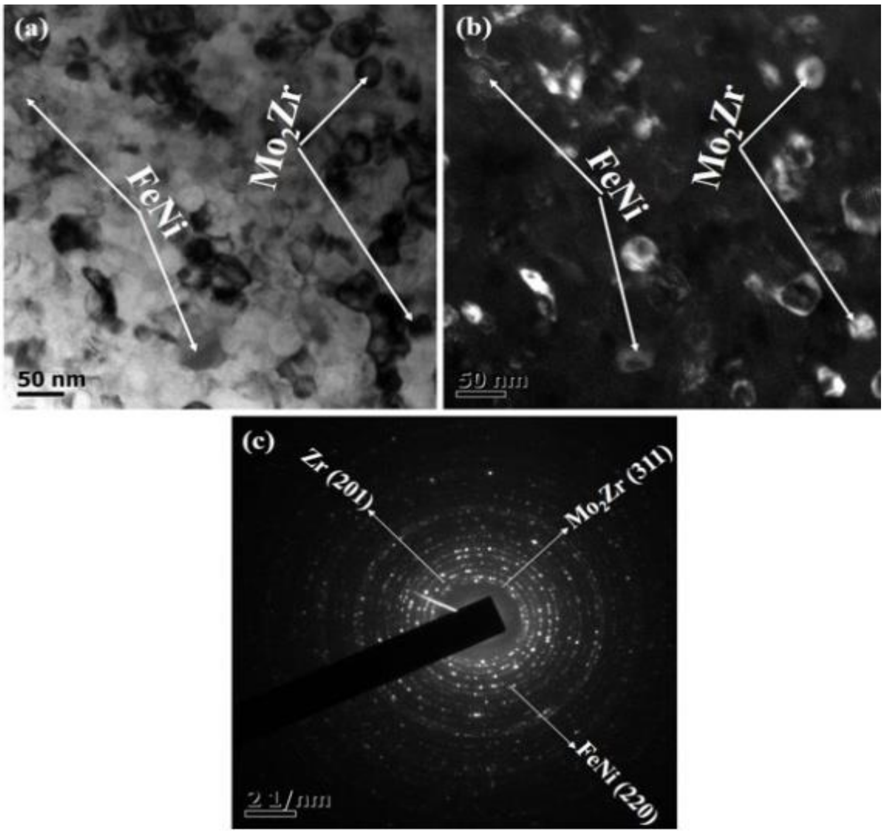

A

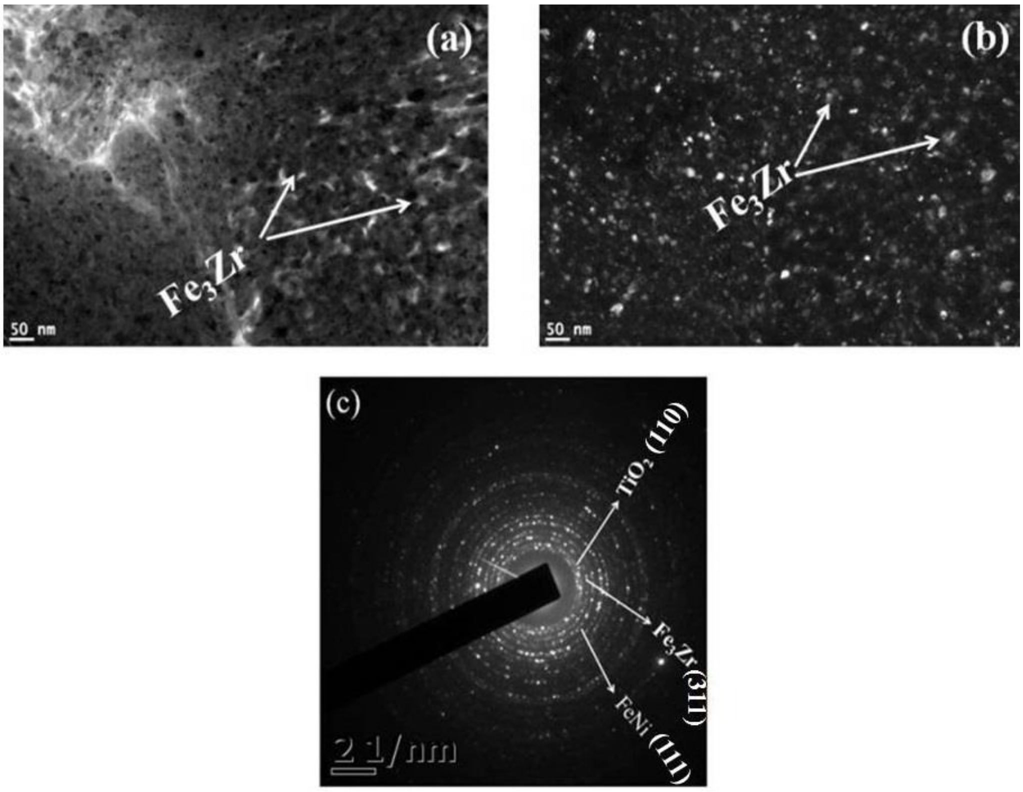

B$_2$

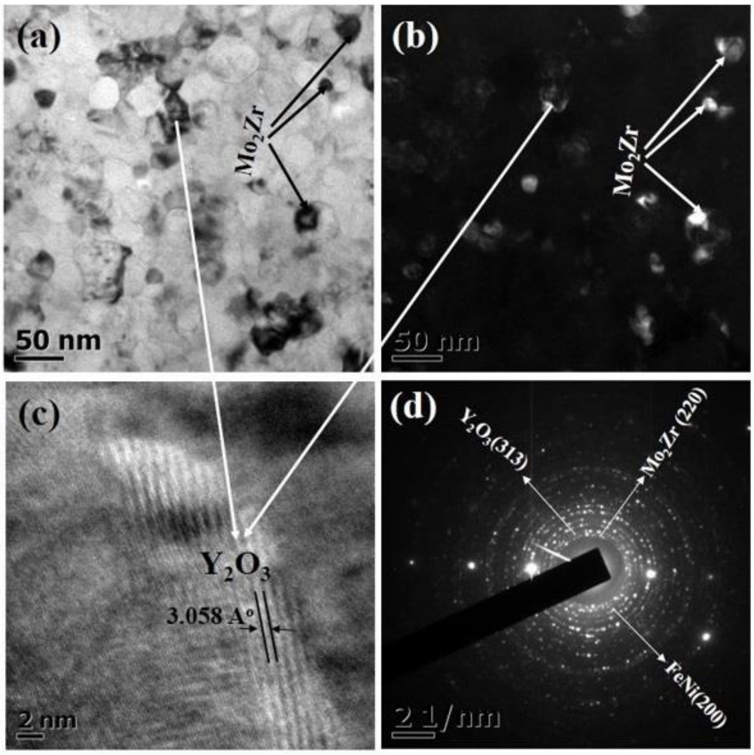

C$_2$

Figure 6.3: (a) Bright field, (b) dark field TEM images and corresponding SAD patterns of alloy A, B$_2$ and C$_2$ sintered at 1000 ^{o}C

6.2 Physical and Mechanical Property Study

6.2.1 Density

Figure 6.4 shows the densities of spark plasma sintered samples of alloy A, B_1, B_2, C_1 and C_2 at sintering temperatures of 900, 950 and 1000 ^{o}C. It can be observed that with increase in SPS temperature, the density increases. The maximum density achieved was nearly 99.5% of the theoretical density (alloy A, 1000 ^{o}C). SPS technique involves short time uniform sintering of amorphous/metastable phase materials involving vaporization, melting on the particle surface by simultaneous application of temperature and pressure, which leads to development of high density products. In the present study, possible partial liquid phase formation also attributes towards achievement of high density. The density values of all the sintered alloys are summarized in Table 6.1.

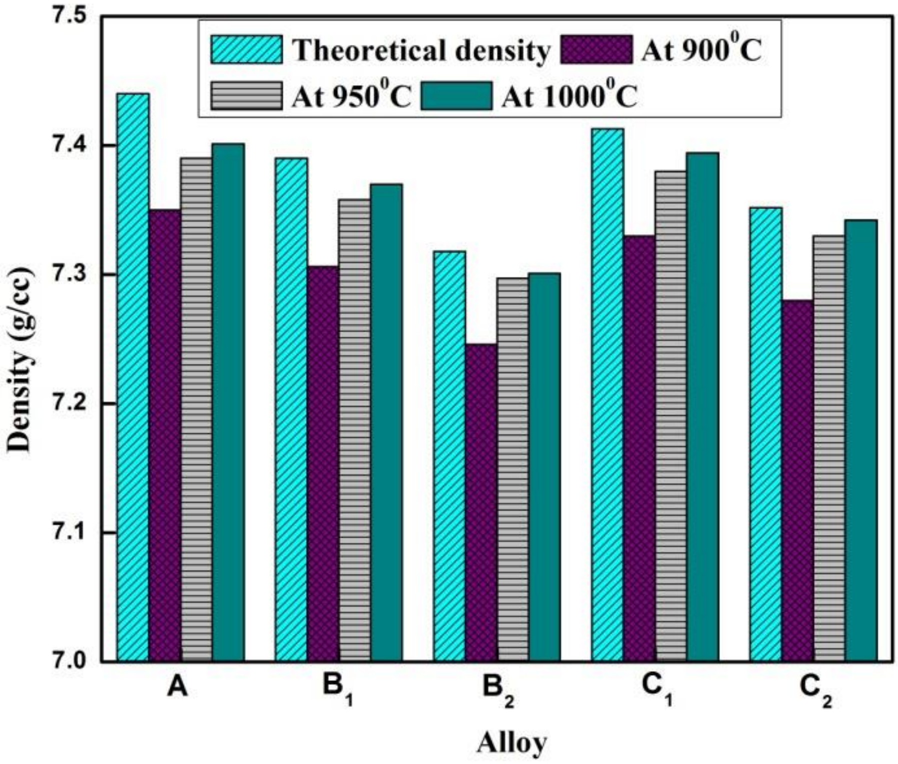

Figure 6.4: Variation of density with alloy composition and sintering temperature

Table 6.1: Density values of sintered products of alloy A, B_1, B_2, C_1 and C_2

Alloy	Theoretical density (g/cc)	Sintering temperature (^{o}C)	Density (g/cc)	% Theoretical density
A	7.440	900	7.350	98.79
		950	7.390	99.32
		1000	7.401	99.47
B_1	7.390	900	7.306	98.86
		950	7.358	99.56
		1000	7.370	99.72
B_2	7.318	900	7.246	99.01
		950	7.297	99.71
		1000	7.301	99.76
C_1	7.4128	900	7.330	98.88
		950	7.380	99.55
		1000	7.394	99.74
C_2	7.3516	900	7.280	99.02
		950	7.330	99.70
		1000	7.342	99.86

6.2.2 Hardness

Figure 6.5 shows the hardness values of spark plasma sintered samples of alloy A, B_1, B_2, C_1 and C_2 at sintering temperatures of 900, 950 and 1000 ^{o}C. It can be observed that with increase in SPS temperature, the hardness increases. It was also observed that hardness values of all the sintered samples were also affected by amount of dispersion (TiO_2/Y_2O_3). Moreover, in spite of partial liquid phase formation, fineness of the matrix and the intermetallics/dispersoids still persists due to characteristics of SPS process; i.e., very high heating rate and low sintering time. The maximum hardness values achieved in the present study was 16.853 GPa in alloy B_2 and 16.19 GPa in alloy C_2 sintered at 1000 ^{o}C. Conventional sintering of similar systems yields maximum hardness value of 6.96 GPa as reported earlier in the previous chapter. The current alloys achieve high hardness compared to commercially available pure cold-rolled Zr or Zircaloy-2 (ASTM UNS Grade R60802) whose hardness is in the range 0.85 to 2.2 GPa. The hardness values of alloys are also mentioned in Table 6.2.

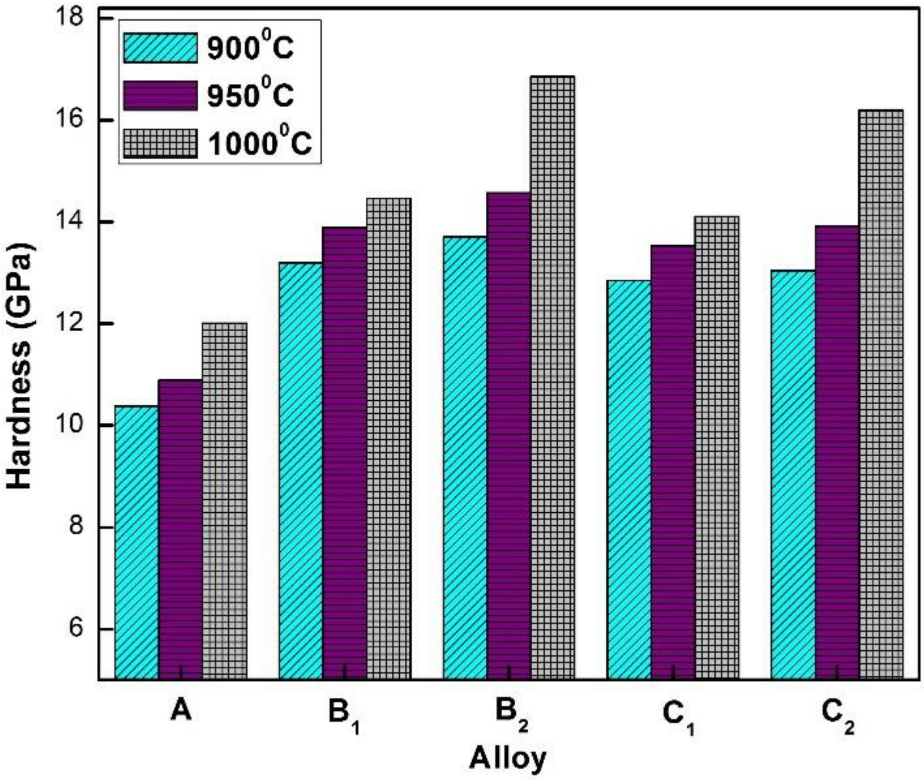

Figure 6.5: Variation of hardness with alloy composition and sintering temperature

Table 6.2: Hardness values of sintered products of alloy A, B_1, B_2, C_1 and C_2

Alloy	Sintering temperature (°C)	Hardness (GPa)
A	900	10.38
	950	10.89
	1000	12.01
B_1	900	13.20
	950	13.88
	1000	14.46
B_2	900	13.71
	950	14.57
	1000	16.85
C_1	900	12.85
	950	13.53
	1000	14.11
C_2	900	13.04
	950	13.91
	1000	16.19

6.2.3 Compressive Strength

Figure 6.6 represents the compressive stress-strain curves of alloy A, B_1, B_2, C_1 and C_2 sintered at 900 ^{o}C obtained by using a universal testing machine (Instron SATEC-600 kN & 1000 kN) at room temperature with cross head velocity of 0.2 mm/min. Compressive test results indicate that the compressive strength was increased by the increase of 1-2 wt. % TiO_2/ Y_2O_3 dispersion and by the increasing sintering temperature as well. This is due to the fact that enchantment of compressive strength of the alloys attributed by solid solution strengthening and dispersion strengthening mechanism. However, the compressive elongation of alloys gradually decreases with increase in the amount of dispersoid (nano-TiO_2/ Y_2O_3) in the Zr matrix. According to Griffith theory, the ductility drops with the presence of micro cracks which act to concentrate the stress at their tips and the stress distribution in the vicinity of crack under constant velocity. The maximum compressive strength and deformation to fracture values are listed in Table 6.3. It can be observed that fracture strain was maximum (0.12) in alloy A. According to the previous research reports, the alloys discussed in the present study shows appreciable increase in deformation along with higher strength value [150].

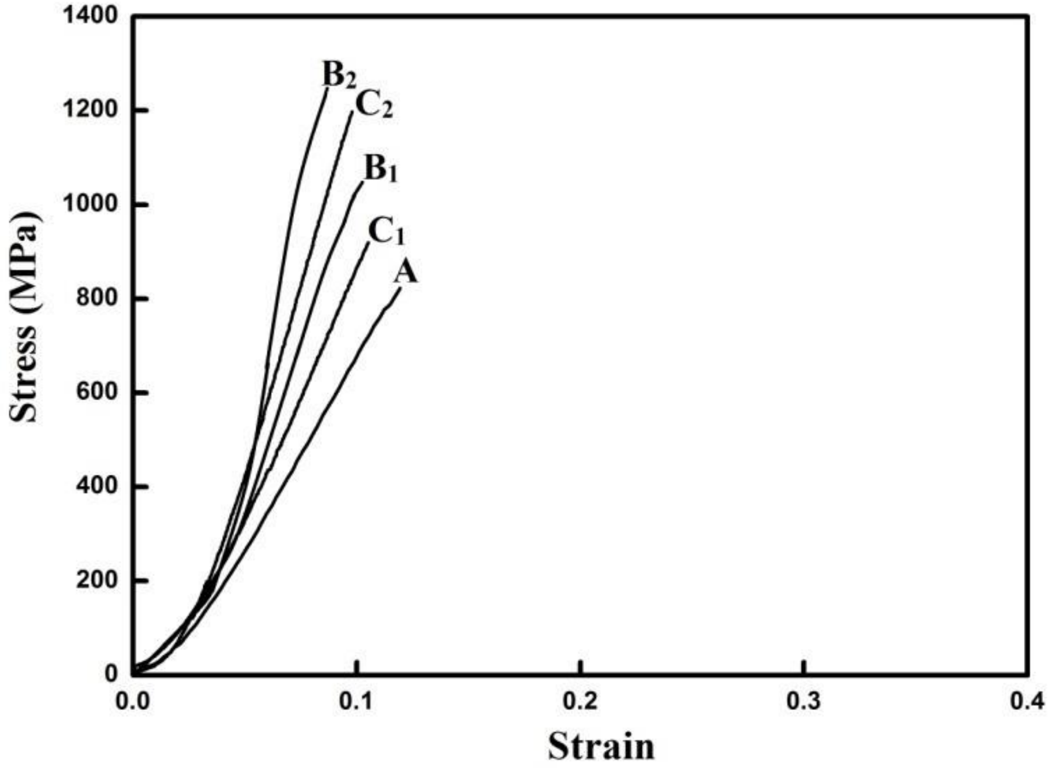

Figure 6.6: Compressive stress strain curves of sintered products of alloy A, B_1, B_2, C_1 and C_2

Table 6.3: Compressive strength and strains of sintered products of alloy A, B_1, B_2, C_1 and C_2

Alloy	Compressive strength (MPa)	Strain
A	825	0.120
B_1	1032	0.103
B_2	1240	0.094
C_1	919	0.105
C_2	1199	0.100

SEM fractographs of compressive specimens are shown in Figure 6.7. All the fracture surfaces mainly exhibit brittle fracture with presence of micro pores, quasi cleavage planes and facets. Due to this, fractographs of the alloys resemble amorphous matrix.

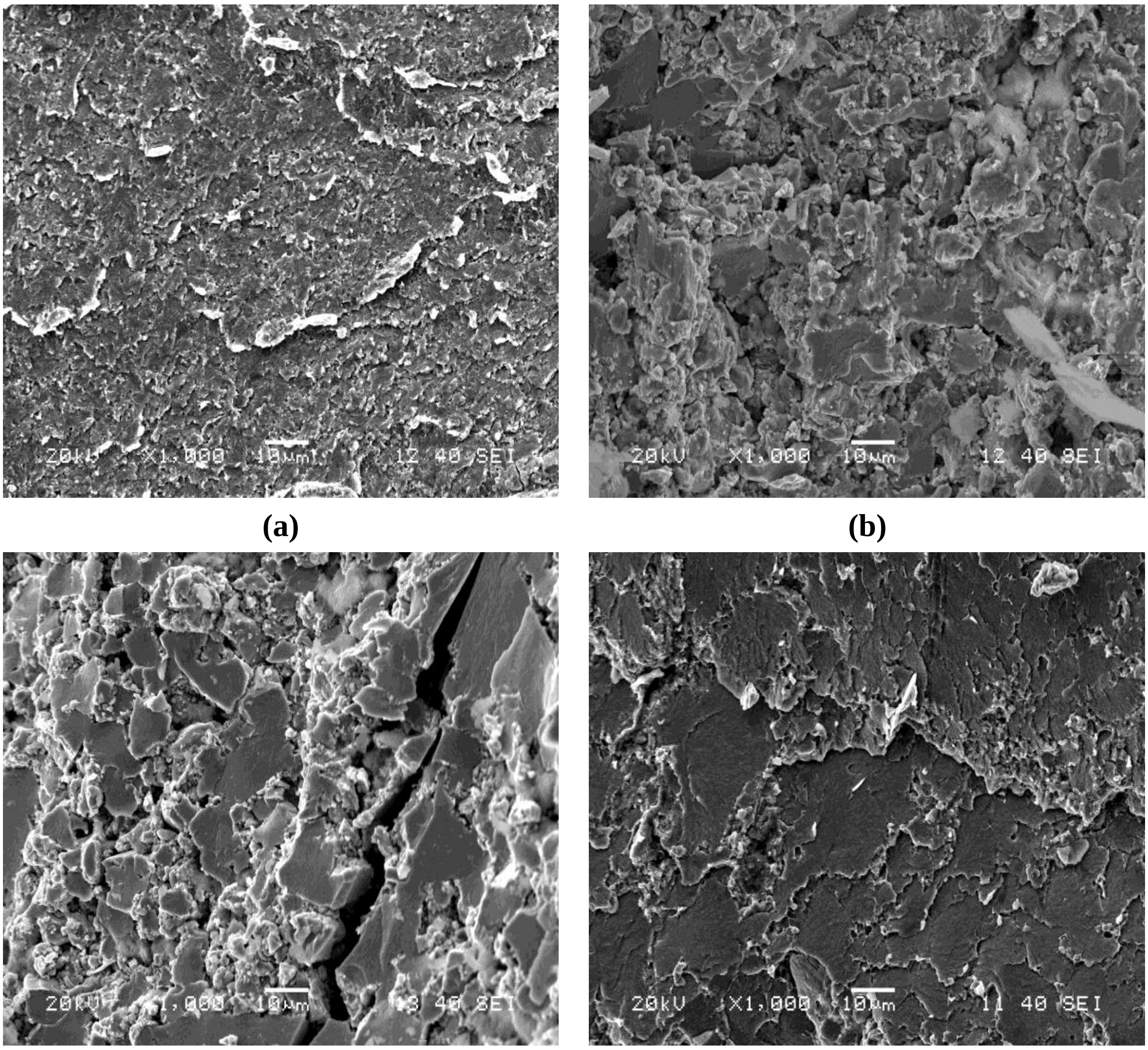

(a) **(b)**

(c) **(d)**

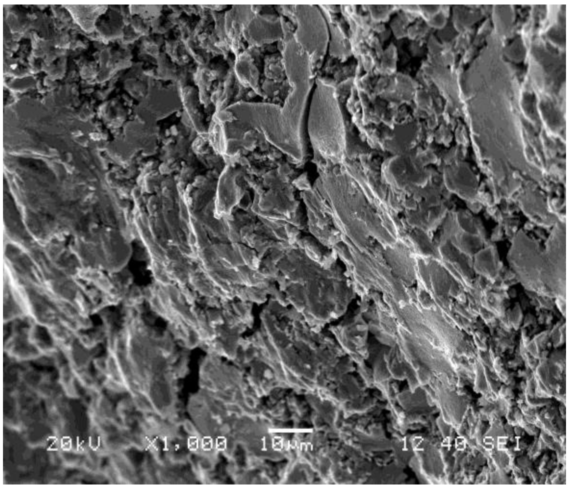

(e)

Figure 6.7: SEM images of fractured surfaces of alloy (a) A, (b) B_1, (c) B_2, (d) C_1 and (e) C_2

In case of alloys B_2 and C_2, presence of micro voids and cracks was more pronounce due to presence of higher amount of dispersoid phase. As amount dispersoid was increased, brittleness increases due to the pile up of layers, pinning of layer gliding and formation of intermetallics associated with Fe, Ni, Mo and Zr.

6.2.4 Wear

To study the mechanical properties of the sintered products, ball-on-plate type wear testing was carried out on samples of alloys A, B_1, B_2, C_1 and C_2 sintered at 1000 ^{o}C, as they showed better hardness compared to others. Figure 6.8 shows the variation of wear depth as a function of sliding distance at 40 N normal load with 20 rpm speed on a 4 mm diameter track. Such wear test was carried out for 10 minutes with linear velocity of 0.004186 m/s on the sintered products using a diamond indenter having Rockwell geometry. From the figure, it is evident that the variation of wear depth as a function of sliding distance was similar in manner i.e., with sliding distance wear depth increases. Minute observation revealed that upto 100 cm of sliding distance, alloy A and C_1 shows maximum wear depth compared to others leading to end result of poorest wear depth of alloy A and C_1 amongst the all at final stage. In other words the slope of the plot (which can be designated as wear rate) is steeper or poor for alloy A and C_1 compared to alloy B_1, B_2 and C_2. In initial stage of this type of wear test there is sudden rise in wear depth due to engagement of the indenter with the specified load. After that the material property shows its actual nature in terms of its wear characteristics. In case of alloys B_1, B_2 and C_2, after initial sliding/deformation, dislocation movement is hindered by the presence of dispersoid (TiO_2/ Y_2O_3) which is absent in alloy A. This mechanism leads to lower rate of wear in case of alloy B_1, B_2 and C_2 as shown in the figure. Moreover, the final wear characteristics shown in Figure 6.8 matches well with hardness values reported in earlier section.

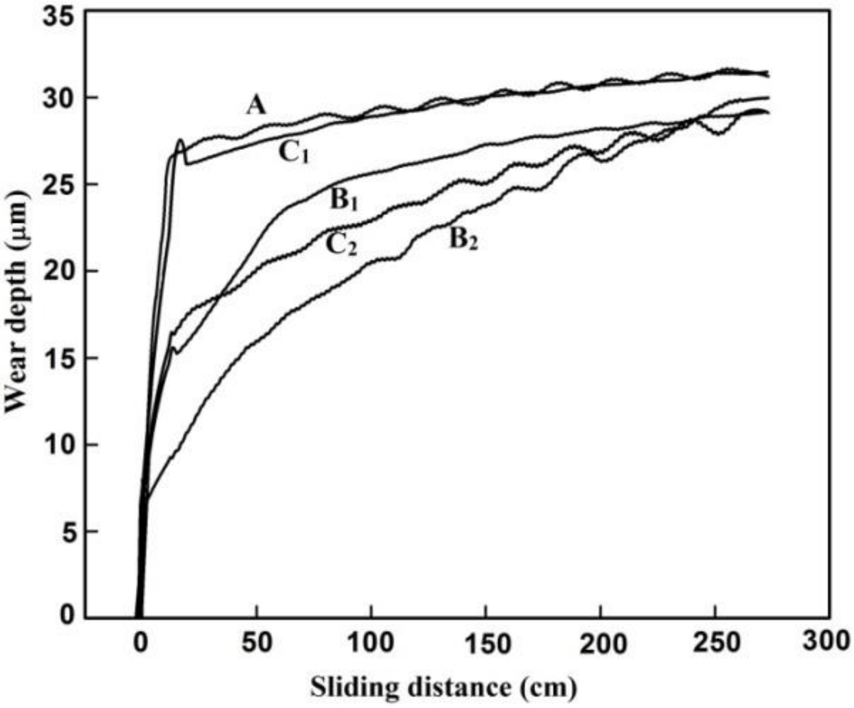

Figure 6.8: Wear test results of sintered products of alloy A, B_1, B_2, C_1 and C_2 sintered at 1000 °C

The worn out surfaces produced by the wear test was subsequently analyzed by field emission scanning electron microscope as shown in Figure 6.9. From the figure it can be observed that the width of the wear track is maximum for alloy A and C_1, minimum in case of alloys B_2 and C_2 representing the same outcome obtained in wear plot. The appearance of the wear track was shiny and consisted of scratching/rubbing mark throughout the track. This type of smooth appearance is exhibited in case of abrasive/brittle wear. But, at the inner edges of the wear track there are minor marks of material flow which is characteristics of adhesive kind of wear. Moreover, in case of alloy B_2 and C_2 the inner edges show discontinuous material flow as compared to alloy A and C_1 as these have better strength/brittleness for the dispersion. Therefore, the overall wear mechanism of these materials discussed in the study is mainly abrasive in nature with minor of shift towards adhesive nature. Moreover, in case of alloy B_1, B_2 and C_2, worn out TiO_2 and Y_2O_3 particles respectively may act as the third body leading to abrasive wear three body motion mechanism as reported earlier by Parida et al [151].

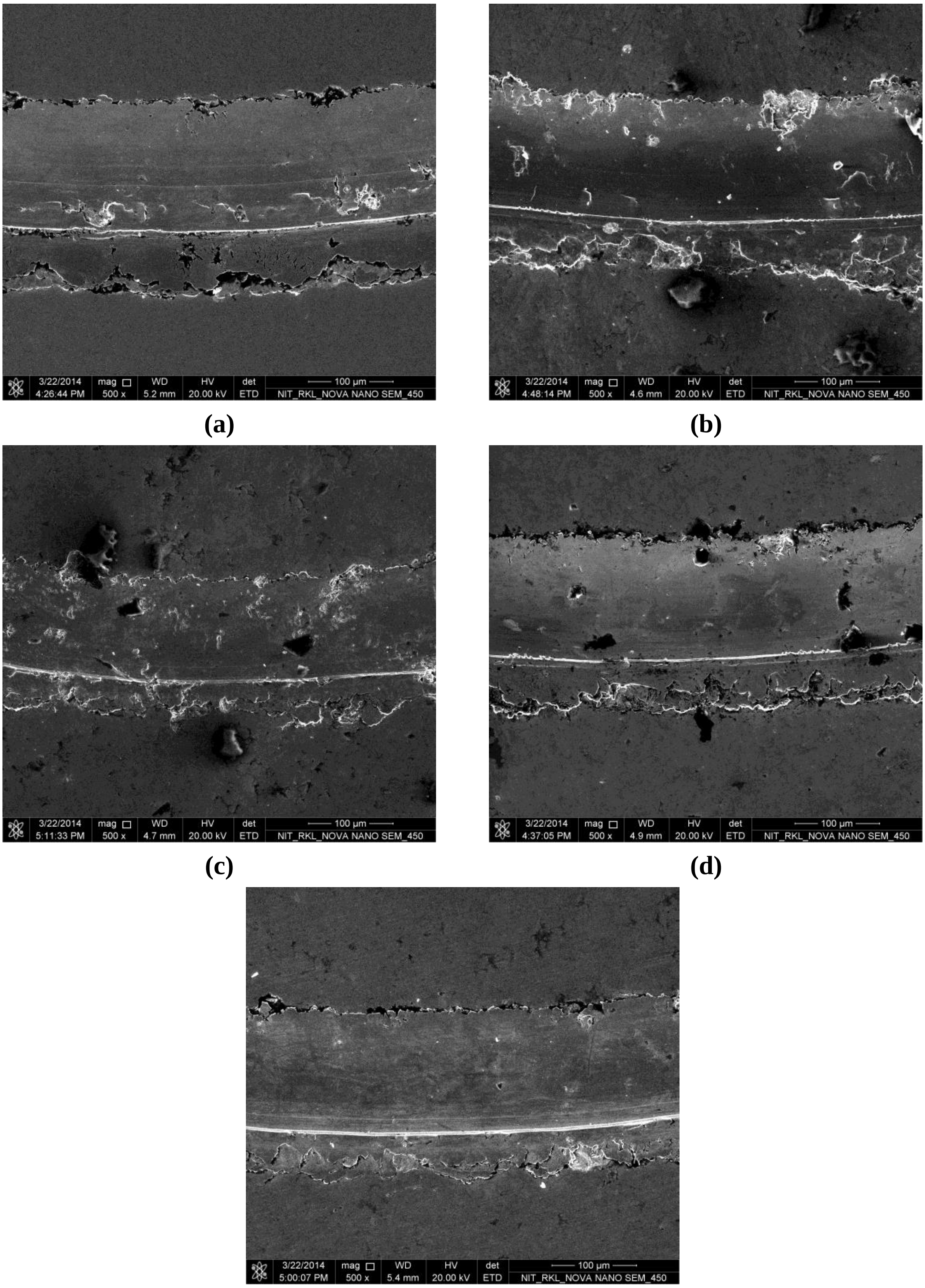

(a) **(b)**

(c) **(d)**

(e)

Figure 6.9: FESEM micrographs of worn surfaces of alloy (a) A, (b) B_1, (c) B_2, (d) C_1 and (e) C_2

6.3 Corrosion study

Figure 6.10 shows polarization curves of alloy A, B_1, B_2, C_1 and C_2 in 3 mole NaCl electrolyte solution treated from -1.5 to +0.5 V (vs. Saturated Calomel electrode; SCE) with scan rate 0.008002 V/s and step potential 0.00244 V. The corrosion current and corrosion potential acquired from fitting the polarization curves are listed in Table 6.4. According to the results, the oxide dispersion of 1-2 wt. % TiO_2/Y_2O_3 enhanced the corrosion resistance in alloys B_2 and C_2. The alloy A acquired highest corrosion potential of -0.825 V and less corrosion rate than TiO_2 dispersed alloys B_1 and B_2; but the corrosion resistance of alloy B_2 is better than alloy B_1. Moreover alloy A has more corrosion rate than Y_2O_3 dispersed alloys C_1 and C_2. This demonstrates that the corrosion rate has been decreased by 2 wt. % TiO_2/Y_2O_3 in alloys B_2 and C_2. This phenomenon can be explained by the poor quality of the formation of ZrO_2 layer. Alloy A has coarse grain structure, alloy B_1 has finer structure obtained by addition of TiO_2 and this increases the corrosion rate. But the probability of formation of ZrO_2 was higher with the addition of higher amount of TiO_2 helps in formation of high dense adherent oxide layer. Similar trend was observed in alloys C_1 and C_2 also. Similar trend was also observed in previous chapter where conventional sintered samples were studied.

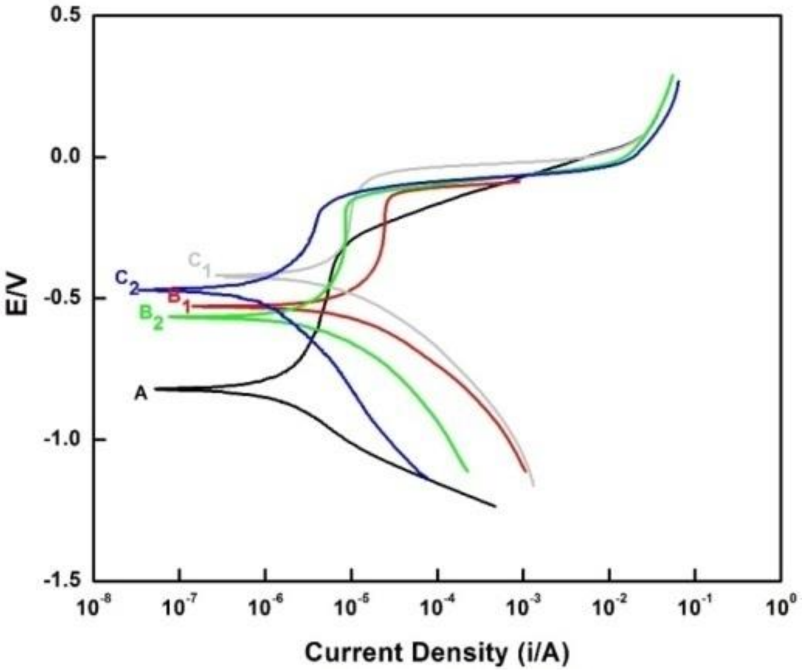

Figure 6.10: Potentiodynamic polarization curves for alloys A, B_1, B_2, C_1 and C_2 in 3 Mole NaCl solution

Table 6.4: Potentiodynamic test result of alloy A, B_1, B_2, $C_1$and alloy C_2 in 3 Mole NaCl solution

Alloy	E_{corr} (V) observed	E_{corr} (V) calculated	Corrosion rate (mm/year)$X10^{-2}$	I_{corr} (A/cm^2)$X10^{-6}$
A	-0.825	-0.853	5.010	2.350
B_1	-0.533	-0.548	19.52	11.10
B_2	-0.566	-0.560	8.262	4.636
C_1	-0.421	-0.397	2.172	1.220
C_2	-0.478	-0.473	1.713	0.940

Figure 6.11 shows the surface morphology of the zirconium alloys after potentio dynamic polarization test in 3 mole NaCl solution. It indicates that the corrosion on surface of alloy B_2 and C_2 was uniform and showed formation of strong aggregates of oxide layer (Figure 6.11(d) and (e)). The irregular and porous morphology that appears in alloy B_1 and C_1 (Figure 6.11(b) and (c)), is due to the sudden changes in ionic concentration by the dispersion of TiO_2 and Y_2O_3 respectively. Zirconium show high passivity in oxidizing environment due to the formation of thin oxide film (ZrO_2) on the surface. Initially with 1 wt. % TiO_2/Y_2O_3 the formation of oxide layer was severe but with 2 wt. % TiO_2/Y_2O_3 changes in ionic concentration was negligible and doesn't affects the diffusivity of ions near electrolyte surfaces. At these concentrations the diffusion of ions becomes slow and oxide layer inhabits the further corrosion by separating the metals from the electrolyte.

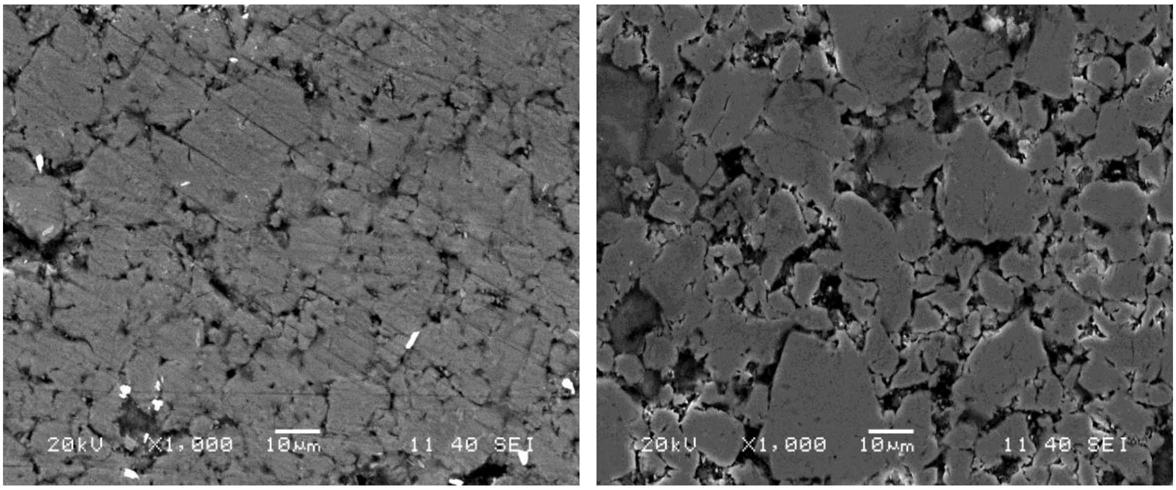

(a) **(b)**

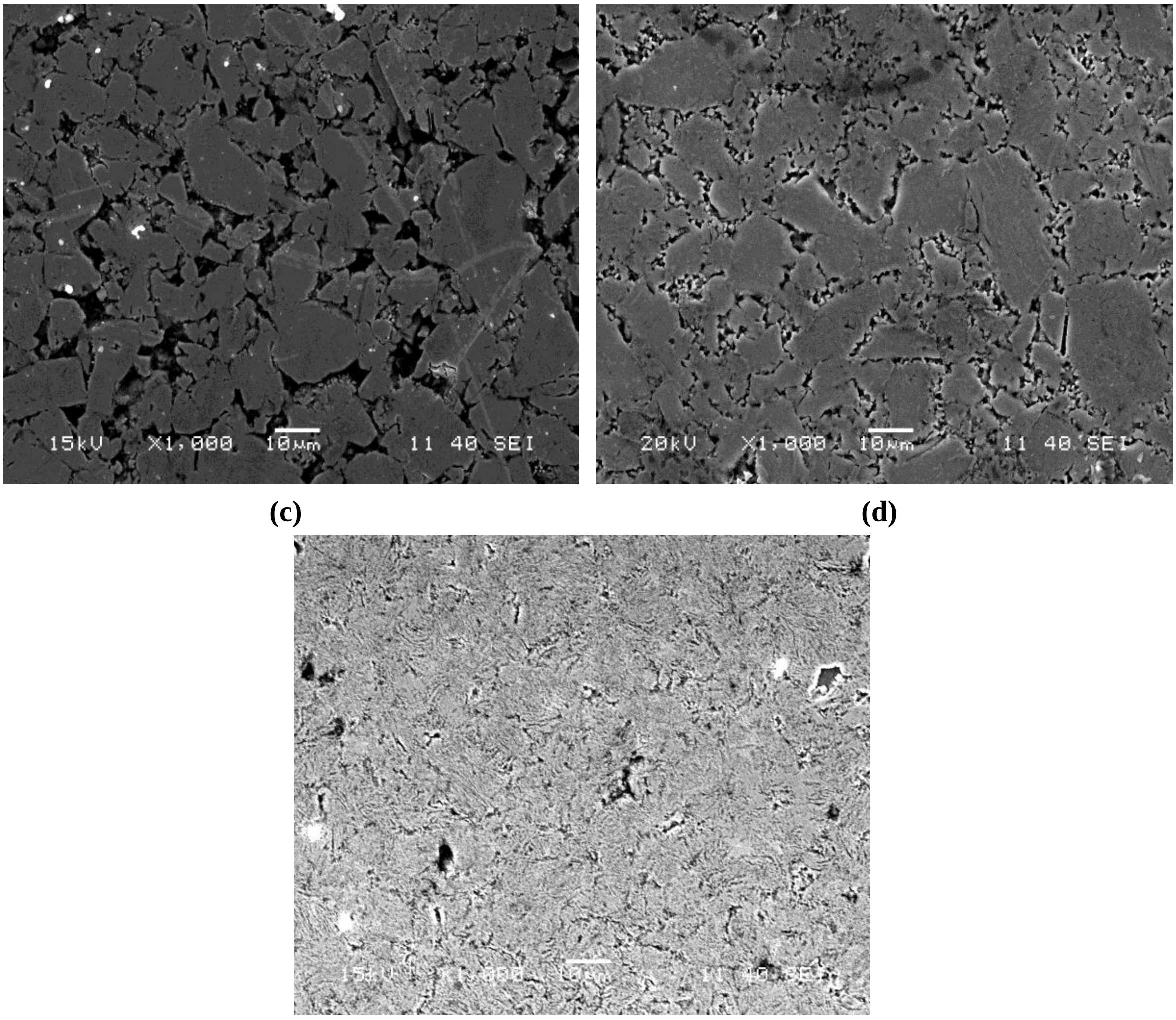

(c) **(d)**

(e)

Figure 6.11: Surface morphologies of alloy (a) A, (b) B_1, (c) B_2 (d) C_1 and (e) C_2 after potentiodynamic polarization test in 3 mole NaCl solution

6.4 Oxidation Study

6.4.1 Isothermal Oxidation

Figure 6.12 shows the isothermal oxidation kinetics of alloy A, B_2 and C_2 carried out at 900, 1000 and 1100 ^{o}C for 50 hours. The oxidation follows parabolic rate law in case of all three alloys. Figure 6.13 compares the rate constant of isothermal oxidation (K_p) during exposure to 900, 1000 and 1100 ^{o}C in dry air for alloy A, B_2 and C_2. From Figure 6.12 (a), (b) and (c) it was seen that with increasing oxidation temperature the weight gain/oxidation increases as expected. When all the figures were compared then it was observed that for alloy A, the weight gain is lower than the alloys B_2 and C_2 at each oxidation temperature. The figure shows that oxidation is more in case of alloy C_2 and less for alloy A. Activation energy for isothermal oxidation is calculated from $ln(K_p)$ versus $1/T$ plots are shown in Figure 6.12.

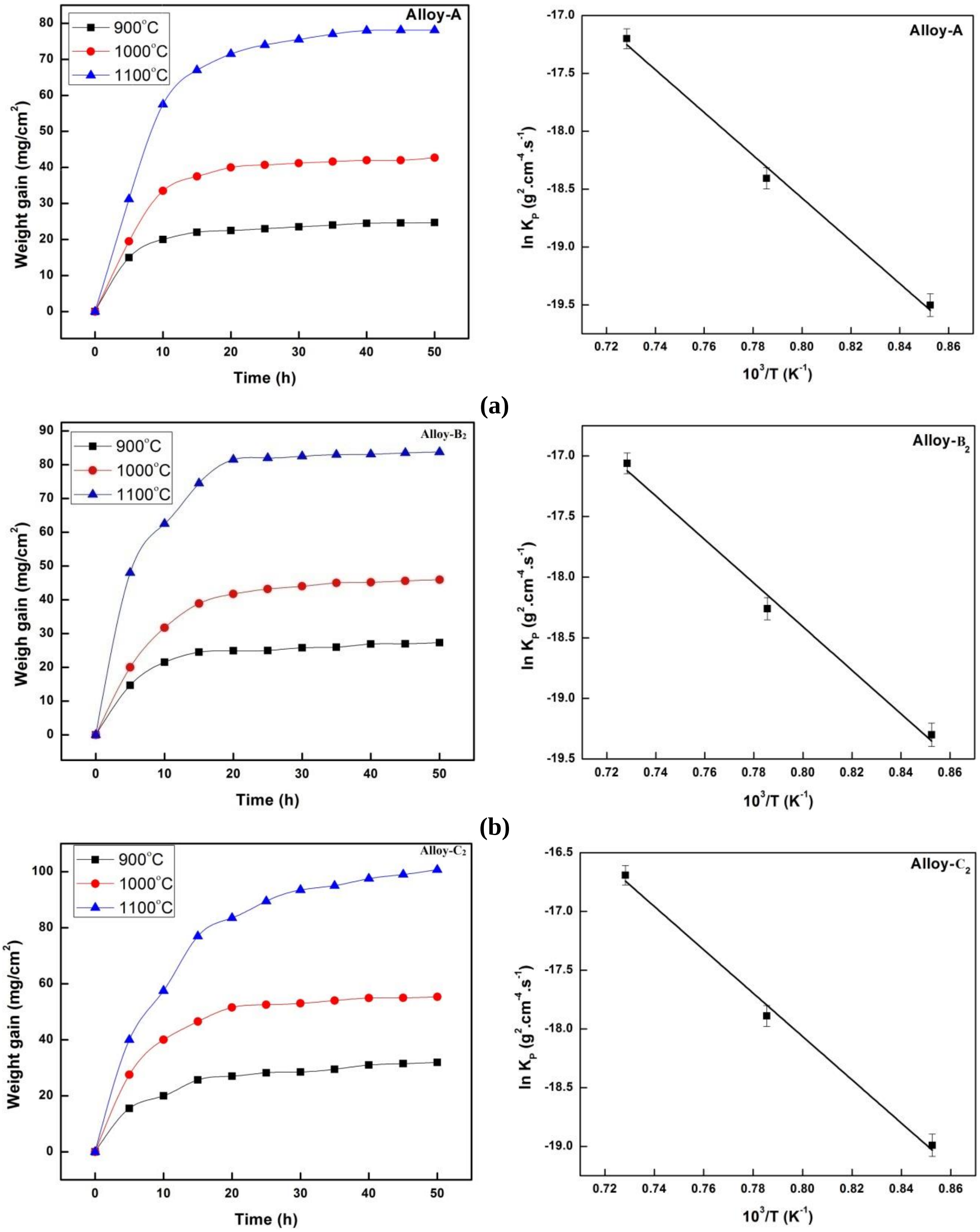

(a)

(b)

(c)

Figure 6.12: Isothermal oxidation kinetics and their corresponding Arrhenius plot for alloy (a) A, (b) B_2 and (c) C_2 at 900, 1000 and 1100 °C in air for 50 hours

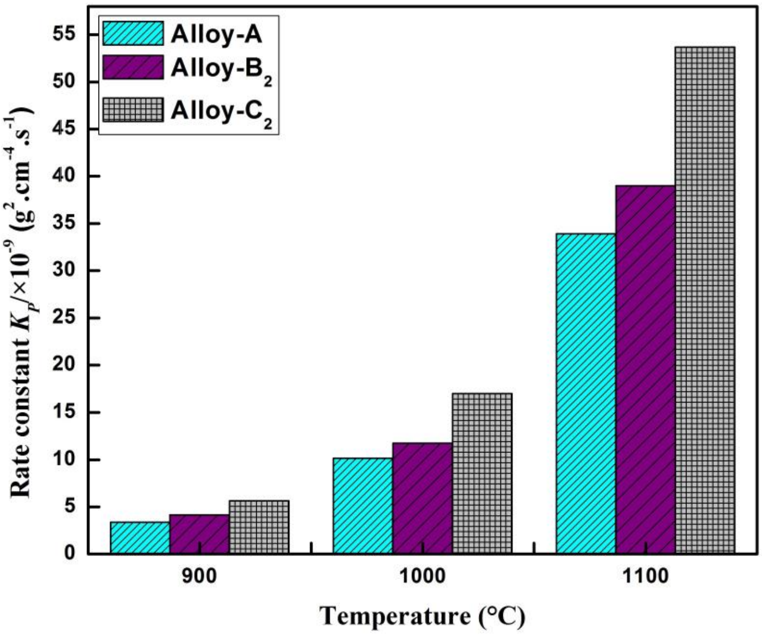

Figure 6.13: Kinetics of isothermal oxidation in terms of rate constant as a function of temperature for alloys A, B_2 and C_2

Table 6.5 shows that the rate constants and activation energies as calculated from isothermal results over the temperature range of 900-1100 °C. The activation energy for oxidation of alloy A is higher than alloy B_2 and C_2. Here it is evident that with presence of dispersoids in alloys, the activation energy decreases and hence the oxidation rate increases. Same trend was observed during oxidation study of conventionally sintered alloys. But, the activation energies reported here are higher than those of conventionally sintered samples. Though oxidation kinetics is highly grain boundary diffusion driven mechanism and samples sintered with SPS techniques shows finer grain size, less porosity makes the SPS alloys more oxidation resistance.

Table 6.5: Arrhenius parameters of isothermal oxidation of alloys at different temperatures

Alloy	Temperature (°C)	Rate constant K_P X10^{-9} ($g^2.cm^{-4}.s^{-1}$)	Activation energy (kJ/mol)
A	900	3.39	153.57±1.32
	1000	10.13	
	1100	33.89	
B_2	900	4.15	149.31±1.57
	1000	11.74	
	1100	38.98	
C_2	900	5.65	149.65±1.30
	1000	17.00	
	1100	53.69	

The XRD patterns of oxidized samples of alloy A, B_2 and C_2 (Figure 6.14(a), (b) and (c) respectively) show that the main constituent of the oxide scale is ZrO_2 in case of all three alloys. Peaks of Fe_3O_4, NiO and $NiMoO_4$ were also detected in alloy A. From the XRD pattern of alloy B_2 (Figure 6.14(b)), formation of ZrO_2 is more active than the alloy A (Figure 6.14(a)) due to the dispersion of TiO_2. In alloy B_2 the continuous and high intensity ZrO_2 peaks confirmed the formation of ZrO_2 oxide layer. In case of Y_2O_3, formation of more ZrO_2 was observed (Figure 6.14(c)) as indicated earlier by kinetics study.

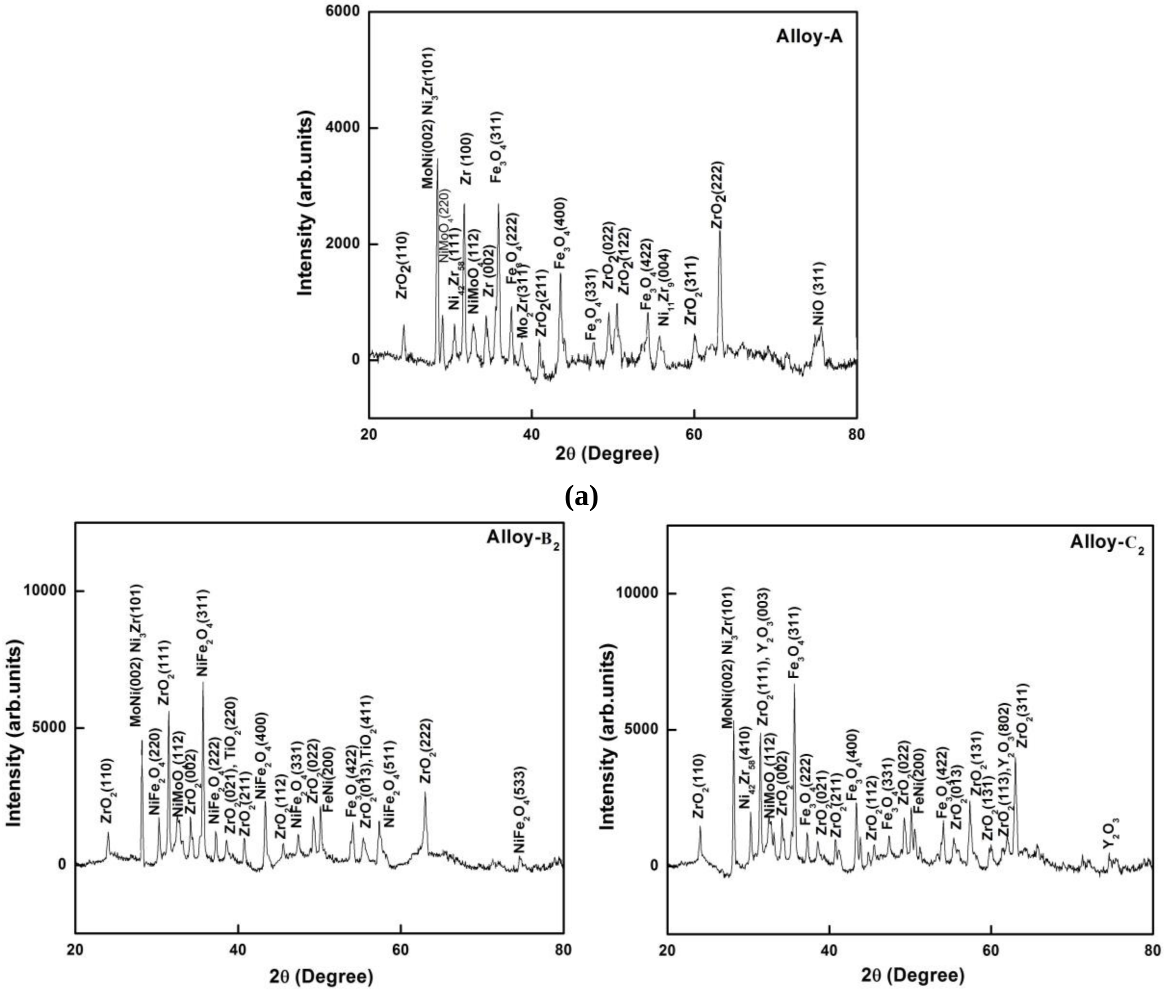

(a)

(b) **(c)**

Figure 6.14: Oxide samples' XRD patterns of alloy (a) A, (b) B_2 and (c) C_2 at 1100 ^{o}C for 50 hours

The SEM micrographs of the surface of the oxidized samples of alloy A, B_2 and C_2 are shown in Figure 6.15(a)-(c) respectively. The oxidized surface layer of alloy A consists of small cracks, while bigger cracks were observed in alloy B_2. A continuous and fully dense oxide layer was covered on the surface of the alloy C_2. Alloy C_2 which does not show any surface cracks even at the temperature of 1100 °C suggest higher stability of the surface oxide.

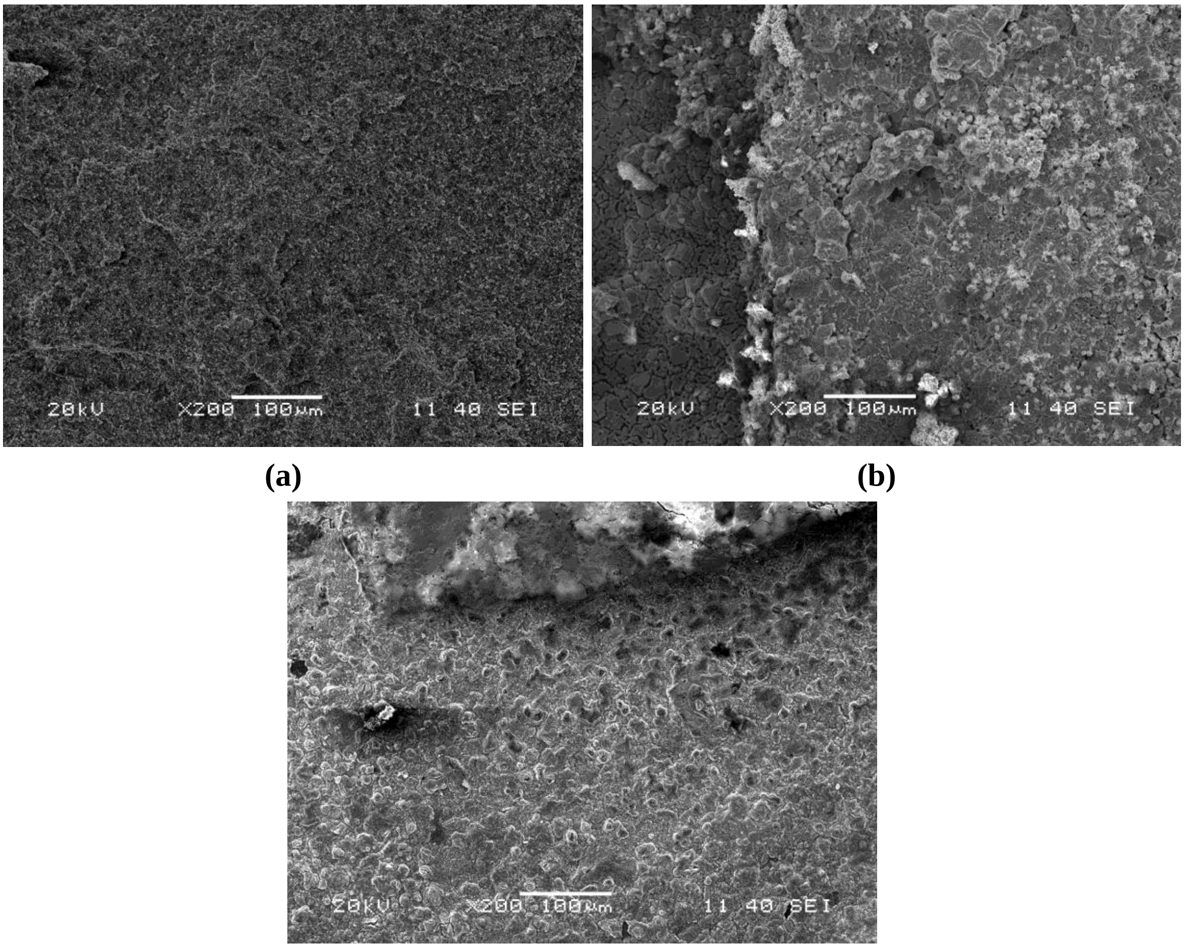

(a) **(b)**

(c)

Figure 6.15: Isothermally oxidized sample surface morphologies of alloy (a) A, (b) B_2 and (c) C_2 at 1100 °C for 50 hours

6.4.2 Non-Isothermal Oxidation

Figure 6.16 compares the extent of oxidation (α) in alloy A, B_2 and C_2 upto 1000 °C at the heating rates of 4, 6, 8 and 10 K/min. Alloy A has shown very low values of α up to 773 K in comparison to alloys B_2 and C_2. However, the alloys B_2 and C_2 has higher oxidation resistance than alloy A at high temperature. The extent of oxidation is low for the alloy A in comparison to the B_2 and C_2 alloys indicating that oxidation resistance has increased after nano crystallization. The degree of oxidation at the heating rate of 10 K/min, α, for the alloys B_2 and C_2 was higher at lower temperature is shown in Figure 6.16(d), there is a gradual increase in oxidation resistance with increase in temperature. The activation energy of oxidation was calculated from the slope of the Kissinger plot ln (Φ/T_p^2) versus $1/T_p$, where Φ is the heating rate, T_p is the onset temperature of oxidation in the heating rate range of 4-10 K/min. Table 6.6 shows the values of activation energies calculated from Kissinger relation and the start temperatures of oxidation at a heating rate of 10 K/min.

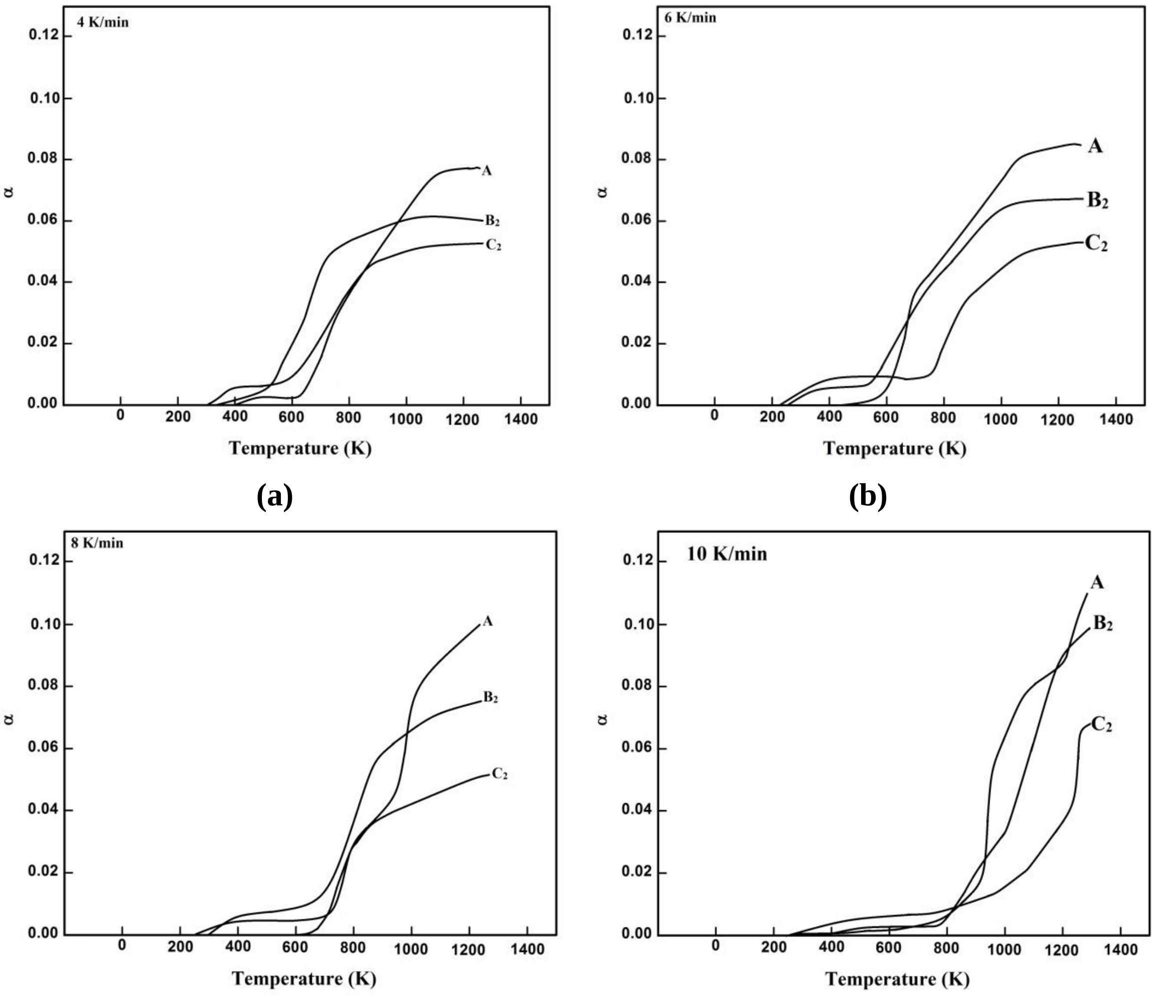

(a) **(b)**

(c) **(d)**

Figure 6.16: Non-isothermal oxidation behavior (α vs. T plot) of A, B_2 and C_2 alloys

Table 6.6: Activation energy for the start of oxidation in alloys A, B_2 and C_2 calculated from Kissinger's plot

Alloy	Activation energy for the oxidation to start (kJ/mol)	Start temperature of oxidation (10 K/min)
A	151.26±3.21	906
B_2	143.22±1.84	748
C_2	139.71±2.67	680

6.5 Summary

This chapter deals with consolidation of powders obtained from Mill-2 by SPS at 900, 950 and 1000 ^{o}C followed by phase analysis and microstructural, mechanical, electrochemical and oxidation properties analysis by XRD, SEM, TEM, hardness, compressive, wear, corrosion, isothermal and non isothermal oxidation testing. Moreover, structure property correlation has been emphasized in the current chapter. In view of this, effect of dispersoids (nano TiO_2/Y_2O_3) addition and consolidation parameters on the above mentioned properties is summarized here.

- XRD analysis of the samples sintered by SPS technique at various temperatures shows presence of intermetallics like MoNi, FeNi, Ni_3Zr, Mo_3Zr and Fe_3Zr along with TiO_2/Y_2O_3 phase in Zr matrix.

- FESEM of samples consolidated by SPS showed fined structure with sub micron to nanometric size range. Partial liquid phase sintering was taken place in samples sintered at 1000 ^{o}C as shown in specific FESEM micrographs.

- From TEM analysis (bright and dark field TEM image and SAD patterns) presence of different intermetallics (FeNi, Mo_2Zr and Fe_3Zr) of 10-20 nm size along with uniform dispersion of TiO_2/Y_2O_3 in the size range of 10-20 nm was confirmed.

- Products sintered with SPS technique showed high density values (~ 99% theoretical density at 1000 ^{o}C) and it was found that sinter density increases with increasing in sintering temperature.

- Hard enhancement was observed with increasing sintering temperatures and dispersoid (TiO_2/Y_2O_3) content. Samples with TiO_2 dispersion shows higher hardness compared to samples dispersed with Y_2O_3 and without dispersion. Maximum hardness of 16.85 GPa was recorded for alloy B_2 sintered at 1000 ^{o}C.

- Similar trend of hardness was also observed during compressive test for all the alloys. Alloy B_2 recoded highest compressive strength (~1240 MPa) when sintered at 1000 ^{o}C. The value is almost 1.5 times higher than that was recorded in conventionally sintered alloy.

- Wear test results show similar trend as that was found during hardness and compressive strength measurements. Wear depths recoded here are smaller than that was reported during wear test of conventionally sintered samples.

- Potentio dynamic polarization test reveals that alloys dispersed with higher amount of dispersoids (TiO_2/Y_2O_3) exhibits lower values of corrosion current density. Alloy C_2 records minimum corrosion rate (1.713 mm/year X 10^{-2}) compared to all alloys discussed.

- Alloy A registrars better oxidation resistance in terms of oxidation activation energy and start temperature of oxidation than that of samples sintered with addition of TiO_2/Y_2O_3 dispersoids (alloy B_2 and C_2).

At the end, it was summarized from the abovementioned points that sample synthesized by Mill-2 and SPS technique with addition of TiO_2/Y_2O_3 dispersoids shows better mechanical properties in terms of hardness, compressive strength and wear resistance. Improvement was also observed with increasing sintering temperatures. However, dispersion addition showed reverse trend in terms of oxidation resistance.

Chapter 7

Conclusion

7.1 Summary

In the present study, a systematic attempt has been made to develop 1.0-2.0 wt. % nano-TiO_2/Y_2O_3 dispersed Zr-Fe-Ni-Mo alloys ($Zr_{45}Fe_{30}Ni_{20}Mo_5$, $Zr_{44}Fe_{30}Ni_{20}Mo_5$ $(TiO_2)_1$, $Zr_{44}Fe_{30}Ni_{20}Mo_4$ $(TiO_2)_2$, $Zr_{44}Fe_{30}Ni_{20}Mo_5$ $(Y_2O_3)_1$ and $Zr_{44}Fe_{30}Ni_{20}Mo_4$ $(Y_2O_3)_2$) by mechanical alloying in two different high energy ball mills followed by subsequent consolidation by conventional and spark plasma sintering. It explores the synthesis of alloy powders involving two different mills and sintering methods used for consolidation of milled powders, effect of dispersiod (1.0-2.0 wt. % nano-TiO_2/Y_2O_3) on the physical, mechanical, corrosion and oxidation properties of the alloys. A few significant new notions have been made in the development of nano- TiO_2/Y_2O_3 dispersed Zr-Fe-Ni-Mo alloys by evaluating the results in terms of synthesis and characterization, consolidation, physical and mechanical properties (density, hardness, compressive strength and wear resistant), high temperature oxidation and corrosion resistance.

Major outcomes of the present study are summarized as follows:

- XRD analysis of the milled product shows that each alloy constitutionally formed solid solution indicating that Fe, Ni and Mo are dissolved in Zr matrix. There was a significant reduction in crystallite size (20-30 nm) and was also confirmed by TEM analysis. The size reduction of particle size was compatible with SEM and Particle size analyzer. Activation energy calculated for final milled powder obtained from dual drive ball mill was higher compared to planetary mill due to high induced strain caused by large impact energy.

- Phase evolution by XRD analysis of conventional and spark plasma sintered products showed the presence of intermetallic phases (Mo_2Zr, $FeZr_2$, NiZr and $Ni_{11}Zr_9$) and (MoNi, FeNi, Ni_3Zr, Mo_3Zr and Fe_3Zr) respectively along with dispersiods (TiO_2/Y_2O_3). From bright and dark field TEM image and SAD analysis, presence of different intermetallics of 10-30 nm size along with TiO_2/Y_2O_3 (10-20 nm) throughout the matrix was confirmed.

- Bulk mechanical properties of the present zirconium alloys consolidated by conventional sintering record high levels of hardness (5.1-7.0 GPa) and compressive strength (428-680 MPa) which are higher than that of similar alloys, developed via the melting casting route. The same set of zirconium alloys consolidated by spark plasma sintering was found to possess extremely high levels of compressive strength (825-1240 MPa) and hardness (10.38-16.85 GPa) due to partial liquid phase sintering and inherent mechanism of SPS process. Increasing dispersion amount improves the mechanical properties and TiO_2 dispersion was found superior than Y_2O_3.

- The wear behavior of the present alloys exhibited same trend as hardness and compressive strength in both the case of sintering techniques. The wear mechanism was found primarily of abrasive in nature.

- Potentiodynamic polarization tests carried out in NaCl solution indicate that increase in TiO_2 dispersion from 1 to 2 wt. % decreases the corrosion rate drastically. On the other hand the Alloy dispersed with Y_2O_3 shows continuous decrease in corrosion rate from 0 to 2 wt. % Y_2O_3. The results show that the alloys dispersed with Y_2O_3 has better corrosion resistance.

- Sintered product prepared without dispersion shows marginally better oxidation resistance in terms of oxidation activation energy than that of samples sintered with addition of TiO_2/Y_2O_3.

After scrutinizing all the above mention points, characterization and results it can be summarized that dual drive ball mill was more efficient than planetary mill and SPS technique was found more efficient and advanced to produce product with better mechanical, oxidation and corrosion properties. It was also found that addition of TiO_2 and Y_2O_3 helps in enhancement of mechanical properties and effect of TiO_2 was more prominent. Sample dispersed with Y_2O_3 displays better corrosion resistance, whereas, base alloy shows best oxidation property.

7.2 Scope for Further Research

After investigating the corrosion and oxidation behaviour it was felt that long-term exposure tests are required for better understanding of high temperature behaviour of these zirconium alloys which can be used in nuclear and chemical applications.

Furthermore, following studies can be carried out in future for better understanding of the developed zirconium alloys in service conditions:

Hydrogen embrittlement: In pressurized water reactors at high temperatures, zirconium quickly reacts with water steam, gets oxidized and release hydrogen gas. This reaction causes hydrogen explosion. Some hydrogen diffuses into the zirconium alloy cladding material forms zirconium hydrides. These hydrides can weaken the cladding material because of having lower ductility and density, causing problems like delayed hydride cracking (DHC). Delayed Hydride Cracking (DHC) is a form of localized hydride-embrittlement phenomenon which, in the presence of a tensile stress-field, manifests itself as a sub-critical crack growth process. It is caused by hydrogen migration up the tensile stress gradient to the region of stress concentration. So, for testing embrittlement due to hydrogen gas, Hydrogen Gas Embrittlement (HGE) test has to be done.

Bent-beam stress relaxation: Measurement of irradiation creep of zirconium alloys using stress relaxation tests gives ability to estimate the in-reactor creep behaviour of zirconium alloys with different prior thermo-mechanical treatments.

Neutron irradiation: Zirconium-based alloys are used widely for fuel cladding and other core components. Irradiation growth under fast neutron irradiation is the main source of dimensional change in zirconium alloys. Therefore, the effect of neutron irradiation of these alloys has to investigate further.

Corrosion study: Zirconium is found to function well in handling and recycling of nitric acid, also used in the preparation of ammonium nitrate and many organic acids. For convenient use of zirconium alloys at high temperatures and concentration, corrosion tests have to be carried out in nitric acid, sulphuric acid and hydrochloric acid media.

Bibliography

[1] S.L. Wadekar, V.V. Raman, S. Banerjee and M.K. Asundi. Structure-Property Correlation of Zr-base Alloys. *Journal of Nuclear Materials*, 151: 162--171, 1987.

[2] J.A.L. Robertson. Zirconium-An International Nuclear Material. *Journal of Nuclear Materials,* 100: 108--118, 1981.

[3] Cong Li, Rulin Zuo, Zhongkui Li, Shihao Ying and Baoluo Shen. Transmission Electron Microscopy Investigation of Zr_2 (Fe, Ni) Particles Incorporated in the Oxide Film Formed on a Zirconium Alloy. *Thin Solid Films*, 461: 272--276, 2004.

[4] R. Krishnan and M.K. Asundi. Zirconium Alloys in Nuclear Technology. *Proceedings of Indian Academy of Sciences (Engineering Science),* 4: 41--56, 1981.

[5] F.X. Qin, H.F. Zhang, Y.F. Deng, B.Z. Ding and Z.Q. Hu. Corrosion Resistance of Zr-Based Bulk Amorphous Alloys Containing Pd. *Journal of Alloys and Compounds*, 375: 318--323, 2004.

[6] Perez, Rosa Jerlerud and Bo Sundman. Thermodynamic Assessment of the Mo-Zr Binary Phase Diagram. *Computer Coupling of Phase Diagrams and Thermochemistry*, 27: 253--262, 2003.

[7] Adamson R. B. and Peter Rudling. Dimensional Stability of Zirconium Alloys. ZIRAT Special Topical Report on Mechanical Properties of Zirconium Alloys Advanced. *Nuclear Technology International*, 2002.

[8] Northwood Derek O. The Development and Applications of Zirconium Alloys. *Materials & Design,* 6(2): 58--70, 1985.

[9] Chaurasia P. K, C. K. Mukhopadhyay, S. Murugan, P. Muralidharan, K. Chandran, V. Ganesan, T. Jayakumar and P. V. Kumar. Tensile Behaviour and Acoustic Emission in Zirconium Alloys after Thermal Aging and Sodium Exposure. *Journal of nuclear materials,* 322(2): 217--227, 2003.

[10] Huasheng Xie, Liu Hongyu, Zhao Jun, Liu Shibing and Shi Kun. Interfacial Reaction between Zirconium Alloy and Graphite Mold/Yttrium Oxide Ceramic Mold. *Research & Development* 11(2): 85--90, 2014.

[11] Davis Joseph R. Corrosion of Weldments. *ASM International,* 2006.

[12] Suryanarayana Challapalli. Mechanical Alloying and Milling. *Progress in Materials Science,* 46(1): 1--184, 2001.

[13] Jurczyk M. Nanocrystalline Materials for Hydrogen Storage. *Journal of Optoelectronics and Advanced Materials,* 8(2): 418--424, 2006.

[14] Suryanarayana C, E. Ivanov and V. V. Boldyrev. The Science and Technology of Mechanical Alloying. *Materials Science and Engineering A,* 304: 151--158, 2001.

[15] Grabias A, D. Oleszak and M. Pekala. Structure and Magnetic Properties of the $Zr_{30}Fe_{35}Ni_{35}$ Alloy Formed by Mechanical Alloying. *Reviews on Advanced Materials Science*, 18: 379--383, 2008.

[16] Scudino S, D. J. Sordelet and J. Eckert. Devitrification of Mechanically Alloyed Zr-Ti-Nb-Cu-Ni-Al Glassy Powders Studied by Time-resolved X-ray Diffraction. *Reviews on Advanced Materials Science,* 18: 221--224, 2008.

[17] Tonejc Antun. Crystallographic Features of Mechanically Milled and Alloyed Nanosized Crystalline and Amorphous Materials. *Acta Chimica Slovenica*, 49(1): 1--28, 2002.

[18] Lee P. Y, M. C. Kao, C. K. Lin and J. C. Huang. Mg-Y-Cu Bulk Metallic Glass Prepared by Mechanical Alloying and Vacuum Hot-pressing. *Intermetallics,* 14(8): 994--999, 2006.

[19] Seidel M, M. Reibold, I. Bacher, H-D. Bauer, J. Eckert and L. Schultz. Progress of Solid-State Reaction during Mechanical Alloying of Zr-Al-Cu-Ni Bulk Metallic Glass-Forming Alloys. *Materials Science and Engineering: A,* 226: 383--387, 1997.

[20] Kuczynski G. C. Physics and Chemistry of Sintering. *Advances in Colloid and Interface Science,* 3(3): 275--330, 1972.

[21] Ristic Momcilo M and S. D. Milosevic. Frenkel's Theory of Sintering. *Science of Sintering,* 38(1): 7--11, 2006.

[22] Guillon Olivier, Jesus Gonzalez-Julian, Benjamin Dargatz, Tobias Kessel, Gabi Schierning, Jan Rathel and Mathias Herrmann. Field-Assisted Sintering Technology/Spark Plasma Sintering: Mechanisms, Materials, and Technology Developments. *Advanced Engineering Materials,* 16(7): 830--849, 2014.

[23] Murty B. S. Mechanical Alloying-A Novel Synthesis Route for Amorphous Phases. *Bulletin of Materials Science,* 16(1): 1--17, 1993.

[24] Majumdar Sanjib and I. G. Sharma. Development of Mo base TZM (Mo-0.5 Ti-0.1 Zr-0.02 C) Alloy and its Shapes. *The Forthcoming issue*, 312: 21--27, 2010.

[25] Choi Chul-Jin. Preparation of Ultrafine TiC-Ni Cermet Powders by Mechanical Alloying. *Journal of Materials Processing Technology,* 104(1): 127--132, 2000.

[26] Chen T. R. and P. Y. Lee. Formation of Amorphous Cu-Zr Alloy Powder by Mechanical Alloying. *Journal of Marine Science and Technology*, 1: 59--64, 1993.

[27] Oleszak D. Mechanical Alloying-A Novel Method for Synthesis and Processing of Materials. *Acta Physica Polonica-Series A General Physics*, 96(1): 101--112, 1999.

[28] Sunol Martinez Joan Josep and Joaquim Fort. Materials Developed by Mechanical Alloying and Melt Spinning. *International Review of Physics*, 2(1): 31--35, 2008.

[29] Sherif M. and El Eskandarany. Mechanical Alloying for Fabrication of Advanced Engineering Materials. *William Andrew Publication*, Norwich, New York, USA 2001.

[30] Bullock E, R. Brunetaud, J. F. Conde, S. R. Keown and S. F. Pugh. Research and Development of High Temperature Materials for Industry. *Springer Science & Business Media,* 2012.

[31] Cahn Robert, Malcolm McLean and Anthony Evans. High-Temperature Structural Materials. *Springer Science & Business Media,* 2012.

[32] Sikka V. K, S. C. Deevi, K. Natesan, P. Ganesan and G. Lai. Heat Resistant Materials II. *ASM International*, Materials Park, OH 157: 1995.

[33] Frommeyer Georg and Ralf Rablbauer. *High Temperature Materials Based on the Intermetallic Compound NiAl Reinforced by Refractory Metals for Advanced Energy Conversion Technologies*. 2008.

[34] Achzet B, Armin Reller, Volker Zepf, C. Rennie, M. Ashfield and J. Simmons. *Materials critical to the energy industry*: *An introduction*. Germany: University of Augsburg 2011.

[35] Osman Todd M. The Nuclear Renaissance: A Challenge for the Materials Community. *Journal of the Minerals, metals, and Materials Society*, 60(1): 10--13, 2008.

[36] Lu K. The Future of Metals. *Science,* 328(5976): 319--320, 2010.

[37] DoE, E. I. A. International Energy Outlook 2005. DOE/EIA-0484. *Energy Information Administration*, 2005.

[38] Gopichandran R, Vipul N. Shah, Niral J. Patel and T. Harinarayana. SMEs can overcome and improve sustainability through preventive management strategies: Some Empirical Evidences from a Cluster of Chemical Industries in Western India. *International Journal of Globalisation and Small Business,* 5(3): 209--223, 2013.

[39] Z. G. Yang, J.W. Stevenson, D.M. Paxton, P. Singh and K.S. Weil. Materials Properties Database for Selection of High-Temperature Alloys and Concepts of Alloy Design for SOFC Applications. Richland, WA*: Pacific Northwest National Laboratory,* 2002.

[40] Schneider Mycle and Antony Froggatt. *World nuclear industry status report, 2013*.

[41] Bychkov Alexander. *Nuclear Power Today and Tomorrow, 2013.*

[42] Flory Denis. *Nuclear Safety through International Cooperation, 2013.*

[43] Schulz Otto, T. Rings, R. Forrest and Joachim von Hoyningen-Huene. Chemical Industry Vision 2030: *A European Perspective*. AT Kearney, 2012.

[44] Karmarkar Amrit B, Avinash D. Deodhar and Aditya A. Holikar. Indian Chemical Industry: *A Potential Chemical Hub for Exploration at World Market*. *Pharma Utility*, 8(1-2): 2014.

[45] Wuchina E, E. Opila, M. Opeka, W. Fahrenholtz and I. Talmy. UHTCs: Ultra-high Temperature Ceramic Materials for Extreme Environment Applications. *The Electrochemical Society Interface,* 16(4): 30--36, 2007.

[46] Reed Roger C, Kenneth A. Green, Pierre Caron, Timothy P. Gabb, Michael G. Fahrmann, Eric S. Huron and Shiela A. Woodard. Challenges for High Temperature Materials in the New Millennium. Superalloys, *The Minerals, Metals & Materials Society,* 2008.

[47] Zirconium Heat Exchanger-A New Direction for Pickling Operations. *Iron and Steel Engineer*, 52: 55, 1975.

[48] Cox B. Some Thoughts on The Mechanisms of In-reactor Corrosion of Zirconium Alloys. *Journal of Nuclear materials*, 336(2):331--368, 2005.

[49] N. Dupin, I. Ansara, C. Servant, C. Toffolon, C. Lemaignan and J.C. Brachet. A Thermodynamic Database for Zirconium Alloys. *Journal of Nuclear Materials*, 275: 287--295, 1999.

[50] http://www.mmta.co.uk/zirconiummarketoverview.

[51] Wasilkowska A, M. Bartsch, U. Messerschmidt, R. Herzog and A. Czyrska-Filemonowicz. Creep mechanisms of Ferritic Oxide Dispersion Strengthened Alloys. *Journal of Materials Processing Technology,* 133(1): 218--224, 2003.

[52] W. Quadakkers. Oxidation of ODS alloys. *Journal de Physique IV*, 03 (C9):177--186, 1993.

[53] Elzey D. M. and E. Arzt. Oxide Dispersion Strengthened Superalloys: The Role of Grain Structure and Dispersion during High Temperature Low Cycle Fatigue. *AIME Sixth International Symposium on Superalloys,* Superalloys, 595--604, 1988.

[54] Gao Lei, R. S. Chen and E. H. Han. Effects of Rare-Earth Elements Gd and Y on the Solid Solution Strengthening of Mg Alloys. *Journal of Alloys and Compounds,* 481(1): 379--384, 2009.

[55] Dieter G. E. *Mechanical metallurgy*. *SI Metric Edn,* 192: 1988.

[56] N J. Grant Etal. *Production of Dispersion Strengthened Metals*. U.S. Patent 3069759, Issued December 25, 1962.

[57] Han B. Q and D. C. Dunand. Creep of Magnesium Strengthened with High Volume Fractions of Yttria Dispersoids. *Materials Science and Engineering: A*, 300(1): 235--244, 2001.

[58] Sundararajan G, R. Vijay and A. V. Reddy. Development of 9Cr Ferritic-Martensitic and 18Cr Ferritic Oxide Dispersion Strengthened Steels. *Current Science*, 105(8): 1100--1106, 2013.

[59] Wright Ian G and Bruce A. Pint. Update on the Status of ODS Alloys for Fossil Energy Applications. *Oak Ridge National Laboratory (ORNL*), 2008.

[60] McKimpson M. G and D. O Donnell. Joining ODS Materials for High-Temperature Applications. *Journal of the Minerals, metals, and Materials Society,* 46(7): 49--51, 1994.

[61] Adamiak M. Mechanical Alloying for Fabrication of Aluminium Matrix Composite Powders with Ti-Al Intermetallics Reinforcement. *Journal of Achievements in Materials and Manufacturing Engineering*, 31(2): 191--196, 2008.

[62] Cheng Zhao-Hua, G. R. MacKay, D. A. Small and R. A. Dunlap. Phase Development in Titanium by Mechanical Alloying Under Hydrogen Atmosphere. *Journal of Physics D: Applied Physics*, 32(15): 1934--1937, 1999.

[63] Suryanarayana C, T. Klassen and E. Ivanov. Synthesis of Nanocomposites and Amorphous Alloys by Mechanical Alloying. *Journal of materials science*, 46(19): 6301--6315, 2011.

[64] DeCastro Claudio L and Brian S. Mitchell. *Nanoparticles from Mechanical Attrition. Synthesis, Functionalization, and Surface Treatment of Nanoparticles*. 1--15, 2002.

[65] Jang J. S. C, J. C. Fwu, L. J. Chang, G. J. Chen and C. T. Hsu. Study on The Solid-Phase Sintering of The Nano-Structured Heavy Tungsten Alloy Powder. *Journal of alloys and compounds*, 434: 367--370, 2007.

[66] Praveen S, Ameey Anupam, Teja Sirasani, B. S. Murty and Ravi S. Kottada. Characterization of Oxide Dispersed AlCoCrFe High Entropy Alloy Synthesized by Mechanical Alloying and Spark Plasma Sintering. *Transactions of the Indian Institute of Metals*, 66(4): 369--373, 2013.

[67] Vikas Chawla, S. Prakash and B. S. Sidhu. State of the Art: Applications of Mechanically Alloyed Nanomaterials-A Review. *Materials and Manufacturing Processes*, 22(4): 469--473, 2007.

[68] Suryanarayana C. Recent Developments in Mechanical Alloying. *Reviews on Advanced Materials Science*, 18(3): 203--211, 2008.

[69] Pilarczyk W, R. Nowosielski, M. Jodkowski, K. Labisz and H. Krzton. Structure and Properties of $Al_{67}Ti_{25}Fe_8$ Alloy Obtained by Mechanical Alloying. *Archives of Materials Science*, 30: 29--32, 2008.

[70] Suryanarayana C and C. C. Koch. Nanocrystalline Materials-Current Research and Future Directions. *Hyperfine Interactions,* 130(1-4): 5--44, 2000.

[71] Liang G. X, Z. C. Li and E. Wang. Microstructure and Mechanical-Properties of Al-4.9 Ni-4.9 Ti Alloy Prepared by Mechanical Alloying. *Journal of Materials Science & Technology*, 11(3): 209--212, 1995.

[72] F. H. Froes, J. J. deBarbadillo and C. Suryanarayana Structural Applications of Mechanical Alloying. *ASM Intl*. 1, 1990.

[73] Bakker H, G. F. Zhou and H. Yang. Mechanically Driven Disorder and Phase Transformations in Alloys. *Progress in Materials Science,* 39(3): 159--241, 1995.

[74] Froes FH Sam, C. Suryanarayana, K. Russell and C-G. Li. Synthesis of Intermetallics by Mechanical Alloying. *Materials Science and Engineering: A*, 192: 612--623, 1995.

[75] Suryanarayana C. The Structure and Properties of Nanocrystalline Materials: Issues and Concerns. *JOM Journal of the Minerals, Metals and Materials Society*, 54(9): 24--27, 2002.

[76] Benjamin J. S and T. E. Volin. The Mechanism of Mechanical Alloying. *Metallurgical Transactions*, 5(8): 1929--1934, 1974.

[77] Koch Carl C. Nanostructured Materials: Processing, Properties and Applications. *William Andrew,* 2006.

[78] Schaffer G. B and P. G. McCormick. Displacement Reactions during Mechanical Alloying. *Metallurgical Transactions A*, 21(10): 2789--2794, 1990.

[79] Ghadimi Morteza and Ali Shokuhfar. Effects of Mechanical Alloying on Microstructure and Microhardness of Nanocrystalline Ni-50 at. % Ti Shape Memory Alloy. International *Journal of Advanced Design and Manufacturing Technology,* 5(5): 25--29, 2013.

[80] Ward Trent S, Wenliang Chen, Mirko Schoenitz, Rajesh N. Dave and Edward L. Dreizin. A study of Mechanical Alloying Processes Using Reactive Milling and Discrete Element Modeling. *Acta Materialia*, 53(10): 2909--2918, 2005.

[81] Pabi S. K, J. Joardar and B. S. Murty. Mechanisms and Kinetics of Alloying and Nanostructure Formation by Mechanical Methods. *Proceedings of the Indian National Science Academy-Part A: Physical Sciences*, 67(1): 1--30, 2001.

[82] Murty, B. S and S. Ranganathan. Novel Materials Synthesis by Mechanical Alloying/Milling. *International materials Reviews,* 43(3): 101--141, 1998.

[83] Benjamin J. S. Fundamentals of Mechanical Alloying. *Materials Science Forum,* 88: 1--18, 1992.

[84] Singh D, C. Suryanarayana, L. Mertus and R-H. Chen. Extended Homogeneity Range of Intermetallic Phases in Mechanically Alloyed Mg-Al Alloys. *Intermetallics*, 11(4): 373--376, 2003.

[85] Balaz Peter, Marcela Achimovicova, Matej Balaz, Peter Billik, Zara Cherkezova-Zheleva, Jose Manuel Criado, Francesco Delogu et al. Hallmarks of Mechanochemistry: from Nanoparticles to Technology. *Chemical Society Reviews*, 42(18): 7571--7637, 2013.

[86] Shen T. D, C. C. Koch, T. Y. Tsui and G. M. Pharr. On the Elastic Moduli of Nanocrystalline Fe, Cu, Ni, and Cu-Ni Alloys Prepared by Mechanical Milling/Alloying. *Journal of Materials Research*, 10(11): 2892--2896, 1995.

[87] Davis R. M, B. Mc Dermott and C. C. Koch. Mechanical Alloying of Brittle Materials. *Metallurgical Transactions A*, 19(12): 2867--2874, 1988.

[88] Kimura H and M. Kimura. Solid State Powder Proc. eds. AH Clauer and JJ deBarbadillo, Minerals. *Metals and Materials Society*, 365: 1990.

[89] A.B. Borzov E.Y. Kaputkin. In: de Barbadillo JJ, et al. Mechanical Alloying for Structural Applications. Materials Park, OH: *ASM International*, 1993.

[90] Kuhn W. E, I. L. Friedman, W. Summers and A. Szegvari. ASM Metals Handbook. Vol. 7. *Powder Metallurgy*, Metals Park (OH), 56: 1985.

[91] Schwarz Ricardo B and Carl C. Koch. Formation of Amorphous Alloys by The Mechanical Alloying of Crystalline Powders of Pure Metals and Powders of Intermetallics. *Applied Physics Letters*, 49(3): 146--148, 1986.

[92] Davis Robert Mark and C. C. Koch. Mechanical Alloying of Brittle Components: Silicon and Germanium. *Scripta metallurgica*, 21(3): 305--310, 1987.

[93] Schwarz R. B, K. L. Wong, W. L. Johnson and B. M. Clemens. A Study of Amorphous Alloys of Au with Group III A Elements (Y and La) Formed by a Solid-State Diffusion Reaction. *Journal of Non-Crystalline Solids*, 61: 129--134, 1984.

[94] Yavari A. R and P. J. Desre. Amorphization by Mechanical Alloying and by Solid-State Reaction: Similarities and differences. *Materials Science and Engineering A*, 134: 1315--1322, 1991.

[95] McHenry Michael E, Matthew A. Willard and David E. Laughlin. Amorphous and Nanocrystalline Materials for Applications as Soft Magnets. *Progress in Materials Science*, 44(4): 291--433, 1999.

[96] Haruyama, Osami and Nobuo Asahi. Amorphization of mixed Ni and Zr Powders by Mechanical Alloying. *Materials Science Forum*, 88: 333--338, 1992.

[97] Lee Y. B, H. C. Park, K. D. Oh, C. R. Bowen and R. Stevens. Self-Propagating High-Temperature Synthesis of ZrB_2 in the System ZrO_2-B_2O_3-Fe_2O_3-Al. *Journal of Materials Science Letters*, 19(6): 469--471, 2000.

[98] Froes F.H, Suryanarayana C, Russel K.C and Ward M. Proceedings of Symposium held at Materials Week, *The Minerals & Materials Society (TMS) and the Materials Information Society, ASM International*, 1--21, 1994.

[99] Eckert J, J. C. Holzer, C. E. Krill iII and W. L. Johnson. Mechanically driven Alloying and Grain size Changes in Nanocrystalline Fe-Cu Powders. *Journal of Applied Physics*, 73(6): 2794--2802, 1993.

[100] Zuo Ke-Sheng, Sheng-Qi Xi and Jing-En Zhou. Effect of Temperature on Mechanical Alloying of Cu-Zn and Cu-Cr System. *Transactions of Non-ferrous Metals Society of China*, 19(5): 1206--1214, 2009.

[101] Dong Y. Mechanically-Driven Amorphization in Metallic Systems. *Journal of Materials Science & Technology* (China) (USA), 9(3): 161--166, 1993.

[102] Couples. Thin Film Diffusive. Solid State Amorphization of the Platinum Metals. *Platinum Metals Review*, 35(2): 83--85, 1991.

[103] N. Burgio, A. Iasonna, M. Magini and F. Padella. Mechanical Alloying of the Fe-Zr System in Different Milling Conditions. *Journal de Physique Colloques*, 51 (C4): 265--271, 1990.

[104] Kapaklisa V, S. Baskoutasb and C. Politisac. Glass Forming Ability of Bulk and Mechanically Alloyed $Zr_{55}Cu_{19}Ni_8Al_8Si_5Ti_5$ Amorphous Alloys. *Journal of Optoelectronics and Advanced Materials*, 5(5): 1255--1258, 2003.

[105] Long Woyun, Xueqiong Ouyang, Zhiwei Luo, Jing Li and Anxian Lu. Research on Zr_{50} Al_{15-x} $Ni_{10}Cu_{25}Y_x$ Amorphous Alloys Prepared by Mechanical Alloying with Commercial Pure Element Powders. *Physica B: Condensed Matter*, 406(3): 503--507, 2011.

[106] Allen T. R., R. J. M. Konings and A. T. Motta. *Corrosion of Zirconium Alloys. Comprehensive Nuclear Materials*: 49--68, 2012.

[107] Jeong Yong Hwan, B. J. Baek and S. Y. Park. Waterside Corrosion of Zirconium Alloys in Nuclear Power Plants. *Korea Atomic Energy Research Institute*, Taejon (Republic of Korea), 1999.

[108] Kim Hyun-Gil, Il-Hyun Kim, Yang-Il Jung, Dong-Jun Park, Jeong-Yong Park and Yang-Hyun Koo. Microstructure and Mechanical Strength of Surface ODS Treated Zircaloy-4 Sheet Using Laser Beam Scanning. *Nuclear Engineering and Technology*, 46(4): 521--528, 2014.

[109] Jeong Y. H, J. Y. Park, H. G. Kim, J. T. Busby, E. Gartner, M. Atzmon, G. S. Was et al. Corrosion of Zirconium-Based Fuel Cladding Alloys in Supercritical Water. In Proc. 12th Int. Conf. on Environmental Degradation of Materials in Nuclear Power Systems–Water Reactors, eds. T. Allen, PJ King, L. Nelson (Warrendale, PA: *The Minerals, Metals, and Materials Society [TMS]*,1--369, 2005.

[110] Yadav Thakur Prasad, Ram Manohar Yadav and Dinesh Pratap Singh. Mechanical Milling: ATop DownApproach for the Synthesis of Nanomaterials and Nanocomposites. *Nanoscience and Nanotechnology*, 2(3): 22--48, 2012.

[111] Klepfer H. H. and A. S. Mehner. Specific Zirconium Alloy Design Program. *European Atomic Energy Community - EURATOM*, Brussels, 1966.

[112] Adolph Eivind, Niels Hansen, J. Jensen, E. Hindle, D. Marsh, J. Kjoller and P. Donald. *Dispersion-Strengthened Zirconium Products*. U.S. Patent 3775823, Issued December 4, 1973.

[113] Antony K. C and H. H. Klepfer. Dispersion-Strengthened Zirconium Alloys. *Journal of the Less Common Metals,* 8(1): 36--46, 1965.

[114] Suri A. K. Material Development for India's Nuclear Power Programme. *Sadhana* 38(5): 859--895, 2013.

[115] Rezek J and B. G. Childs. Structure and Properties of Yttria-Zirconium Dispersions. *Journal of Nuclear Materials*, 26(3): 285--299, 1968.

[116] Parsons P. O and Eivind Adolph. Zirconium Alloys Dispersion Strengthened with Yttria. *Canadian Metallurgical Quarterly*, 11(1): 223--235, 1972.

[117] Yusoff Mahani and Zuhailawati Hussain. Effect of Sintering Parameters on Microstructure and Properties of Mechanically Alloyed Copper-Tungsten Carbide Composites. *InternationalJournal of Materials, Mechanics and Manufacturing*, 1(3): 283--286, 2013.

[118] Frenkel J. On the Surface Motion of Particles in Crystals and the Natural Roughness of Crystalline Faces. *Journal of Physics* USSR, 9: 392--398, 1945.

[119] Ristic M. M and M. V. Nikolic. Sixty Years of the Theory of B. Ya. Pines. *Science of Sintering,* 38(3): 201--202, 2006.

[120] Munoz Daniel Pino, Julien Bruchon, Francois Valdivieso and Sylvain Drapier. Solid-State Sintering Simulation: Surface, Volume and Grain-Boundary Diffusions. *European Congress on Computational Methodsin Applied Sciences and Engineering (ECCOMAS* 2012), 2012.

[121] Chinelatto Adriana Scoton Antonio, Adilson Luiz Chinelatto, Ana Maria de Souza, Eliria Maria de Jesus Agnolon Pallone, Milena Kowalczuk Manosso and Roberto Tomasi.

Mechanisms of Microstructure Control in Conventional Sintering. *INTECH Open Access Publisher*, 2012.

[122] Allen A. J, Krueger S, Skandan G, Long G. L, Hahn H, Kerch H. M, Parker J. C and Ali M. N. Microstructural Evolution During the Sintering of Nanostructured Ceramic Oxides *Journal of the American Ceramic Society*, 79(5): 1201--1212, 1996.

[123] Averback R. S, H. J. Hofler, H. Hahn and J. C. Logas. Sintering and Grain Growth in Nanocrystalline Ceramics. *Nanostructured Materials*, 1(2): 173--178, 1992.

[124] Chen P. L and Chen I. W. Sintering of Fine Oxide Powders: I, Microstructural Evolution, *Journal of the American Ceramic Society*, 79(12): 3129--3141, 1996.

[125] Hahn H, Logas J and Averback R. S. Sintering Characteristics of Nanocrytalline TiO_2, *Journal of Materials Research*, 5(3):609--614, 1990.

[126] Groza Joanna R. Nanosintering. *Nanostructured Materials*, 12(5): 987--992, 1999.

[127] Dejonghe Lutgard C and Mohamed N. Rahaman. Sintering of Ceramics.Handbook of Advanced Ceramics*: Materials, Applications, Processing and Properties*, 2: 187--264, 2003.

[128] Borrell Amparo, I. Alvarez, Ramon Torrecillas, Victoria G. Rocha and Adolfo Fernandez. Microstructural Design for Mechanical and Electrical Properties of Spark Plasma Sintered Al_2O_3-SiC Nanocomposites. *Materials Science and Engineering: A*, 534: 693--698, 2012.

[129] Tokita Masao. Recent Progress of Spark Plasma Sintering (SPS) Method and Industrial use of Functionally Graded Materials (FGMs). *Blucher Material Science Proceedings* 1: 90--93, 2014.

[130] Rajeswari K, U. S. Hareesh, R. Subasri, Dibyendu Chakravarty and R. Johnson. Comparative Evaluation of Spark Plasma (SPS), Microwave (MWS), Two Stage Sintering (TSS) and Conventional Sintering (CRH) on The Densification and Micro Structural Evolution of Fully Stabilized Zirconia Ceramics. *Science of Sintering*, 42(3): 259--267, 2010.

[131] Li Xiaoqiang, Yongquan Ye, Yu Tang and Shengguan Qu. Effect of Pulsed Magnetic Field on Spark Plasma Sintering of Iron-Based Powders. *Materials Transactions*, 51(7): 1308--1312, 2010.

[132] Schmidt J, T. Weissgaerber, T. Schubert and B. Kieback. Spark Plasma Sintering of Intermetallics and Metal Matrix Composites. *Sintering II, Euro* PM2005, 2005.

[133] Figiel P, M. Rozmus and B. Smuk. Properties of Alumina Ceramics Obtained by Conventional and Non-conventional Methods for Sintering Ceramics. *Journal of Achievements in Materials and Manufacturing Engineering*, 48(1): 29--34, 2011.

[134] Groza Joanna R and Antonios Zavaliangos. Sintering Activation by External Electrical Field. *Materials Science and Engineering A*, 287(2): 171--177, 2000.

[135] L. Gao, J. S. Hong, H. Miyamoto and S. D. D. L. Torre, Bending Strength and Microstructure of Alumina Ceramic Densified by Spark Plasma Sintering. *Journal of the European Ceramic Society,* 20: 2149--52, 2000.

[136] Chakravarty D, Bysakh S, Muraleedharan K, Rao T. N. and Sundaresan R. Spark Plasma Sintering of Magnesia-Doped Alumina with High Hardness and Fracture Toughness, *Journal of the American Ceramic Society*, 91(1):203--208, 2008.

[137] Bernard-Granger and C. Guizard. Spark Plasma Sintering of a Commercially Available Granulated Zirconia Powder: I. Sintering Path and Hypotheses About the Mechanism(s) Controlling Densification, *Acta Materialia*, 55: 3493--504, 2007.

[138] Zamora V, A. L. Ortiz, F. Guiberteau and Mats Nygren. Crystal-size Dependence of The Spark-Plasma-Sintering Kinetics of ZrB_2 Ultra-High-Temperature Ceramics. *Journal of the European Ceramic Society,* 32(2): 271--276, 2012.

[139] Thompson Matthew, William G. Fahrenholtz and Greg Hilmas. Effect of Starting Particle Size and Oxygen Content on Densification of ZrB_2. *Journal of the American Ceramic Society*, 94(2): 429--435, 2011.

[140] Chaira Debasis, B. K. Mishra and S. Sangal. Synthesis and Characterization of Silicon Carbide by Reaction Milling in a Dual-drive Planetary Mill. *Materials Science and Engineering A,* 460: 1110--120, 2007.

[141] Mote V. D, Y. Purushotham and B. N. Dole. Williamson-Hall Analysis in Estimation of lattice Strain in Nanometer-sized ZnO Particles. *Journal of Theoretical and Applied Physics*, 6(1): 1--8, 2012.

[142] Nuthalapati Mohan, S. K. Karak, J. Dutta Majumdar and A. Basu. Phase Evolution and Mechanical Properties of Nano-TiO_2 Dispersed Zr-Based Alloys by Mechanical Alloying and Conventional Sintering. *Metallurgical and Materials Transactions A*, 45(9): 3748--3754, 2014.

[143] Wachtman Jr J. B, W. E. Tefft and D. G. Lam Jr. Elastic constants of rutile (TiO_2). *Journal of Research of the Rational Bureau of Standards-A. Physics and Chemistry,* 66(6):465--471, 1962.

[144] Sayir Ali, James W. Palko, Waltraud M. Kriven, Sergey V. Sinogeikin and Jay D. Bass. Single-Crystal Elastic Constants of Yttria (Y_2O_3) Measured to High Temperatures. 2001.

[145] ChutoToshinori, Fumihisa Nagase and Toyoshi Fuketa. High Temperature Oxidation of Nb-containing Zr Alloy Cladding in LOCA Conditions. *Nuclear Engineering and Technology*, 41(2): 163--170, 2009.

[146] Xie Z. M, R. Liu, Q. F. Fang, Y. Zhou, X. P. Wang and C. S. Liu. Spark Plasma Sintering and Mechanical Properties of Zirconium Micro-Alloyed Tungsten. *Journal of Nuclear Materials*, 444(1): 175--180, 2014.

[147] Nuthalapati Mohan, S. K. Karak, D. Chakravarty and A. Basu. Development of Nano-Y_2O_3 Dispersed Zr Alloys by Mechanical Alloying and Spark Plasma Sintering. *Materials Science and Engineering A*, 650: 145--153, 2016.

[148] Karak S. K., J. Dutta Majumdar, W. Lojkowski, A. Michalski, L. Ciupinski, K. J. Kurzydłowski and Indranil Manna. Microstructure and Mechanical Properties of Nano-Y_2O_3 Dispersed Ferritic Steel Synthesized by Mechanical Alloying and Consolidated by Pulse Plasma Sintering. *Philosophical Magazine*, 92(5): 516--534, 2012.

[149] Roy D, S. Kumari, R. Mitra and I. Manna. Microstructure and Mechanical Properties of Mechanically Alloyed and Spark Plasma Sintered Amorphous-Nanocrystalline Al 65 Cu 20 Ti 15 Intermetallic Matrix Composite Reinforced with TiO_2 Nanoparticles. Intermetallics, 15(12): 1595--1605, 2007.

[150] Busser Vincent, Marie-Christine Baietto-Dubourg, Jean Desquines, Christian Duriez and Jean-Paul Mardon. Mechanical Response of Oxidized Zircaloy-4 Cladding Material Submitted to a Ring Compression Test. *Journal of Nuclear Materials*, 384(2): 87--95, 2009.

[151] Parida G, D. Chaira, M. Chopkar and A Basu. Synthesis and Characterization of Ni-TiO_2 Composite Coatings by Electro-co-deposition. *Surface and Coatings Technology*, 205(21): 4871--4879, 2011.

Dissemination

Journal Articles

1. **Nuthalapati Mohan**, S.K. Karak, J. Dutta Majumdar and A. Basu. Phase Evolution and Mechanical Properties of Nano-TiO_2 Dispersed Zr-based Alloys by Mechanical Alloying and Conventional Sintering. *Metallurgical and Materials Transactions A*, 45: 3748--3754, 2014.

2. **Nuthalapati Mohan**, S. K. Karak and A. Basu. Synthesis and Characterization of Nano-Y_2O_3 Dispersed Zr based Alloys by Mechanical Alloying and Conventional Sintering. *Materials Today: Proceedings* 2:1109--1117, 2015.

3. **Nuthalapati Mohan**, S. K. Karak, D. Chakravarty and A. Basu. Development of Nano-Y_2O_3 Dispersed Zr Alloys by Mechanical Alloying and Spark Plasma Sintering. *Materials Science and Engineering A*, 650: 145--153, 2016.

4. **Nuthalapati Mohan**, S. K. Karak and A. Basu. Corrosion Behaviour and High Temperature Oxidation Kinetics of Nano-TiO_2/Y_2O_3 Dispersed Zirconium Alloys (To be communicated).

Conference Presentations

1. Presented a poster on the topic ***Synthesis and Characterization of Zr Based Alloy by Mechanical Alloying for High temperature Applications***in 50thNational metallurgists' day, 66th Annual Technical Meeting NMD ATM 2012 Jamshedpur.

2. Presented a poster on the topic ***Microstructure and Mechanical Properties of Nano TiO_2 Dispersed Zr Based Alloy by Mechanical Alloying and Conventional Sintering*** in 51st national metallurgists' day, 67th annual technical meeting NMD ATM 2013 BHU (Varanasi).

3. Presented a paper on the topic ***Synthesis and Characterization of Nano-Y_2O_3 Dispersed Zr-based Alloys by Mechanical Alloying and Conventional Sintering*** in 4th International Conference on Materials Processing and Characterization (ICMPC 2015), India, Hyderabad.

Vitae

Name	Mohan Nuthalapati
Date of Birth	06.05.1984
Permanent Address	S/O. Subbarao Nuthalapati Tellabadu (P.O), Maddipadu (M.D), Prakasam (D.T), Andhra Pradesh, India-523263
E-mail ID	mohan.nmn7@gmail.com
Languages Known	English, Hindi, Telugu

Educational Qualification

Exam. passed	**Discipline/ Specialization**	**Name of the Institution (School /College etc.)**	**Board of university**	**Year of passing**	**Divn. 1st, 2nd, 3rd**
M.Tech	Material Science & Engg.	NIFFT	-	2011	1st
M.Sc	Physics	C.S.R.Sharma College	ANU	2007	1st
B.Sc	M.P.C	A.C. College	ANU	2005	1st
Intermediate	M.P.C	A.P.S.W.R.Jr College	AP BIE	2002	1st
SSC	General Science	P.N.Z.P.H.School	AP SSC	2000	1st

Journal Articles

1. **Nuthalapati Mohan**, S.K. Karak, J. Dutta Majumdar and A. Basu. Phase Evolution and Mechanical Properties of Nano-TiO_2 Dispersed Zr-based Alloys by Mechanical Alloying and Conventional Sintering. *Metallurgical and Materials Transactions A*, 45: 3748--3754, 2014.
2. **Nuthalapati Mohan**, S. K. Karak and A. Basu. Synthesis and Characterization of Nano-Y_2O_3 Dispersed Zr-based Alloys by Mechanical Alloying and Conventional Sintering. *Materials Today Proceedings* 2:1109--1117, 2015.
3. **Nuthalapati Mohan**, S. K. Karak, D. Chakravarty and A. Basu. Development of Nano-Y_2O_3 Dispersed Zr Alloys by Mechanical Alloying and Spark Plasma Sintering. *Materials Science and Engineering A*, 650: 145--153, 2016.
4. Shyam Ranjan Kumar, **Mohan Nuthalapati** and Joydeep Maity. Development of nanocrystalline ZnSe thin film through electro-deposition from a non-aqueous solution. *Scripta Materialia*, 67:396--399, 2012.

Conference Presentations

1. Presented a poster on the topic ***Synthesis and Characterization of Zr based Alloy by Mechanical Alloying for High Temperature Applications*** in 50th National metallurgists' day, 66th Annual Technical Meeting NMD ATM 2012 Jamshedpur.
2. Presented a poster on the topic ***Microstructure and Mechanical Properties of Nano TiO_2 Dispersed Zr Based Alloy by Mechanical Alloying and Conventional Sintering*** in 51st national metallurgists' day, 67th annual technical meeting NMD ATM 2013 BHU (Varanasi).
3. Presented a paper on the topic ***Synthesis and Characterization of Nano-Y_2O_3 Dispersed Zr-based Alloys by Mechanical Alloying and Conventional Sintering*** in 4th International Conference on Materials Processing and Characterization (ICMPC-2015), India, Hyderabad.